

**Department of Physical Chemistry**

**Faculty of Science**

**PALACKY UNIVERSITY, OLOMOUC**



**Hybrid nanostructures for photoelectrochemical  
water splitting**

Doctoral Dissertation

Author:

**Mahdi Shahrezaei, MSc**

Supervisor:

**Štěpán Kment, Ph.D.**

Under:

Study program: P1417 Chemistry

Field of study: Physical Chemistry

Olomouc 2023



## Annotation

Department of Physical Chemistry, Faculty of Science

Palacky University, Olomouc

Candidate	Mahdi Shahrezaei
Title	Hybrid nanostructures for photoelectrochemical water splitting
Supervisor	Štěpán Kment, Ph.D.
Defense year	2023
Type of thesis	Doctoral
Language	English
Abstract	<p>TiO<sub>2</sub> has been extensively studied as a promising photocatalyst for clean and sustainable photocatalytic hydrogen production. However, its high recombination rate of photoexcited charge carriers and limited absorption of the visible spectrum due to a high band gap energy are significant drawbacks. To address these limitations, extensive research has been conducted. In this thesis, we focused on the effective use of noble metal such as Pt on the TiO<sub>2</sub> nanostructured surfaces and platinized cyanographene for photocatalytic and photoelectrochemical applications.</p>
Keywords	TiO <sub>2</sub> nanotube arrays, platinized cyanographene, photoelectrochemical properties, single-atom catalysts, hydrogen evolution, photocatalysis



## **Author Declaration**

I hereby declare that the Ph.D. thesis entitled “Hybrid nanostructures for photoelectrochemical water splitting” is an authentic record of my research work performed during my doctoral study under the supervision of Associate Professor Štěpán Kment. All experimental work of this thesis is performed in the Czech Advanced Technologies and Research Institute (CATRIN-RCPTM) as well as the Department of Physical Chemistry, Palacký University Olomouc. All the further information used for this original work has been referenced as well. I declare that this dissertation contains no material, which has been submitted elsewhere as part of any academic degree.

In Olomouc, 10<sup>th</sup> August. 2023

Mahdi Shahrezaei



## **Acknowledgement**

First, I would like to express my deepest gratitude to my supervisor Associate Professor Štěpán Kment for his kindness, undivided supervision, immensely supporting and encouragement throughout my Ph.D. study. Thank you for the opportunity to be part of your team and not only to enter to the scientific community, but also to enhance my personality. I especially would like to thank Associate Professor Alberto Naldoni for his assistance, constructive suggestions, and friendship during my Ph.D.

Further, I am thankful to Professor Libor Kvítek and Dr. S. M. Hossein Hejazi for their kind help throughout my Ph.D. career. I also wish to extend my sincere respect and thankfulness to my fellow lab mates, my friends, and all my colleagues in Department of Physical Chemistry, CATRIN, and RCPTM who has supported and helping me through this entire process. Special thanks to my Iranian friends who kept me motivated, smiling, and being with me whenever I need them. Finally, my heartfelt regard goes to my wife, my parents, and my sisters for their endless love, invaluable support, and infinite trust as always.



# Table of contents

<b>Table of contents .....</b>	<b>ix</b>
<b>List of figures .....</b>	<b>xiii</b>
<b>List of tables .....</b>	<b>xviii</b>
<b>Chapter 1: Energy and Photoelectrochemical water splitting .....</b>	<b>1</b>
<b>1.1 Introduction.....</b>	<b>1</b>
<b>1.2 Solar energy.....</b>	<b>1</b>
<b>1.3 Hydrogen production methods .....</b>	<b>2</b>
1.3.1 Steam methane reforming .....	2
1.3.2 Water electrolysis .....	3
1.3.3 Photocatalysis.....	4
1.3.3.1 Semiconductor and band diagram .....	6
1.3.4 Photoelectrocatalysis.....	9
1.3.4.1 Estimation of the PEC water splitting efficiency .....	11
<b>Chapter 2: TiO<sub>2</sub> for water splitting application.....</b>	<b>15</b>
<b>2.1 Titanium dioxide (TiO<sub>2</sub>) as a benchmark photocatalyst .....</b>	<b>15</b>
<b>2.2 TiO<sub>2</sub> nanostructuring .....</b>	<b>17</b>
2.2.1 Hydrothermal method .....	18
2.2.2 Anodization method of TiO <sub>2</sub> nanotube synthesis .....	18
<b>2.3 Modifications of TiO<sub>2</sub> nanostructures .....</b>	<b>21</b>
2.3.1 Non-metal doping .....	22
2.3.2 Metal doping.....	23
2.3.2.1 Noble metal decoration .....	24
2.3.2.1.1 Single atom (SA) decoration .....	26
2.3.2.1.2 Plasmonic-enhanced performance .....	28

2.3.3	Black TiO <sub>2</sub> .....	29
2.3.3.1	Reduction treatment under high temperature .....	32
2.3.3.2	Electrochemical reduction.....	33
2.3.3.3	Chemical reduction.....	34
2.3.3.4	H <sub>2</sub> plasma .....	36
2.3.3.5	Ion bombardment.....	36
2.3.3.6	Sonication.....	37
<b>2.4</b>	<b>The aim of this work .....</b>	<b>38</b>
<b>Chapter 3: Materials and method .....</b>		<b>41</b>
<b>3.1</b>	<b>Fabrication of different morphology of TiO<sub>2</sub> nanotubes.....</b>	<b>41</b>
3.1.1	Compact TiO <sub>2</sub> nanotubes (TNTs).....	41
3.1.2	Multi-leg TiO <sub>2</sub> nanotubes (MLTNTs).....	42
<b>3.2</b>	<b>Modification of TiO<sub>2</sub> nanostructures.....</b>	<b>42</b>
3.2.1	Thermal treatment.....	42
3.2.2	Preparation of the cyanographene and platinized cyanographene composite.....	43
3.2.3	Preparation of Pt-SA.....	44
<b>3.3</b>	<b>Material characterization .....</b>	<b>44</b>
3.3.1	Scanning electron microscopy (SEM) .....	44
3.3.2	Energy-dispersive X-ray spectroscopy (EDS).....	45
3.3.3	Transmission electron microscopy (TEM).....	46
3.3.4	X-ray photoelectron spectroscopy (XPS).....	47
3.3.5	X-ray diffraction pattern (XRD).....	49
3.3.6	Ultraviolet-visible diffuse reflectance spectra (UV-Vis DRS).....	49
3.3.7	Raman Spectroscopy.....	50
<b>3.4</b>	<b>Photoelectrocatalytic and electrochemical characterization.....</b>	<b>51</b>
3.4.1	Photoelectrochemistry measurement .....	51
3.4.2	Open-circuit hydrogen-evolution.....	51

<b>Chapter 4: Results and discussions .....</b>	<b>54</b>
<b>4.1 Fabrication of MLTNTs and influence of process parameters .....</b>	<b>54</b>
4.1.1 Effect of anodization temperature.....	54
4.1.2 Effect of anodization voltage.....	55
4.1.3 Effect of anodization time .....	56
4.1.4 Anodization in dimethyl sulfoxide (DMSO) electrolyte.....	57
<b>4.2 MLTNTs photoelectrodes modified by platinized cyanographene .....</b>	<b>58</b>
4.2.1 Synthesis and characterization.....	59
4.2.2 Photoelectrochemical performance of the structures .....	63
4.2.3 Conclusion.....	71
<b>4.3 Fabrication of compact TiO<sub>2</sub> nanotubes (TNTs) .....</b>	<b>71</b>
4.3.1 Mechanical treatment .....	71
4.3.2 Chemical treatment .....	72
<b>4.4 Controlled loading of Pt single atoms as a co-catalyst on reduced TiO<sub>2</sub>.....</b>	<b>73</b>
4.4.1 Characterization of fabricated nanostructures .....	74
4.4.2 Photoelectrochemical performance of TiO <sub>2</sub> as a substrate .....	77
4.4.3 Deposition of Pt single atom and material characterization .....	80
4.4.4 Photocatalytic hydrogen evolution .....	85
4.4.5 Conclusion.....	89
<b>Chapter 5: Summary and Outlook.....</b>	<b>91</b>
<b>5.1 Summary .....</b>	<b>91</b>
<b>5.2 Outlook .....</b>	<b>93</b>
<b>References .....</b>	<b>95</b>
<b>List of abbreviations and acronyms .....</b>	<b>108</b>
<b>List of Publications .....</b>	<b>111</b>



# List of figures

Figure 1.1 Water electrolysis process.....	4
Figure 1.2 Thermodynamic illustration of a) uphill reaction and b) downhill reaction [13]......	5
Figure 1.3 Energy band diagram demonstrating different band gap energies. ....	7
Figure 1.4 The band edge potentials and band gaps of different semiconductors [26]. ....	7
Figure 1.5 Schematic illustration of photoexcited electron-hole pairs on a semiconductor and possible recombination and reaction path. ....	8
Figure 1.6 Schematic illustration of the hydrogen production via water dissociation mechanism on semiconductor. ....	9
Figure 1.7 Illustration schematic of a photoelectrochemical cell that involves of a semiconducting photoanode and a metal cathode [32]......	10
Figure 2.1 Crystal structures of TiO <sub>2</sub> (spheres: red—O <sub>2</sub> , grey—Ti) [47]. ....	16
Figure 2.2 Anodization set-up for synthesizing the nanotubes [66,67]......	20
Figure 2.3 a) Schematic illustration of anodization at the metal-oxide interface indicating ions migration processes during the anodization of Ti b), formation of TiO <sub>2</sub> NTs, and c) I-t at different stages: (I) formation of compact oxide layer, (II) nanopore formation, and (III) self-ordering of TiO <sub>2</sub> nanotubes [72,73]. ....	21
Figure 2.4 A) Schematics illustration of the new-formed valence band structure by using non-metal dopants. B) Valence band XPS and C) Uv-vis spectra of a) pure TiO <sub>2</sub> , b) C-TiO <sub>2</sub> , C) S-TiO <sub>2</sub> and d) N-TiO <sub>2</sub> [81]. ....	23
Figure 2.5 Metal-doped photocatalyst a) donor level and b) acceptor level [81]. ....	24
Figure 2.6 Illustration of energy diagram for PEC-WS with and without co-catalyst. ....	25
Figure 2.7 Volcano plot showing the relationship between the exchange current and the M-H bond strength [93]......	26
Figure 2.8 Schematic illustration of a) the surface free energy changes and its specific activity per metal atom [98] and, b) difference between SAC (left) and ADC (right). [110]......	28

Figure 2.9 Schematic illustration of a) LSPR of metal NPs, b) Co-catalyst effect of NPs c) the plasmon-induced charge separation of plasmonic NPs and d) hot electrons with sufficient energies can pass the Schottky barrier and reach to the semiconductor conduction band [115,116].	29
Figure 2.10 A) Optical absorption of spectra of (a) white TiO <sub>2</sub> and (b) black TiO <sub>2</sub> . Inset shows the extended absorption of black TiO <sub>2</sub> nanoparticles, B) Schematic illustration of structure and density of state (DOS) of fabricated black TiO <sub>2</sub> , C) pictures of white and black TiO <sub>2</sub> , HRTEM images of D) white and D) black TiO <sub>2</sub> [121].	30
Figure 2.11 Schematic illustration of various defects with local atomic structures in the photocatalysts [124].	31
Figure 2.12 a) Images and hydrogen evolution of TiO <sub>2</sub> nanoparticles treated under different conditions and b) UV-DRS measurement of TiO <sub>2</sub> nanotubes annealed in various reductive atmospheres [131].	33
Figure 2.13 Schematics of the synthesizing black TiO <sub>2</sub> nanotube via electrochemical reduction method [136].	34
Figure 2.14 a) Images of reduced TiO <sub>2</sub> nanoparticles treated with 2.5 (top), 1.5 (middle) and 0.5 (bottom) mmol of Zn powder, b) UV-visible absorbance spectra and c) H <sub>2</sub> evolution measurement of reduced TiO <sub>2</sub> nanoparticles obtained from different amounts of Zn powder in visible light region [139].	35
Figure 2.15 a) Schematic illustration reduction of TiO <sub>2</sub> in a two-zone tube furnace, b) images of black and white TiO <sub>2</sub> using Al-reduction method and c) UV-visible absorption spectra of pristine TiO <sub>2</sub> , hydrogenated black TiO <sub>2</sub> with high pressure (HP-TiO <sub>2</sub> ) and TiO <sub>2</sub> nanoparticles reduced at different temperatures (300°C, 400°C, 500°C) [137].	35
Figure 2.16 a) UV-visible-IR absorption spectra of pristine and plasma-reduced and high presurer hydrogenated TiO <sub>2</sub> and b) images of pristine and plasma-reduced TiO <sub>2</sub> [142].	36
Figure 2.17 HRXPS of Ti2p peaks pristine TiO <sub>2</sub> (a) and after 50 min (b), 5 h (c) Ion bombardment [144].	37
Figure 2.18 UV-vis absorbance spectra and b) valence band XPS spectra of pristine and sonicated TiO <sub>2</sub> nanoparticles for different h [146].	38
Figure 3.1 Schematic illustration of the a) the whole experimental set-up with an its real image (inset) and b) cross-section of the O-ring, Ti foil as a working electrode (anode) , Pt as counter electrode (cathode).	42
Figure 3.2 Schamatic illustration of the preperation of G-Pt NTs and G-NTs composite.	43
Figure 3.3 Schamatic illustration of Pt-SA catalyst process.	44
Figure 3.4 Schematic illustration of a) SEM microscope and b) the interaction of electron beam with sample [151].	45
Figure 3.5 Schematic illustration of X-ray generation through the incident electron beam.	46
Figure 3.6 Different component of TEM set-up [152].	47
Figure 3.7 Schematic illustration of XPS instrument [153].	48

Figure 3.8 representation of Bragg's law [154].	49
Figure 4.1 SEM images of MLNTs obtained at a) RT, b) 35°C, and c) 50°C (the anodization was carried out for 2 h by using a constant voltage of 60 V and an electrolyte consisting of 0.6 wt.% ammonium bi-fluoride salt (NH <sub>4</sub> F.HF), 96 ml diethylene glycol and 4 ml DI water.	55
Figure 4.2 Top and cross section SEM images of synthesized MLNTs for various anodization voltage a) 30 V, b) 40 V and c) 60 V. Top SEM images of MLNTs for d) 80 V and e) 100 V. (the anodization was performed in 0.6 wt.% ammonium bi-fluoride salt (NH <sub>4</sub> F.HF), 96 ml diethylene glycol and 4 ml DI water at 35°C for 2h).	56
Figure 4.3 Top and cross section (inset) SEM images of MLNTs for different anodization time a) 1h, b) 4h, and c) 6h (the anodization was conducted in 0.6 wt.% ammonium bi-fluoride salt (NH <sub>4</sub> F.HF), 96 ml DEG and 4 ml DI water at 60 V and temperature of 35°C).	57
Figure 4.4 Top and inset cross-section SEM images of nanotubes obtained in 0.6 wt.% ammonium bi-fluoride salt (NH <sub>4</sub> F.HF), 96 ml DMSO and 4 ml DI water at 35°C for 2h.	57
Figure 4.5 TEM images of a) the pristine cyanographene (G-CN) and b-d) after the formation and decoration with Pt nanoparticles (G-CN/Pt), (e) full XPS survey of G-CN and G-CN/Pt. The inset shows the atomic composition of G-CN/Pt. (f) HRXPS of the G-CN/Pt sample, showing the Pt 4f region.	60
Figure 4.6 Top SEM images with different magnification of: a-b) G-NTs, c-d) G-Pt-NTs.	61
Figure 4.7 a) Raman spectra of P-NTs, G-NTs and G-Pt-NTs samples (the inset shows the magnified Raman spectra), b) XRD analysis of TiO <sub>2</sub> nanotubes using cobalt X-ray source calcined at 450°C in air, c) UV-vis DRS measurement of P-NTs, G-NTs, and G-Pt-NTs samples, and d-f) HRXPS spectra of d) C1s, e) Ti2p (e), and f) Pt4f of G-Pt-NTs sample.	63
Figure 4.8 Photoelectrochemical response of composite samples obtained under 1 sun illumination (100 mW/cm <sup>2</sup> - AM1.5 G) in 1 M NaOH solution at different a) concentration of cyanographene and (b) electrodeposition time.	64
Figure 4.9 The effect of (a) G-CN concentration and (b) electrodeposition time on the PEC-WS.	64
Figure 4.10 a) Photoelectrochemical response of fabricated samples measured under 1 sun illumination (100 W/m <sup>2</sup> - AM1.5 G) in 1 M NaOH solution, b) corresponding IPCE spectra, and c) chronoamperometry test of G-Pt-NTs in 1 M NaOH solution, potential 1.5 V vs RHE for 7 h where the pH is 13.6 ( $E_{Ag/AgCl}^0 = 0.197$ V at 298 K, and $E_{Ag/AgCl}^0$ is the measured potential vs. Ag/AgCl).	66
Figure 4.11 a) The Nyquist plots demonstrating EIS spectra of P-NTs, G-NTs, and G-Pt-NTs samples obtained in 1 M NaOH solution at 1.5 V vs. RHE. The EIS at high frequency and the equivalent circuits used to fit the impedance spectra has shown in inset. b) Comparison of $\tau_{trans}$ of photogenerated electron for the pristine nanotube (P-NTs) and composite samples (G-NTs, and G-Pt-NTs) as a function of incident photon flux at 369 nm (monochromatic light). c) $V_{OCD}$ decay	

measurement of P-NTs, G-NTs, and G-Pt-NTs samples under 1 sun ( $100 \text{ W/m}^2$ –AM 1.5 G) illumination, and d) corresponding $\tau n$ . .....	70
Figure 4.12 a) Schematic illustration of synthesized TNTs. Top SEM images of b) as-synthesized TNTs and c) after post-treatment. (Anodization was performed in 0.15 M $\text{NH}_4\text{F}$ ethylene glycol and 3 wt. % DI water at 20V for 10 min, followed by 70 V for 10 min). .....	72
Figure 4.13 a) Schematic representation of synthesized TNTs. Top SEM images of b) as-synthesized TNTs and c) after post-treatment. (Anodization was performed in 0.2 M HF ethylene glycol and 4 wt. % DI water at 70 V for 30 min). .....	73
Figure 4.14 XRD patterns of pristine and sonicated TNTs using a cobalt X-ray source. ....	75
Figure 4.15 SEM image of samples: a) pristine synthesized $\text{TiO}_2$ (P-NT), b) sonicated sample for 50 min (R50-NT), and c) demonstrating cross section of P-NT. ....	76
Figure 4.16 a) UV-Vis DRS measurement of P-NT, R50-NT samples, b) bandgap energies calculation for P-NT and R50-NT, c) XPS valence band spectra of P-NT and R50-NT, d) schematic illustration of DOS for P-NT and R50-NT, and e) HRXPS spectra in the $\text{Ti}2p$ region for P-NT and R50-NT. ....	77
Figure 4.17 a) Photoelectrochemical measurement of TNTs samples sonicated for different time (from 30 to 80 min) under 1 sun illumination ( $100 \text{ mW cm}^{-2}$ - AM1.5 G) in 1 M NaOH solution, b) comparison of photocurrent density at 1.23 V for the corresponding samples, c) The Mott–Schottky plots of P-NT and R50-NT samples obtained at a frequency of 5KHz in the dark and d) corresponding IPCE spectra. ....	79
Figure 4.18 Nyquist plots representing electrochemical impedance spectra of P-NT and R50-NT samples. ....	80
Figure 4.19 a) TEM images of treated samples at various soaking time ranging from 1 to 60 min in very dilute hexachloroplatinic acid solution, b) HAADF-STEM image and c) the corresponding EDS elemental mapping of R50/Pt-NT10 sample. ....	81
Figure 4.20 a) EDS analysis of Pt-SA and Pt-NP decorated on the TNTs and b) Pt nanoparticles size distribution on TNTs for R50/Pt-NT60 sample. ....	81
Figure 4.21 a) Whole XPS survey spectra of sonicated TNTs at different impregnation time (10 and 30 min) in in the hexachloroplatinic acid solution, b,c) HRXPS spectra of $\text{Pt}4f$ for: b) sonicated TNTs for 50 min, followed by immersion in the hexachloroplatinic acid solution for 10 min, c) for 30 min and d) quantitative comparison of surface Pt on Pt-decorated TNTs. ....	83
Figure 4.22 a) Whole XPS survey spectra of Pt decorated samples for different impregnation times in dilute hexachloroplatinic acid solution; b, c, d) HRXPS spectra in the $\text{Pt}4f$ region of TNTs sonicated for 50 min, followed by immersion in the Pt solution for 1, 15 and 60 min (R50/Pt-NT1, R50/Pt-NT15 and R50/Pt-NT60), respectively. ....	84
Figure 4.23 HRXPS spectra in the $\text{Ti}2p$ region of sonicated TNTs for 50 min, followed by immersion in the Pt solution for 1, 10, 15, 30 and 60 min (R50/Pt-NT1, R50/Pt-NT10, R50/Pt-NT15, R50/Pt-NT30 and R50/Pt-NT60). ....	85

Figure 4.24 XRD pattern of Pt-SA and Pt-NP decorated samples.....	86
Figure 4.25 a) H <sub>2</sub> evolution of pristine, sonicated and Pt-decorated TNTs, b) Normalized H <sub>2</sub> evolution of Pt decorate sample, and c) reusability test of H <sub>2</sub> evolution of R50/Pt-NT10, sonicated for 50 min, followed by immersion in the hexachloroplatinic acid solution for 10 min .....	88
Figure 4.26 The mechanism of photocatalytic hydrogen evolution using ultrasound-reduced TNTs with embedded Pt single-atoms co-catalysts. ....	88

## List of tables

Table 2.1 Physical and chemical properties of anatase, rutile and brookite [56–58].	17
Table 4.1 Equivalent circuit components calculated by fitting the experimental electrochemical impedance spectroscopy data.	67
Table 4.2 The electron transfer time ( $\tau_{\text{trans}}$ ) of photogenerated electrons for the pristine and composite samples calculated through IMPS data analysis.	70



# Chapter 1: Energy and Photoelectrochemical water splitting

## 1.1 Introduction

Fossil energy reserves has been utilized extensively to meet most of the world's energy requirements and energy consumption for each nation is considered as a crucial driver of economic growth. In addition, continuous increase of environmental pollution threatens the global climate change because of tremendous emission of carbon dioxide (CO<sub>2</sub>) and other pollutants, which stem from combustion of fossil fuels. [1,2]. Essential challenging issues such as steady increasing the human population and energy demand in all the word along with depletion of fossil fuels cause the discovering of environmentally friendly fuels and efficient designing of energy storage devices. Therefore, for energy demand challenges, sustainable and clean renewable energy resources such as wind and solar energy can be employed as alternative energy sources [3,4].

## 1.2 Solar energy

Solar energy is considered as one of the most promising and unlimited source of energy to address this growing energy demand rate with lowest environmental pollution. The amount of energy coming to the land through the sun is about  $36 \times 10^3$  TW which only 1% of this amount of energy will be sufficient to tackle environmental pollution issue as well as to satisfy world's human population consumes in the year 2050 [5,6]. Moreover, the advantages of using solar energy compared to the conventional energy

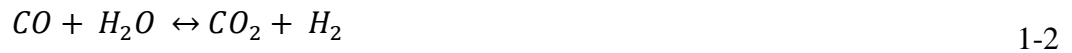
usage is consist of: (i) it is almost free because the payback times could be very short after the initial cost, (ii) reducing the level of greenhouse gases and pollutants and, (iii) it does not need nor power supply nor natural gas. Artificial photosynthesis, as solar-to-chemical energy convertors, by harvesting light can be used to produce high source of energy such as hydrogen ( $H_2$ ) or hydrocarbon via promising methods such as water splitting or carbon oxide reduction [2,6]. Among the various types of chemical fuels, hydrogen is one of the most significant candidate due to it can yield more energy per unit mass, which is 3-4 fold higher that than other fuels (120–142 MJ/kg) and can be utilized in fuel cells producing only water as the reaction product without any detrimental emission [7]. On the planet such as earth,  $H_2$  is almost always found as part of another compound, such as molecule of water ( $H_2O$ ), methane ( $CH_4$ ) or organic material, and it must be separated into pure  $H_2$  for use for instance in fuel cell electric vehicles. However, because of being a useful fuel,  $H_2$  safely has been utilized for decades in glass purification, in metallurgical process as  $O_2$  scavenger, metal treatment, petroleum refining, semiconductor manufacturing, fertilizer production and pharmaceuticals [2,8].  $H_2$  can be produced through a wide range of raw materials which is consist of gas and coal as a fossil source, as well as renewable sources using sunlight, such as water and biomass. In addition, numerous technologies with the long-term promise have been developed and will require financial support to fulfil their goals. However, in industry sector some of these technologies have been using for hydrogen production. In the next section, the main research activities for hydrogen production will be discussed.

### **1.3 Hydrogen production methods**

#### **1.3.1 Steam methane reforming**

Steam-methane-reforming is utmost process for  $H_2$  production in the industry. As a first step, methane such as natural gas with high-temperature steam ( $700^\circ C$  – $1,000^\circ C$ ) under 3–25 bar pressure (1 bar = 14.5 psi) in the presence of a catalyst is used to produce

synthesis gas (reaction 1-1) which is mixture of H<sub>2</sub> and carbon monoxide (CO). Followed by water gas shift reaction (WGSR), where the produced CO reacts with the steam to produce CO<sub>2</sub> and more H<sub>2</sub> (reactions 1-1 and 1-2). To obtain the pure H<sub>2</sub> in the final process system, all impurities and CO<sub>2</sub> will be removed from the gas stream.



Gasification also is one of the important path of H<sub>2</sub> production using fossil-based carbonaceous materials and biomass with high-temperature steam and oxygen (O<sub>2</sub>). In this process, for example, in the presence of O<sub>2</sub> and the steam at high temperature (>700°C), coal converts into CO, H<sub>2</sub>, and CO<sub>2</sub>. Subsequently, more H<sub>2</sub> is produced via a water-gas shift reaction, and then membrane can be employed to separate the pure H<sub>2</sub> from mixture gas stream [9,10].

### 1.3.2 Water electrolysis

As shown in Figure 1.1, electrolysis is the eco-friendly process to produce high purity of H<sub>2</sub> and O<sub>2</sub> as an only by-product (equation 3-1). However, it is not cost-effective and therefore less than 5% of necessary H<sub>2</sub> consumption can be produced by electrolysis [11,12].



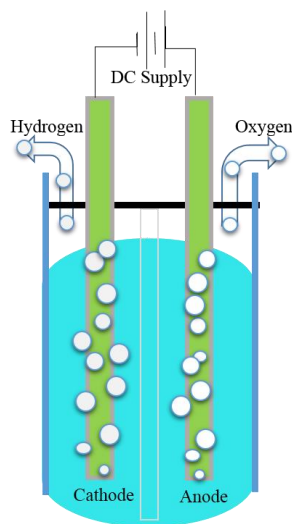


Figure 1.1 Water electrolysis process.

### 1.3.3 Photocatalysis

Photocatalysis is the acceleration of a photoreaction using a catalyst such as semiconductor material under light irradiation, which can continuously produce electron-hole pairs ( $e^-/h^+$ ) during the photochemical reaction. The photocatalytic reactions as it has been utilized in many chemical reactions can be categorized into two main types from thermodynamics point of view. Firstly, uphill reactions ( $\Delta G > 0$ , positive Gibbs free energy changes) where the material absorb light to perform the reaction such as  $\text{CO}_2$  reduction and water splitting. Secondly, downhill reactions ( $\Delta G < 0$ , negative Gibbs free energy changes) where the oxidation of many organic pollutants by oxygen would fit in this category (Figure 1.2). Irrespective of definition, the photocatalyst is considered based on properties such as light absorption, charge separation and charge transfer [13,14]. The search for a study of the light effect on chemical reactions began in early 1901 by Giacomo Ciamician [15]. In 1911 [13], the concept of photocatalysis was introduced when Alexander Eibner utilized Zinc oxide ( $\text{ZnO}$ ) and Prussian blue (the dark blue pigment) to bleach under illumination of light.

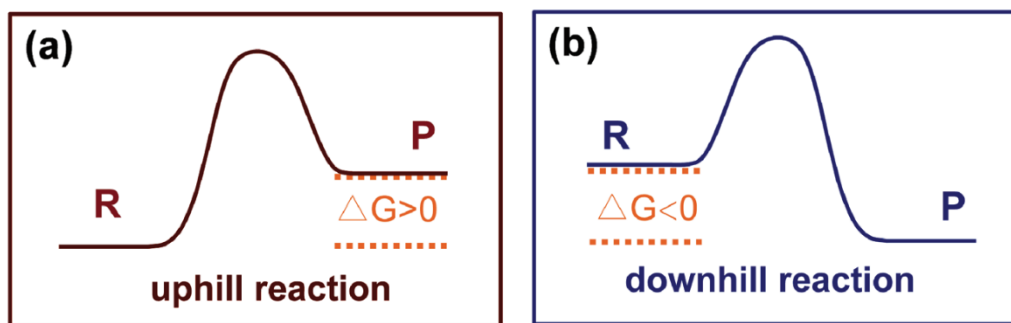


Figure 1.2 Thermodynamic illustration of a) uphill reaction and b) downhill reaction [13].

Later, in 1924 [13], based on previous experimental results, ZnO has been used to reduce silver ion under irradiation of light. Baly et al. [16] reported ferric oxide and colloidal uranium salt as catalyst under visible light to form formaldehyde. Later, an article was published regarding the utilization of  $\text{TiO}_2$  and  $\text{Nb}_2\text{O}_5$  for reduction of  $\text{ANO}_3$  and  $\text{AuCl}_3$  in 1932 [13]. Afterwards, in 1938 [13], Kitchener and Goodeve investigated  $\text{TiO}_2$  as a highly stable oxide. They found that after absorption of ultra violet (UV) light,  $\text{TiO}_2$  in the presence of oxygen can act as a photosensitizer and produce active oxygen species on its surface for bleaching dyes. In spite of much effort due to the lack of interest and absence of some practical application, there was a more than 20 years gap in any photocatalysis scientific work. However, the issue of energy crisis as well as its impact on environment was the milestone to encourage the scientists to think about alternative energy sources.

In 1972, Fujishima and Honda reported a breakthrough scientific research on photocatalysis of water, occurred in two-electrode electrochemical set-up using  $\text{TiO}_2$  and Platinum (Pt) under UV light irradiation [17–20]. In this set-up,  $\text{TiO}_2$  as an anode electrode could absorb the UV light in the way that the electrons pass through the external circuit to reach to the Pt as a cathode part to reduce the water to the  $\text{H}_2$ . Later, in 1979 [13], Fujishima and his colleague extended the application of photocatalysis by focusing on  $\text{CO}_2$  reduction using different inorganic semiconductor photocatalyst. Since then,

scientists have been concentrating on principle of photocatalyst mechanism, improve its efficiency and investigation new photocatalysts for various applications [13].

#### *1.3.3.1 Semiconductor and band diagram*

Nowadays, semiconductors due to their role in the fabrication of electronic devices, play an important role in our modern society. The developments in semiconductor technology during the last 50 years changed the world beyond anything that could have been imagined before them. Thanks to the semiconductors, electronic devices become smaller, faster, and more reliable.

The study of semiconductor materials began in the early 19<sup>th</sup> century. Typical semiconductor material such as silicon (Si), Germanium (Ge), and combination of groups III and V of periodic table elements (GaAs) have been characterized by its bandgap. The bandgap can be defined as an energy gap or forbidden energy region between the completely full band of electron (valence band or VB) and partially/quite-empty one (conduction band or CB) [21,22]. Electrons through optical or thermal excitation can cross this gap. The bandgap in semiconductor material is ranging between 1 and about 3.5 eV. While, the bandgap in insulator material is too large and it is about larger than 4 eV, there is no gap between the VB and CB in metal (Figure 1.3) [23].

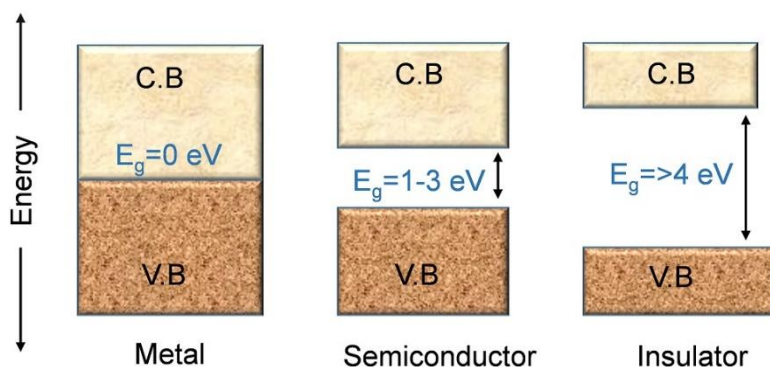


Figure 1.3 Energy band diagram demonstrating different band gap energies.

Photocatalytic property is observed when semiconductors absorb light at a wavelength equal or greater than to the material's band gap. Consequently, VB electrons are promoted through the bandgap into the CB, and leaves behind the electron-holes in the VB [24,25]. The bandgap energy diagram of some most common semiconductors are presented in Figure 1.4 [26].

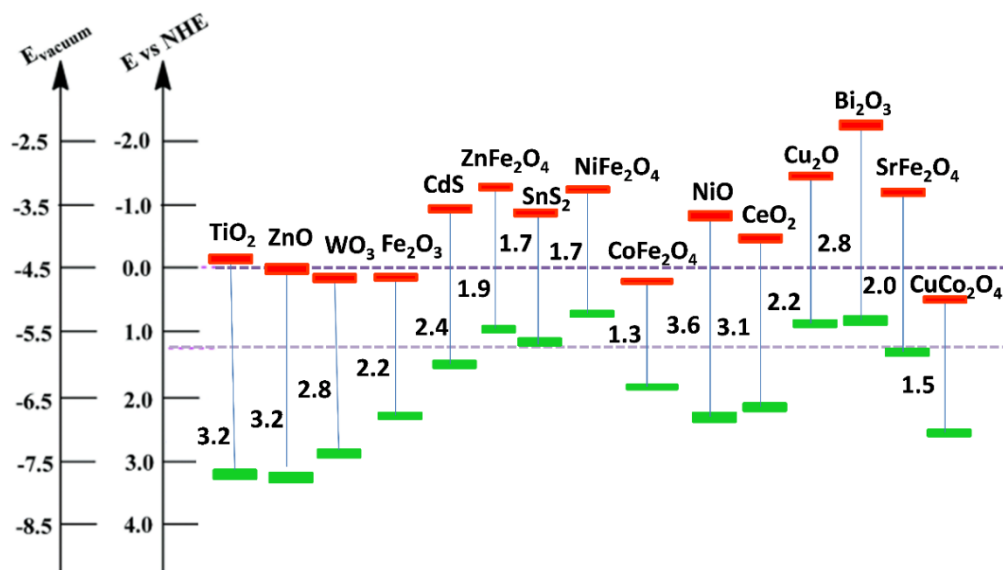


Figure 1.4 The band edge potentials and band gaps of different semiconductors [26].

According to the literature, the most widely accepted formation mechanism for all semiconductors during the light absorption involves four stages (shown in Figure 1.5): (i) light absorption to generate electron-hole pairs; (ii) separation of photo-excited charges; (iii) transfer of electrons and holes to the surface of photocatalyst; and (iv) oxidation and

reduction (redox) reactions based on the utilization of charge carriers on the surface of photocatalyst [13,27,28]. There is the undesirable charge carrier recombination either on the surface of catalyst or on route to the surface. The recombination of excited charge release the energy obtained from excitation in the form of heat (non-radiative recombination) or light emission (radiative recombination) [14].

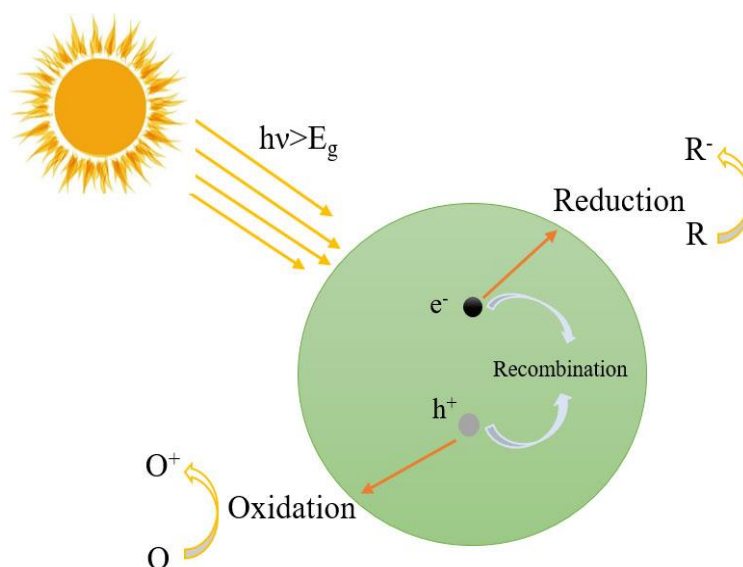
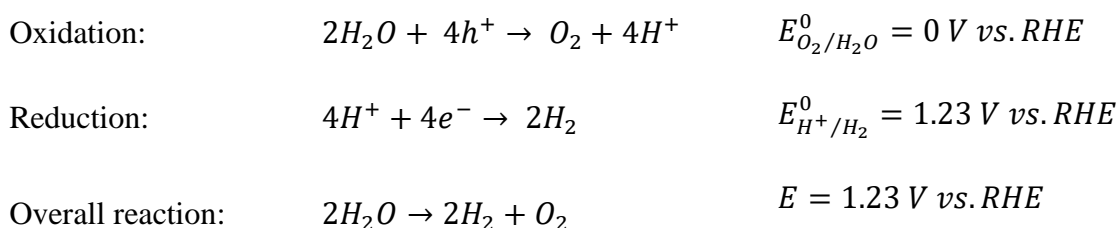


Figure 1.5 Schematic illustration of photoexcited electron-hole pairs on a semiconductor and possible recombination and reaction path.

As we discussed earlier, there have been variety methods to produce  $H_2$ . However, photocatalysis has been considered as cost-effective and environmentally friendly approach to split water for  $H_2$  evolution. Overall, the energy of the photons can be converted to the chemical energy via combination of oxidation and reduction process as follows [28–30]:



Based on an overall reaction,  $H_2$  evolution through water splitting is endothermic which the Gibbs free energy for this reaction is 237.2 KJ/mol of  $H_2$  produced. In addition, there have been two necessary requirements that affect  $H_2$  production. Firstly, due to the overpotential needed for  $O_2$  and  $H_2$  production, actual energy of  $1.26 < E_g < 2.4$  eV is required to achieve water splitting reaction. Secondly, the band edge positions must straddle the  $H_2$  and  $O_2$  redox potential and the CB of semiconductor should be more negative than potential of  $H_2$  evolution and the valence band edge more positive than potential needs to oxidize the water. Based on the main aforementioned steps for semiconductor, migrated charge to the surface may oxidize/reduce adsorbed water molecules, producing  $H_2$  molecules (Figure 1.6) [28,31].

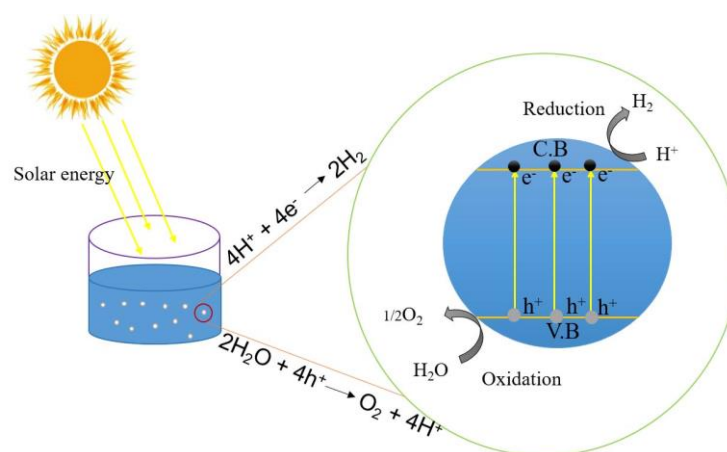


Figure 1.6 Schematic illustration of the hydrogen production via water dissociation mechanism on semiconductor.

### 1.3.4 Photoelectrocatalysis

The concept of photoelectrocatalysis, which is combination of photoelectrochemical technique with heterogeneous photocatalyst, can be referred to the photoelectrochemistry. Photoelectrochemical (PEC) water splitting is one of the most promising method for production of highly clean and sustainable  $H_2$  [2,13]. The photoelectrochemical is consist of two electrodes immersed in aqueous electrolyte solution. Reduction of water into  $H_2$  and  $O_2$  generation occur on the surface of photoanode and photocathode respectively.

During the photoelectrochemical water splitting (PEC-WS), photogenerated electron (or holes) migrate to the cathode (or anode) to participate in  $H_2$  (or  $O_2$ ) evolution reactions (HER and OER, respectively). These charge carriers that promote redox reactions are generated in semiconductor upon absorption of light [32–35]. Generally, PEC-WS offers some beneficial issues compared to the conventional photocatalysis. On one hand, on the nanoscale photocatalyst's setup the close vicinity of oxidation and reduction site increases product crossover. Therefore, for photoelectrocatalysis much higher efficiencies than powdery photocatalysis setup are expected. On the other hand, PEC techniques can provide better characterization tools to understand and characterize photocatalyst in quantitative way which will be discussed in the next section [13]. As shown in Figure 1.7, upon illumination the electron and holes are generated ( $e^-/h^+$ ). The electron and holes then separated and holes in the valence band diffuse/migrate towards the surface of semiconductor where OER occurs. Simultaneously, electron promotes to the semiconductor conduction band and transported towards semiconductor's back contact and through the external circuit to the surface of counter electrode to drive the HER [2].

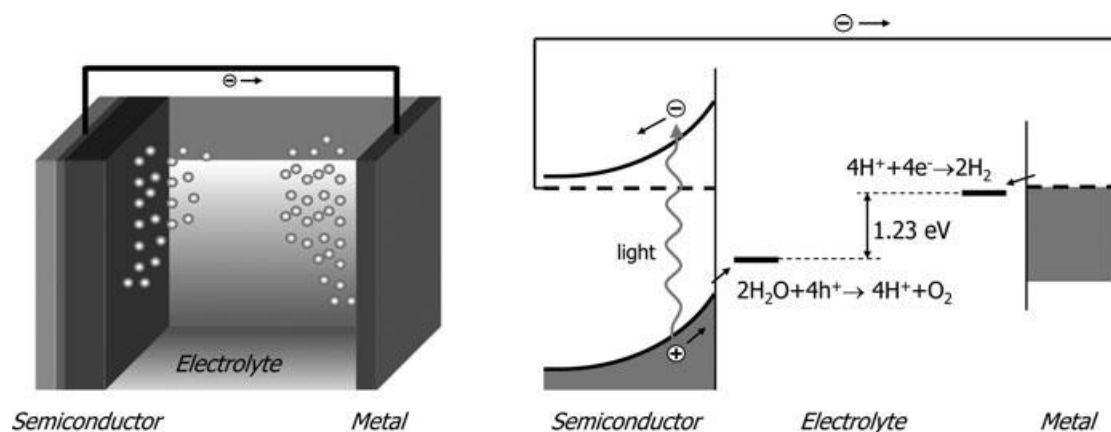


Figure 1.7 Illustration schematic of a photoelectrochemical cell that involves of a semiconducting photoanode and a metal cathode [32].

While PEC water splitting is powerful technique, it seems complex process for direct splitting water into  $H_2$  and  $O_2$  efficiently. For this reason, it must be met several key criteria simultaneously: (i) the band gap should be small enough for absorption of

significant portion of solar spectrum, (ii) the semiconductor photocatalyst must generate adequate voltage level upon irradiation to split the water molecule, (iii) the semiconductor should have straddled band edge positions with respect to water redox potentials, (iv) the semiconductor must show photocorrosion resistance in aqueous electrolyte and facile charge transfer from the surface of semiconductor to the solution ions to minimize the energy losses [32]. For practical H<sub>2</sub> production, the cost-effective materials, which can satisfy all above requirements process has not been reported yet.

#### 1.3.4.1 Estimation of the PEC water splitting efficiency

The energy conversion efficiency is ultimate performance indicator of PEC-WS cell for promoting the advancement of this technology. Photoconversion efficiency can be measured under irradiation of artificial light sources such as xenon (Xe) lamp. While the intensity and spectrum of solar light reaching the ground highly depend on the weather conditions and the time of day, the intensity of artificial sources remain constant with time during its lifetime. Several measures are mainly used to determine the efficiency of material for PEC-WS, which will be discussed in the following [36–40].

The standard solar-to-hydrogen conversion efficiency (STH) is the most important approach for calculating PEC-WS performance. It can be explained as a ratio between the total energy generated to the solar energy input. The PEC device for STH measurement is measured in 2-electrod system and requires solar AM 1.5G illumination, under zero bias voltage between working electrode (WE) and counter electrode (CE).

$$STH = \frac{\text{Total energy generated}}{\text{Total energy input}} = \frac{\Delta G \times r_{H_2}}{P_{sun} \times S} \quad (1.1)$$

Where  $r_{H_2}$  is the rate of H<sub>2</sub> production in moles per second, measured with mass spectrometer or gas chromatograph,  $\Delta G$  is the Gibbs free energy (237 KJ mol<sup>-1</sup>),  $P_{sun}$  is

the power density of illuminated light ( $100 \text{ mW cm}^{-2}$ ) and  $S$  is the illuminated electrode area ( $\text{cm}^2$ ).

When an external bias is applied to the PEC system, the current extracted from the cell is higher compared to the bias-free condition of STH measurement; therefore, the electrical energy must be subtracted. The applied bias photo-to-current efficiency (ABPE) is determined:

$$ABPE = \frac{P_{out} - P_{in}}{P_{light}} = \frac{J_{ph} (V_{redox} - V_{bias})}{P_{light}} \quad (1.2)$$

Where  $P_{light}$  is the light intensity ( $100 \text{ mW cm}^{-2}$ ),  $J_{ph}$  photocurrent density under  $V_{bias}$ ,  $V_{redox}$  is redox potential (1.23 V vs. NHE) for water splitting,  $V_{bias}$  is actual potential difference between the working and counter electrode.

The incident photon-to-current efficiency (IPCE) is another possibility of assessing the performance of photoelectrode for water splitting. The IPCE is calculated as the percentage of the incident photon flux that is directly transformed into the photocurrent as function of the incident photon.

$$IPCE = \frac{\text{Total energy of converted electrons}}{\text{Total energy of incident photons}} = \frac{\left(\frac{J_{ph}(\lambda)}{e}\right) \times \left(\frac{hc}{\lambda}\right)}{P(\lambda)} \times 100\% \quad (1.3)$$

Where  $J_{ph}$  is the photocurrent density measured at specific wavelength ( $\text{mA cm}^{-2}$ ),  $e$  is the electronic charge,  $h$  is Plank's constant,  $c$  is speed of the light, and  $P(\lambda)$  is the incident light intensity at that specific wavelength ( $\text{mW cm}^{-2}$ ).

Finally, in the calculation of IPCE, optical losses caused by reflection and/or transmission of photons are neglected. Therefore, the absorbed photon-to-current conversion efficiency (APCE) can be obtained by correction these optical losses. The

APCE is expressed as number of photogenerated charge carriers contributing to the photocurrent per absorbed photon, that is:

$$APCE = \frac{IPCE(\lambda)}{A(\lambda)} = \frac{IPCE(\lambda)}{1 - R - T} \times 100\% \quad (1.4)$$

Where A, R, T are the optical absorption, reflection, and transmission, respectively. Regarding the various semiconductors introduced in Figure 1.4 those that are thermodynamically feasible for water splitting are ZnO, TiO<sub>2</sub>, SiC and CdS. For these reasons and its high chemical stability, TiO<sub>2</sub> has considered as one of the promising semiconductor candidate for this purpose, which will be discussed in the next chapter.



## Chapter 2: TiO<sub>2</sub> for water splitting application

### 2.1 Titanium dioxide (TiO<sub>2</sub>) as a benchmark photocatalyst

Among various types of metal oxide semiconductors ( $\alpha$ -Fe<sub>2</sub>O<sub>3</sub>, ZnO, WO<sub>3</sub>, etc.), TiO<sub>2</sub> has been one of the most widely used materials for the PEC application owing to many beneficial properties, including chemical and mechanical stability, photocorrosion resistance, favourable band edge positions, and low cost [7,41–43]. In 1964, Kato et al. reported photocatalytic oxidation of tetralin by a suspended TiO<sub>2</sub>. Later, McLintock et al. further studied the photocatalytic oxidation of propylene and ethylene in the presence of adsorbed oxygen on the surface of TiO<sub>2</sub> [44]. In the 1970s, Fujishima and Honda demonstrated the most important discovery in the area of photocatalysis, using photoexcited TiO<sub>2</sub> to dissociate water into H<sub>2</sub> and O<sub>2</sub> in a photoelectrochemical cell configuration. Considering the photocatalytic activity property, TiO<sub>2</sub> nanostructure attracts wide scientific interest in view of their applications in photocatalytic water splitting, environmental protection procedures such as, air and water purification, gas sensors, solar cell, cancer cell killing, hip and dental implant, and ion change [45,46]. As shown in Figure 2.1, TiO<sub>2</sub> has three major crystalline forms in the bulk or nanoscale namely anatase, rutile and brookite [47]. The most thermodynamically stable phase at ambient temperature and pressure in macroscopic sizes form of TiO<sub>2</sub> is rutile, while anatase is more stable in nanoscopic sizes. TiO<sub>2</sub> consists of Ti<sup>4+</sup>-ion at the centre that

surrounded with six O<sub>2</sub>-ions. However, rutile and anatase TiO<sub>2</sub> have distinct densities and average Ti<sup>4+</sup> distance differ for those structures, which affects their thermodynamic stability. All physical and chemical properties of these three crystalline phases are presented in Table 2.1. It is worth to mention that a number of experiments show that at temperatures higher than ca. 300°C TiO<sub>2</sub> structure can be transformed to anatase phase. At temperature 700-1000°C, the phase transition anatase to rutile take place which is depends on impurities and crystallite size [48,49]. Brookite is the rarest naturally occurring form of TiO<sub>2</sub> and is challenging to synthesize in pure form. However, many parameters can be influenced in the phase transitions among these three phases such as pH of solution, particle size, surface energy, and solution chemistry [50]. For example, for the equal particle sizes of the three phases, the most thermodynamically stable phase for crystal sizes below ca. 11 nm, 35 nm and exceeding 35 nm, anatase, rutile and brookite are most stable, respectively [50]. The band gap of rutile is 3.0 eV, which is smaller than that other TiO<sub>2</sub> crystalline phase (3.2 eV for anatase and 3.3 eV for brookite). However, due to the high recombination rate of electron-hole in rutile, it is not suitable candidate for photocatalysis reaction [51]. Furthermore, it is reported that brookite nanocrystals demonstrate higher photocatalytic activities compared to those rutile and anatase [52–55].

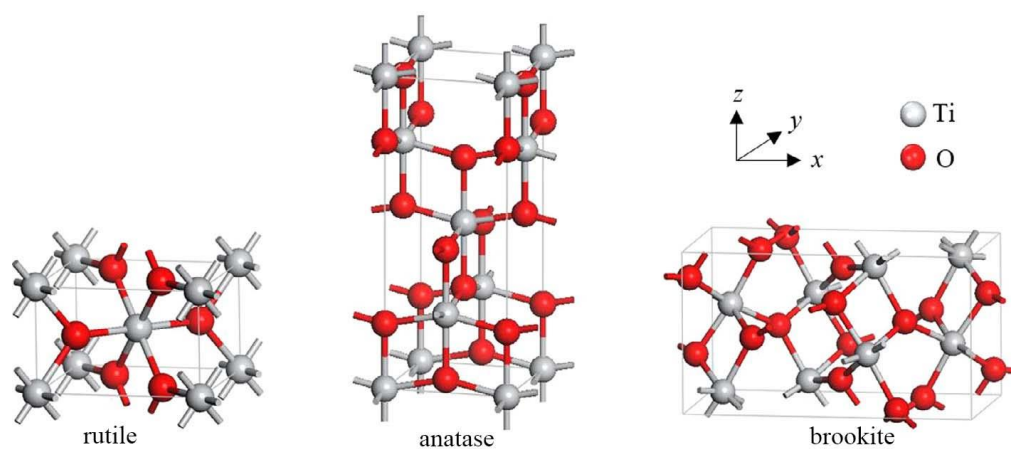


Figure 2.1 Crystal structures of TiO<sub>2</sub> (spheres: red—O<sub>2</sub>, grey—Ti) [47].

Table 2.1 Physical and chemical properties of anatase, rutile and brookite [56–58].

Properties	Anatase	Rutile	Brookite
Crystal structure	Tetragonal	Tetragonal	Orthorhombic
Lattice constant (Å)	a = 4.5936 c = 2.9587	a = 3.784 c = 2.9587	a = 9.184 b = 5.447 c = 5.154
Density (g/cm <sup>3</sup> )	3.89	4.52	4.18
Melting point (°C)	1825	1840	1843
Semiconductor type	n-type	n-type	n-type
Standard heat capacity C <sub>p</sub> (J/KgK)	55.52	55.06	56.2
Refractive index (η <sub>a</sub> )	2.56	2.94	2.58

## 2.2 TiO<sub>2</sub> nanostructuring

The size of the material has a great influence on its properties. There is no big difference in materials properties in their bulk and microscale. However, the properties changes considerably when the particle reaches a size blow 100 nm, compared to its bulk state. Significant features of nanomaterial, affecting in photocatalytic application are: (i) increasing effective surface area, which is popular for improving photocatalytic reactions by adsorbing more reactants in semiconductor-electrolyte interfaces, (ii) more efficient charge-carrier separation, and (iii) adjustment of band-bending, surface state and flat-band potential with expose specific crystal facets to the light. Moreover, it has been reported that the photocatalytic activity of TiO<sub>2</sub> nanostructures is related to their size, specific surface area, morphology and synthesis method of nanomaterials [45]. One-dimensional (1D) TiO<sub>2</sub> nanotubes (TNTs) have been extensively investigated over the last decade, due to their favourable properties to outperform their bulk counterparts in photocatalytic activity. For instance, TNTs generally provide a high aspect ratio that significantly enlarges the surface area and the light harvesting efficiency as well as an increased number of catalytic centres [7,59]. Moreover, the drawback of the electron–

hole recombination can be significantly suppressed due to the fast and directional pathway (along the axial direction) of photogenerated electrons [7]. Various methods have been developed to synthesize TNTs, including template synthesis, sol-gel or a hydrothermal method [7,60,61].

### **2.2.1 Hydrothermal method**

Among various synthesis methods, hydrothermal method is straightforward approach for chemical processing, leading to fabrication of high purity and good dispersibility for synthesizing 1D TiO<sub>2</sub> nanostructures (TNTs). It is a technique of crystallizing a metal oxide in an aqueous solution at high pressure and temperature. Teflon autoclave within a stainless-steel vessel is used to keep the solution in furnace or oil bath at higher temperature 100°C (i.e., boiling point of water at 1 atm). Kim and co-workers reported that the 1D TiO<sub>2</sub> nanotubes growth by hydrothermal method that they treated titanium precursor with 10M NaOH solution followed by a heat treatment in an autoclave for 48 h [62]. Interestingly, Bahnemann et al. [53] reported the growth of brookite TiO<sub>2</sub> nanorods using titanium bis (ammonium latate) dihydroxide (TALH) precursor with combination of high concentration of urea at 140°C for 24 h. Over the past years several parameters have been considered to produced desired morphology including, reaction temperature, reaction time, various Ti precursor, and concentration of alkali solution [45,63].

### **2.2.2 Anodization method of TiO<sub>2</sub> nanotube synthesis**

Electrochemical anodization technique is one of the most affordable and convenient method to obtain highly order and uniform arranged nanotubes perpendicular to the substrate. This method could provide a high degree of control over the length and diameter of nanotubes. Self-organized growth of TiO<sub>2</sub> nanotubes layer via anodization of titanium (Ti) in chromic acid electrolytes was investigated for the first time by Zwilling in 1991 [64]. Later, Gong et al. [65] reported the synthesis of self-organized TiO<sub>2</sub> nanotube arrays by anodization of Ti foil in an aqueous electrolyte (H<sub>2</sub>O/HF) with length

of approximately 500 nm at room temperature. In this process, the metal (i.e., Ti, Al, Zr) is immersed in an electrolyte and acts as the anode of an electric circuit. Then, the DC electric field drives the migration of metal and oxygen ions in the electrolyte bath (Figure 2.2). The corresponding mechanism of tube formation through anodization of Ti foil can be verified via SEM and current-time curve during the fabrication of TiO<sub>2</sub> nanotubes. The formation of TiO<sub>2</sub> nanotubes can be described because of competition between formations of the anodic oxide layer under applied electric field (equations 2-1 and 2-2) and chemical assisted dissolution rate of the forming oxide (equation 2-3). This can be regarded as dissolution promoted by the presence of fluoride ions (F<sup>-</sup>), which is an vital parameter for the formation of tubular structure because of its ability to form soluble hexafluoro titanium complex ([TiF<sub>6</sub>]<sup>2-</sup>) [66–71].



In the presence of F<sup>-</sup> dissolution/complexation of Ti<sup>4+</sup> as [TiF<sub>6</sub>]<sup>2-</sup> can be formed according to the following reaction as well:



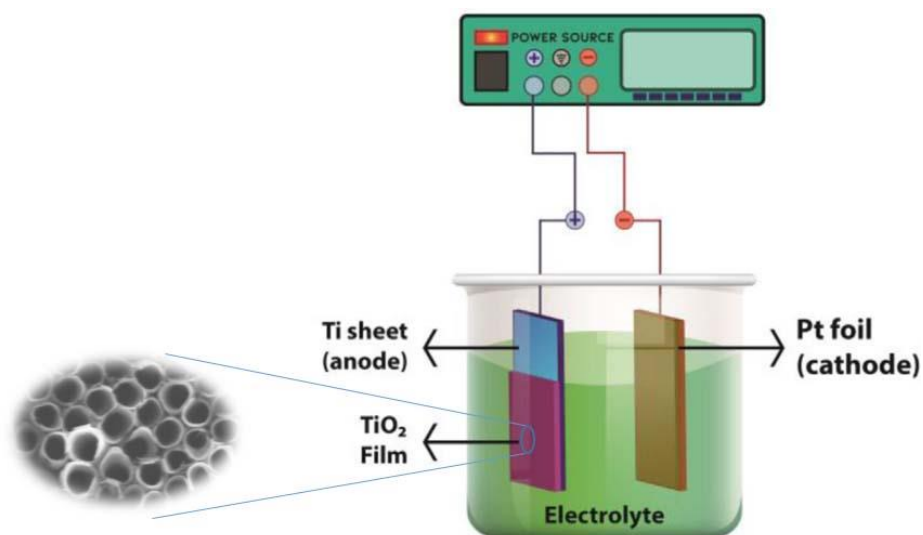


Figure 2.2 Anodization set-up for synthesizing the nanotubes [66,67].

A schematic illustration of the reaction phenomena occurring in fluoride containing media is shown in Figure 2.3a. The electric field drives  $\text{Ti}^{4+}$  ions from the Ti substrate towards the electrolyte-oxide interface, which results in the thickening of the grown of oxide layer. Totally, oxide layer is grown either at the oxide/metal or oxide/electrolyte interface based on  $\text{Ti}^{4+}$  and  $\text{O}^{2-}$  ions migration rate, where  $\text{Ti}^{4+}$  ions combine with  $\text{F}^-$  ions to form a water-soluble titanium hexafluoride species ( $[\text{TiF}_6]^{2-}$ ). The  $\text{OH}^-$  and  $\text{O}^{2-}$  anions stem from the dissociation of water and  $\text{F}^-$  with the high diffusion coefficient, migrate towards the anode interface to form a fluoride-rich layer at the metal–oxide interface. The presence of  $\text{F}^-$  ions in appropriate concentration play vital role for pore formation in the substrate, results in partially dissolving the oxide (Figure 2.3b). When the formation of oxide layer and dissolution rated reach at equilibrium under several key factors such as pH, fluoride content, anodizing potential and time, and temperature the nanotubular TiO<sub>2</sub> structure can be formed. It is worth mentioning that O<sub>2</sub> and H<sub>2</sub> bubbles are evolved at the anode and cathode, respectively [68,70–72].

Figure 2.3c demonstrates the current density versus time (I-t) curve of anodization process of TiO<sub>2</sub> nanotubes in the presence of F<sup>-</sup> ions in the electrolyte. This curve can be divided into three sections during the anodization: (i) due to the formation of compact oxide layer current density decrease dramatically; (ii) moderate increase of current can be seen because of formation of nanopores through etching of oxide layer; (iii) stable nanopores growth occur and the current density remained the same value [68,73].

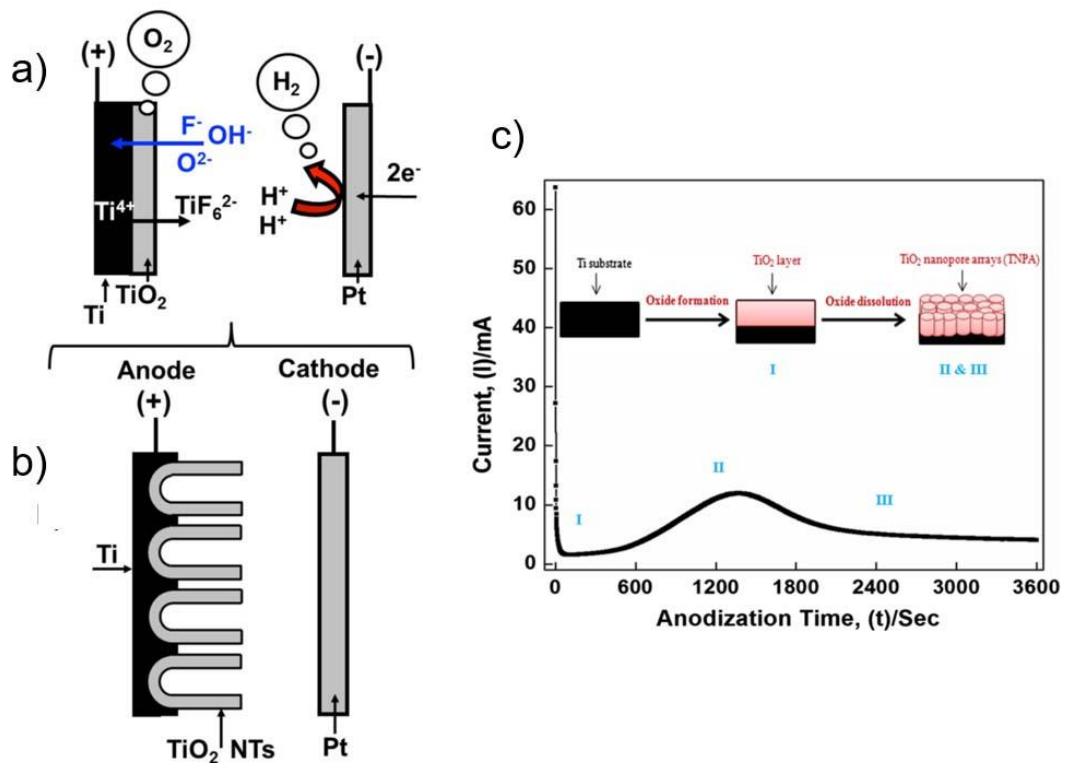


Figure 2.3 a) Schematic illustration of anodization at the metal-oxide interface indicating ions migration processes during the anodization of Ti b), formation of TiO<sub>2</sub> NTs, and c) I-t at different stages: (I) formation of compact oxide layer, (II) nanopore formation, and (III) self-ordering of TiO<sub>2</sub> nanotubes [72,73].

### 2.3 Modifications of TiO<sub>2</sub> nanostructures

TiO<sub>2</sub> as one of the most widely used materials for the PEC application offers some advantages such as higher stability over the various range of pH values in aqueous solution upon illumination for PEC-WS. However, it also suffers from a few significant drawbacks that restrict its broader practical application. These are mainly low efficiency

under solar light activation in visible region, which accounts less than 5% of the solar spectrum due to its wide bandgap energy and a relatively high recombination rate of the charges [74,75]. Consequently, considerable effort has been focused in literatures on improving the main drawbacks, aiming at enhance the photoactivity activity of TiO<sub>2</sub>. In the next section, some of these methods will be briefly discussed.

### 2.3.1 Non-metal doping

TiO<sub>2</sub> doping with non-metal or metal ions can enhanced poor absorption in visible light or its activity in the UV region. Several non-metal ions such as carbon (C), nitrogen (N), and sulphur (S) have been used to dope TiO<sub>2</sub>, and then its product were investigated for their optical and photocatalytic properties through the years [76–80]. Although, these dopants are less likely to form donor levels in the band gap area, they revealed an upward shifting of valence band edge as shown in Figure 2.4. Chen et al. demonstrated using C-, N-, and S-doped TiO<sub>2</sub> results in additional electronic states above the valence band edge of TiO<sub>2</sub>. This observation can be described as a redshift of the catalyst's potential. A broad light absorption in the visible region and extensive utilization of a solar spectrum is observed by a reduction in the band gap. Furthermore, the “shoulder” and “tail-like” features can be visible in the UV-vis spectra as well (Figure 2.4c) [81].

Among all the other anion-doped forms (C and S), N-doped TiO<sub>2</sub> as one the most frequently used non-metal dopants, has been widely investigated in the literatures. Siuzdak et al. reported that the vertical and highly ordered N-TiO<sub>2</sub> nanotubes composite using electrochemical method, which the presence of N in TiO<sub>2</sub> lattice was confirmed by spectroscopic technique. The results showed that the suppression of electron-holes recombination rate and enhancing the photocatalytic activity of fabricated TiO<sub>2</sub> [82]. In some papers, the TiO<sub>2</sub> modification with carbon-base are also presented. For instance, Shi et al. [83] reported synthesizing of different carbon nano-composites, such as C-doped TiO<sub>2</sub>. More complex carbon-base structures including multi-walled carbon nanotubes

(MWCNT) in TiO<sub>2</sub>-SiO<sub>2</sub>/MWCNT and carbon dots (Cdots) in C/N-TiO<sub>2</sub> have been reported as well [84,85].

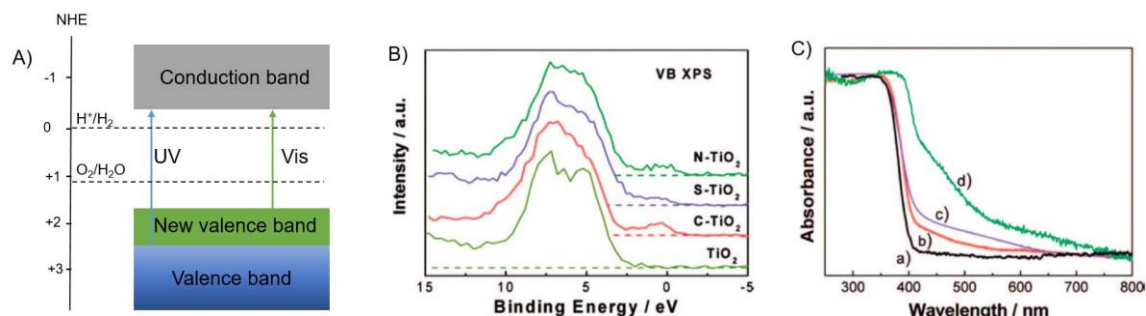


Figure 2.4 A) Schematics illustration of the new-formed valence band structure by using non-metal dopants. B) Valence band XPS and C) Uv-vis spectra of a) pure TiO<sub>2</sub>, b) C-TiO<sub>2</sub>, C) S-TiO<sub>2</sub> and d) N-TiO<sub>2</sub> [81].

### 2.3.2 Metal doping

Doping using metal is another most effective way to obtain visible-light activity of TiO<sub>2</sub> and lifetime prolongation of the charge carriers. Metal doping such as Ag, Ni, Co, Au, Cu, Ru, Fe, Pt, etc can increase the efficiency of TiO<sub>2</sub> by acting as an electron trap, thereby suppressing the electron-hole recombination [86–88]. Over the past few decades, there have been numerous studies on the band gap correction of photocatalyst including TiO<sub>2</sub> using impurity levels in the forbidden band structure to make them visible light active. As shown in Figure 2.5 metal ion doping creates either acceptor level below the conduction band or donor level above the valence band to form much more active photocatalysts in the whole light spectrum [81].

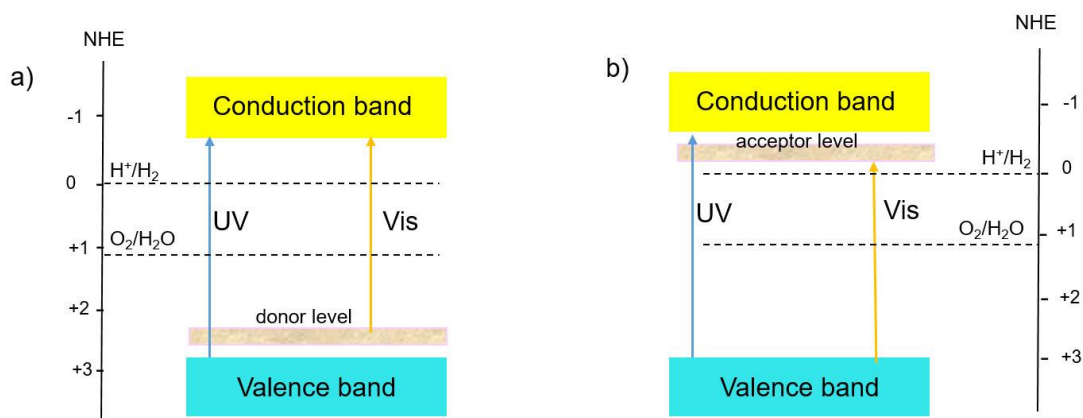


Figure 2.5 Metal-doped photocatalyst a) donor level and b) acceptor level [81].

### 2.3.2.1 Noble metal decoration

It is believed that three vital sequential steps effect on photocatalyst particles in photocatalysis reactions: (i) excitation of  $e^-h^+$  pairs in the particles via absorption of photons with higher energies than the bandgap of the photocatalysts, (ii) separation and migration of photogenerated electrons and holes, and (iii) chemical reactions at surface based on these carriers [89,90]. Therefore, noble metals can act as a mediator through the crating junctions to facilitate electron transfer and as reaction sites enhance the photocatalytic H<sub>2</sub> production efficiency. Noble metals might be loaded as the co-catalysts owing to unique properties including lower overpotential, better conductivity, and higher catalytic activity for H<sub>2</sub> evolution in comparison with the semiconductors. The work function  $\Phi$  (minimum energy required to transfer of an electron from fermi level to the vacuum) of TiO<sub>2</sub> is about 4.2 eV which is smaller than of work function of many noble metals (e.g., Pd, Pt and Ru are 5.55, 5.65 and 4.64 respectively) [91]. Since many semiconductors have intrinsically low kinetics and catalytic ability for HER or OER, co-catalysts are loaded on the surface of semiconductors to drive those reactions. Otherwise, they are less favourable due to inefficient consumption of charges carrier. While water splitting thermodynamically is an uphill reaction, co-catalysts on the semiconductor also

reduce the overpotential or activation energy of reactions, thereby promoting the photocatalytic performance as shown in Figure 2.6 [91].

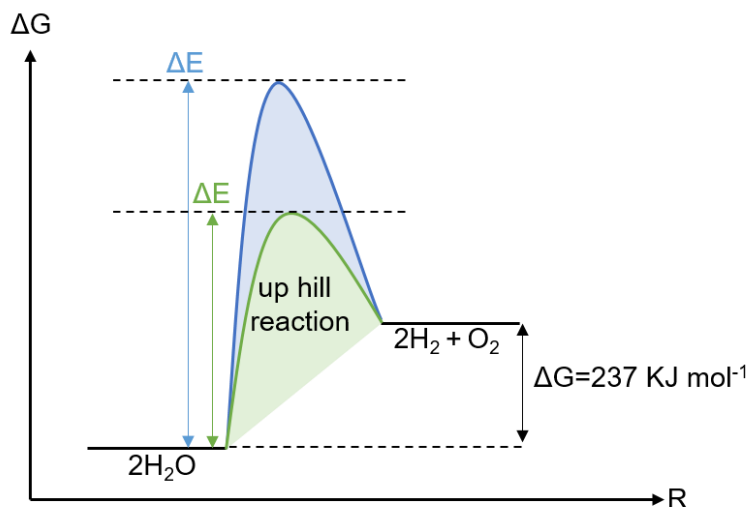


Figure 2.6 Illustration of energy diagram for PEC-WS with and without co-catalyst.

Catalytic activity of metals (or noble metals) for H<sub>2</sub> evolution is a periodic function of their atomic numbers. It is reported that, the activity of metal is increased by an increase in the number of d electrons (metal's electron configuration). It reaches to the highest level at nearly completed d orbitals (d<sup>8</sup> configuration), followed by sudden decrease when s orbital is completed [92].

Based on aforementioned methods to suppress electron-hole recombination on TiO<sub>2</sub>, junction of TiO<sub>2</sub> with the noble metal might be able to facilitate an efficient electron transfer at the surface of TiO<sub>2</sub>, which offers superior H<sub>2</sub> evolution activity. The volcano plot shows the relationship between the exchange current for H<sub>2</sub> evolution and the M–H bond strength [93]. It can be seen that the Pt-group metals (Pt, Ru, and Ir) possess appropriate surface properties and will be the most interesting catalysts for the HER reaction. Among them, Pt is the best performing catalyst discovered for this purpose until now. This is owing to the formed Pt–H bonds with ideal bond strength. This bond is strong enough for easy adsorption and reduction of H<sup>+</sup> ion as well as weak enough for

facile releasing of H<sub>2</sub> when reduction is complete. This unique feature of Pt can place it at the top of the volcano plot [35,93].

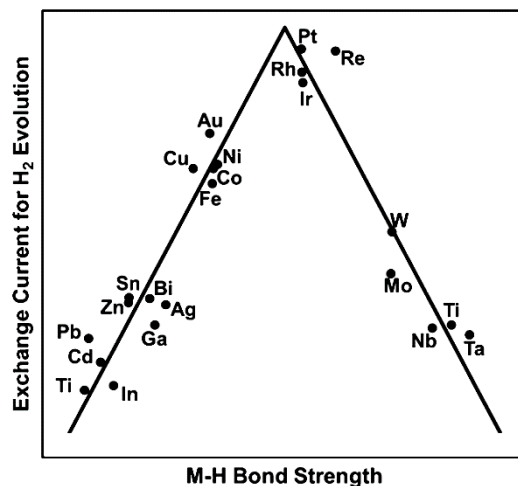


Figure 2.7 Volcano plot showing the relationship between the exchange current and the M-H bond strength [93].

#### 2.3.2.1.1 Single atom (SA) decoration

Loading co-catalyst on the surface of substrate not only suppress charge carrier recombination rate by trapping electrons, but also provides an appropriate place for effective reduction of proton, and therefore significantly improves the photocatalytic activity. Zhang et. al [94] in 2011 proposed single-atom catalysis (SACs) for the first time and has recently introduced with atomically dispersed metals as an interesting approach. Using this unique class of heterogeneous catalysts offers the opportunity to the 100% of metal atom utilization in catalytic reactions, performing the construction of inexpensive catalyst by thrifting the use of precious metals such as Pt, Au, Rh and Pd [94]. Thus, great effort has been dedicated on this strategy by embedding the single atoms into supported catalysts as well as control of synthesis parameter to tune interaction between atoms and thereby providing highly active SA catalysts. Using SACs have shown excellent catalytic performance in water–gas shift reactions [95], CO oxidation [96], photocatalytic activity for H<sub>2</sub> production [97] and so on. Despite their high effectivity, single-atom catalysts need further optimization to mitigate serious aggregation or coarsening during the catalytic

reaction process in terms of their instability. As shown in Figure 2.8a, materials can be categorized into the bulk, nanoparticles, subnanoclusters, and single atoms. For instance, by reducing the size of metal, it works differently because of the larger proportion of atoms at their surfaces as well as an increase of unsaturated coordination environment of the metal species. Consequently, there are an increase in the surface free energy of the metal components which results in chemical interactions with the support and adsorbates through the highly metal active sites. In the extreme case of SACs, due to the quantum confinement of electrons and highly active valence electrons, the surface free energy of metal species reaches highest point, promoting chemical interactions with the support [98]. Unsaturated coordination sites along with high activity and selectivity, as well as remarkable efficiency are some merits of SA catalyst compared to the its nanoparticles and nanocluster counterparts. The chemical nature of the supported single metal atoms forcefully depends on their interactions with the support surfaces. However, in comparison with conventional catalyst, SACs might offer higher atomic efficiency of metal and fully expose of every single atom for catalytic reactions [99]. There are various methods to produce SA catalyst: *e.g.*, vapor deposition, atomic layer deposition (ALD) [100,101], co-precipitation [102], wet-chemical synthesis such as impregnation and photo deposition [103], use of metal–organic frameworks (MOFs) [104–107]. However, due to the increased reactivity and their high surface energy, these structures are chemically unstable and they have great tendency for aggregation, thereby leading to formation of either nanocluster or nanoparticles [108,109]. As can be seen in Figure 2.8b, without any metal–metal bond, uniformly or non-uniformly distributed isolated single metal atoms, where immobilized onto heterogeneous supports called SACs. Although, SAC and atomically dispersed catalyst (ADC) show totally dispersion because all atoms are exposed, ADC contains an inhomogeneous distribution of different structure and sizes of clusters that are non-isolated [110].

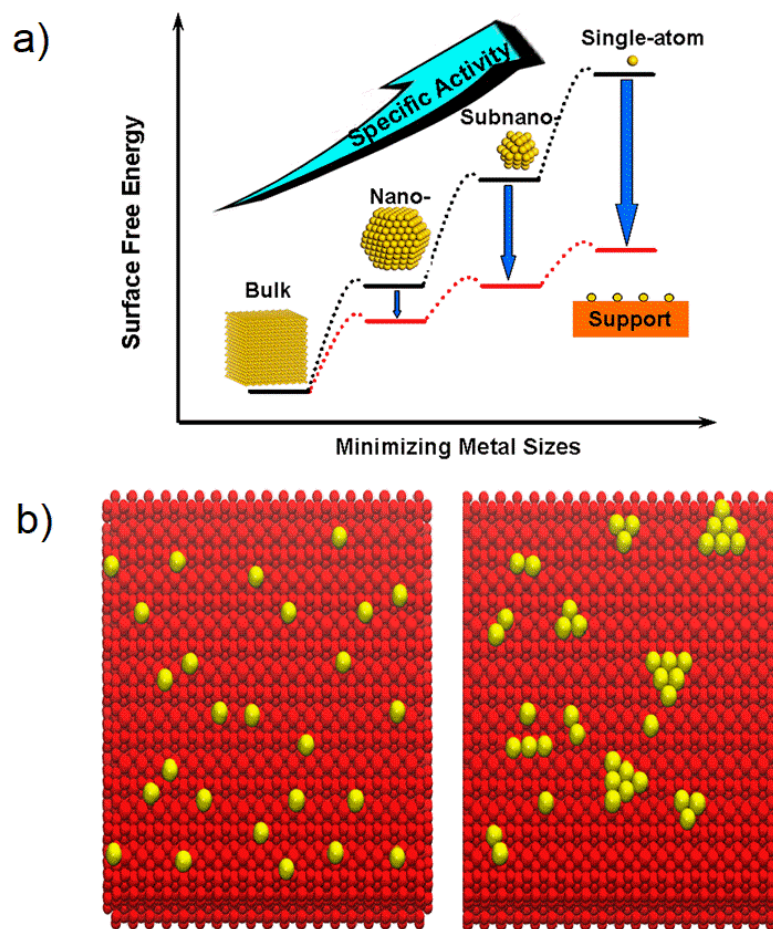


Figure 2.8 Schematic illustration of a) the surface free energy changes and its specific activity per metal atom [98] and, b) difference between SAC (left) and ADC (right). [110].

### 2.3.2.1.2 Plasmonic-enhanced performance

Based on aforementioned discussion, the surface decoration of TiO<sub>2</sub> with noble metals (*i.e.*, Au, Pt) as a co-catalyst has been extensively investigated in photocatalysis and photoelectrochemical water splitting. On the other hand, noble metal nanoparticles (NPs) can be employed as plasmonic NPs, enabling an effective light absorption in visible and near infrared (IR) region due to localized surface plasmon resonance (LSPR) [111–113]. The resonance of plasmonic NPs as a function of size, shape, dielectric features of material and distance between adjacent NPs can efficiently absorb the UV, Vis, and even near IR light photons in order to catalyze the chemical reactions [114]. After absorption of light by metal NPs and excitation of LSPR, the non-radiative decay

of plasmons gives rise to the hot-electrons. Consequently, this electron can be migrated from NPs to the conduction band of semiconductor if its energy is higher than Schottky barrier (Figure 2.9 a-d) [115,116].

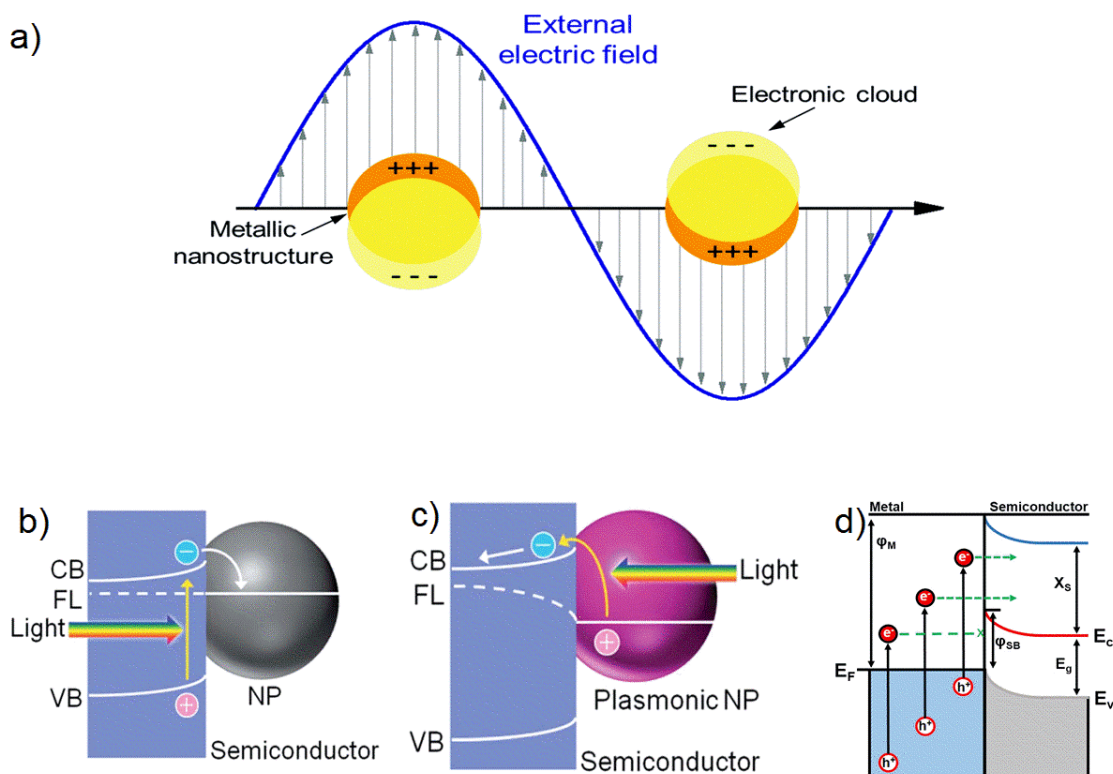


Figure 2.9 Schematic illustration of a) LSPR of metal NPs, b) Co-catalyst effect of NPs c) the plasmon-induced charge separation of plasmonic NPs and d) hot electrons with sufficient energies can pass the Schottky barrier and reach to the semiconductor conduction band [115,116].

### 2.3.3 Black TiO<sub>2</sub>

In order to increase the optical absorption of TiO<sub>2</sub> through metal or non-metal doping, many efforts have been dedicated to study colourful TiO<sub>2</sub> from the last decade. All these investigations tend to bring about the extension of absorption into the visible-light region for enhancing its photocatalytic activity. For instance, a series of metal ions and non-metal elements have been utilized to substitute the Ti<sup>4+</sup> and O<sub>2</sub> ions in the TiO<sub>2</sub> lattice, respectively [117–120]. The black TiO<sub>2</sub> via hydrogenation method in a high pressure of 20 bar at 200°C has been introduced as an efficient approach in shifting the bandgap of TiO<sub>2</sub> to around 1.5 eV (807 nm) with an optical onset around 1.0 eV (~ 1200 nm) by Chen et. all in 2011 (Figure 2.10A) [121]. As shown in Figure 1, the formation of mid-gap state

as results of extended disorder layer, presenting the concept of fabricated black TiO<sub>2</sub> nanomaterials (Figure 2.10B) along with the pictures (Figure 2.10C). The HRTEM images of white and black TiO<sub>2</sub> nanoparticles shown in Figure 2.10D, E.

Afterwards, black TiO<sub>2</sub> nanomaterials received has worldwide research interest due to its lattice disorder-induced reduction in the bandgap of TiO<sub>2</sub>, which causes efficient light absorption. Indeed, it is reported that either heating TiO<sub>2</sub> in a reducing atmosphere (Ar, H<sub>2</sub> etc.) under vacuum or using electrochemical/chemical reduction treatments leads to a colour change from yellow to black material as well as formation of Ti<sup>3+</sup> or/and oxygen vacancies.

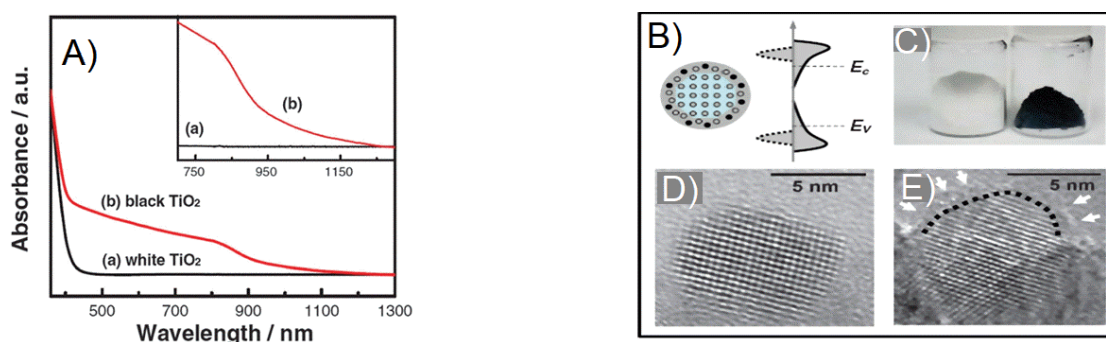


Figure 2.10 A) Optical absorption of spectra of (a) white TiO<sub>2</sub> and (b) black TiO<sub>2</sub>. Inset shows the extended absorption of black TiO<sub>2</sub> nanoparticles, B) Schematic illustration of structure and density of state (DOS) of fabricated black TiO<sub>2</sub>, C) pictures of white and black TiO<sub>2</sub>, HRTEM images of D) white and D) black TiO<sub>2</sub> [121].

Based on above discussion different type of defect are created after reduction of TiO<sub>2</sub>. Generally, defects in semiconductors play important role in mechanical, optical and magnetic properties as well as can affect on carrier concentration and interface reaction. Therefore, defect engineering as a most frequently investigated scenario is vital for activation of catalyst for photocatalytic reactions [122,123]. Defects can be categorized into four main divisions based on their dimensionality of the defect (Figure 2.11). Firstly, zero dimensional (0D) defects or point defects are associated to the single or few atomic positions. For instance, Ti<sup>3+</sup>, oxygen vacancy, Ti interstitial, Ti vacancy (can be seen as results of prolonged oxidation of TiO<sub>2</sub>) and substantial impurities such as non-metal and

metal dopants belong to this type of the defect. The formed defect can be accommodated at different level of semiconductor such as surface which is first atomic layer of semiconductor. The second level could be subsurface from atomic surface up to few nanometre in depth, and finally bulk of semiconductor may encounter defect as well [124]. It is reported that the incorporation of metal ions into TiO<sub>2</sub> crystal lattice can form additional 3d state below the CB of TiO<sub>2</sub> [125]. Similarity, oxygen vacancy with the mutual formation of Ti<sup>3+</sup> yields electronic states (0.8–1.2 eV) below the CB. In contrast, non-metal dopant such as C, N, S presents the electronic state above a defective TiO<sub>2</sub> [125,126]. Line defects (1D defect) or dislocations stem from plastic deformation of crystal lattice which can move if the atoms from one of the surrounding planes break their bonds and rebond with the atoms at the terminating edge. Planar defects (2D defects) such as grain boundary is a kind of defect that separates regions of different crystalline orientation within a polycrystalline solid. Interphases (two-phase boundaries) like creation of rutile/anatase nanojunctions in TiO<sub>2</sub> nanoparticles also can be defined as a 2D defects. However, this kind of defect for TiO<sub>2</sub> photocatalyst determines efficient charge carrier transport and separation as well as surface reactivity [127,128]. Volume defects (3D defect) are very similar to the point defects consist of voids, crack, existing either bulk or surface of material [129,130].

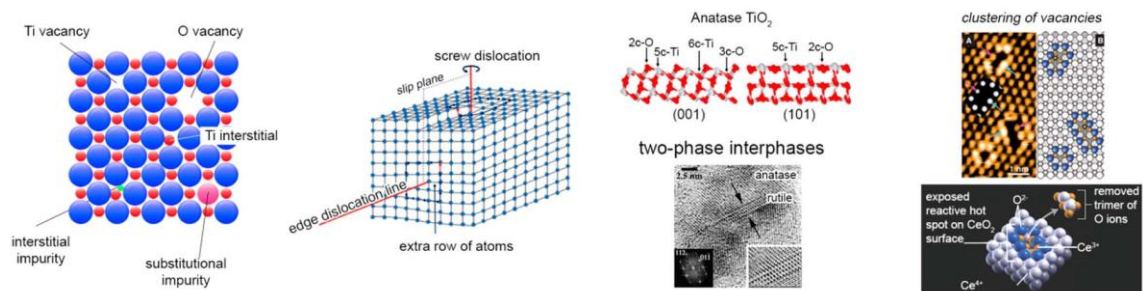


Figure 2.11 Schematic illustration of various defects with local atomic structures in the photocatalysts [124].

Research on black TiO<sub>2</sub> has attracted attention of scientists working in different fields, ranging from H<sub>2</sub> production through the water splitting to removal of either pollution or contaminants from environmental media. As far, the black TiO<sub>2</sub> is investigated in many research works, various methods have been uncovered for the synthesis of it, to reveal the enhanced performance of photocatalyst in comparison with pristine one. It is believed that, the photoactivity of the composite structure of black TiO<sub>2</sub> with other components will be enhanced due to the synergy between the beneficial effects provided by all the materials. In this section, some of these approaches will be briefly reviewed.

### *2.3.3.1 Reduction treatment under high temperature*

H<sub>2</sub> thermal treatment of TiO<sub>2</sub> is the straightforward and facile technique, which can reduce TiO<sub>2</sub> into other chemical species. By doing this, the chemical or physical properties is changed for fabricated black TiO<sub>2</sub> accordingly. Oxygen vacancy/Ti<sup>3+</sup> is formed in high temperature treatment under reductive atmosphere such as H<sub>2</sub> treatment in high/low pressure, H<sub>2</sub>/Ar, H<sub>2</sub>/N<sub>2</sub> and Ar treatment. Schmuki et al. [131] reported that the hydrogenation treatment of anodic TiO<sub>2</sub> nanotube in a high pressure H<sub>2</sub> at high temperature (20 bar, 500°C for 1h) can turn the colour of anatase TiO<sub>2</sub> into light blue. In addition, hydrogenation conditions played a decisive role in its optical properties, showing a high H<sub>2</sub> evolution rate in photocatalytic experiments compared to the classic reduction treatment such as reduction in H<sub>2</sub>/Ar.

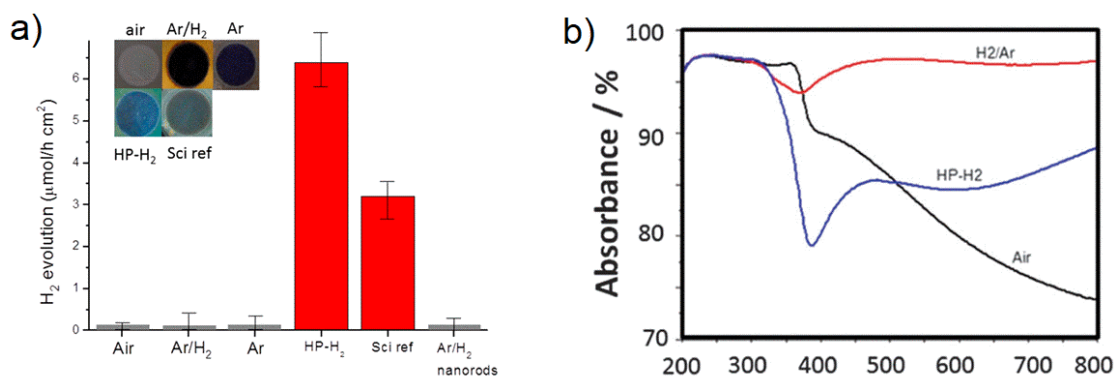


Figure 2.12 a) Images and hydrogen evolution of TiO<sub>2</sub> nanoparticles treated under different conditions and b) UV-DRS measurement of TiO<sub>2</sub> nanotubes annealed in various reductive atmospheres [131].

### 2.3.3.2 Electrochemical reduction

Totally, in this method for the self-doping of Ti<sup>3+</sup> into TiO<sub>2</sub>, a three-electrode configuration is utilized by applying negative potential. For the electrochemical reduction, TiO<sub>2</sub> samples which can be either as a anodized TiO<sub>2</sub> nanotubes or thin film TiO<sub>2</sub> nanoparticles on the FTO is used as the working electrode; Pt and saturated Ag/AgCl (3 M KCl) as counter and reference electrodes, respectively [132–136]. Li et al. [136] reported the synthesis of black TiO<sub>2</sub> nanotubes using anodization method followed by electrochemical reduction as presented in Figure 2.13. After synthesizing TiO<sub>2</sub> nanotubes in an ethylene glycol, 0.2 M HF and 0.12 M H<sub>2</sub>O<sub>2</sub> solution as an electrolyte under 60 V for 12 h, they were annealed at 450°C for 4 h. The fabricated TiO<sub>2</sub> undergoes electrochemical reduction in an ethylene glycol solution containing 0.27 wt% NH<sub>4</sub>F under 40 V for 200 s. Consequently, black TiO<sub>2</sub> nanotubes with lower resistivity and narrower bandgap than pristine ones were synthesized.

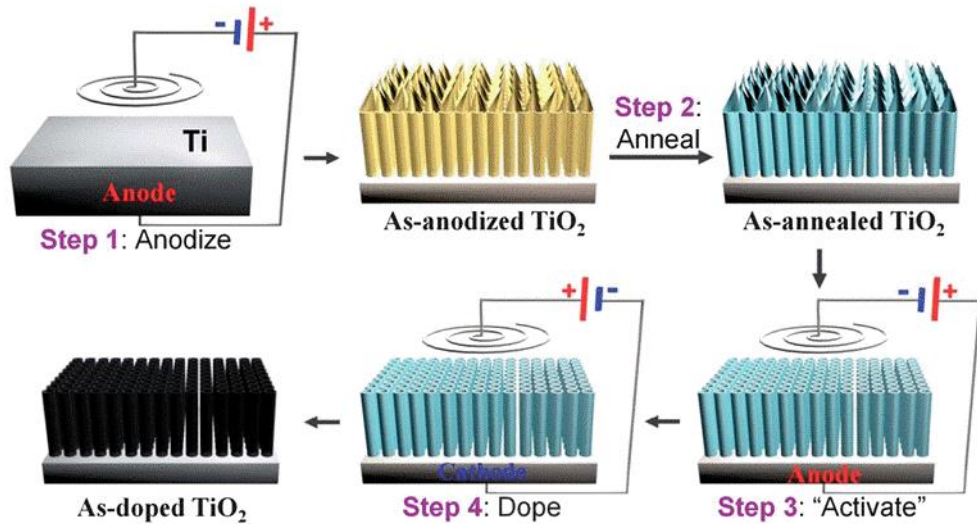


Figure 2.13 Schematics of the synthesizing black TiO<sub>2</sub> nanotube via electrochemical reduction method [136].

### 2.3.3.3 Chemical reduction

The chemical reduction technique include the reduction of TiO<sub>2</sub> with metals such as aluminium (Al) [137,138], zinc (Zn) [139], and in solution with NaBH<sub>4</sub> [140] can effectively change the colour of TiO<sub>2</sub> into black. For instance, grey rutile TiO<sub>2</sub> nanoparticles through the zinc reduction has been synthesized by Zhao et al. [139]. Presence of Zn powder in the solution hamper the fully oxidation of Ti<sup>3+</sup> in the reaction thereby changing the colour of synthesized TiO<sub>2</sub>. Based on the amount of Zn inside the solution the colour change from grey to black, which leads to band gap narrowing and its photocatalytic activity in visible light region (Figure 2.14).

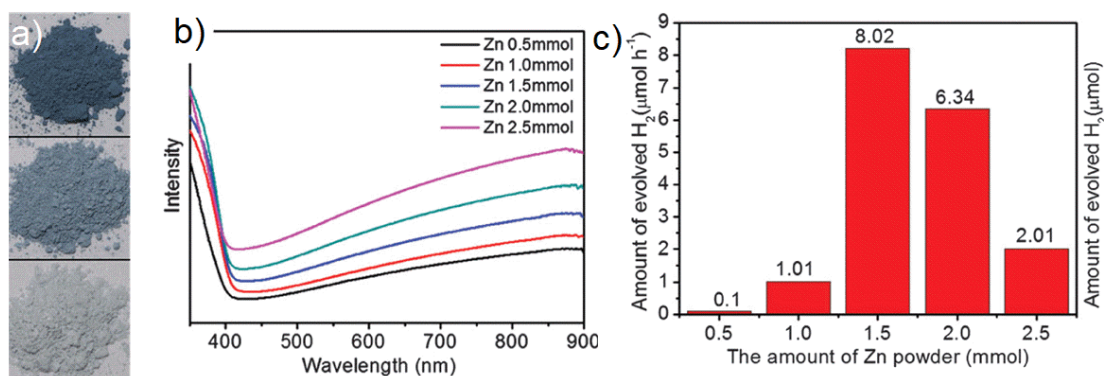


Figure 2.14 a) Images of reduced TiO<sub>2</sub> nanoparticles treated with 2.5 (top), 1.5 (middle) and 0.5 (bottom) mmol of Zn powder, b) UV-visible absorbance spectra and c) H<sub>2</sub> evolution measurement of reduced TiO<sub>2</sub> nanoparticles obtained from different amounts of Zn powder in visible light region [139].

Wang et al. [137] synthesized oxygen-deficient TiO<sub>2-x</sub> in an evacuated two-zone vacuum furnace at 300–500°C utilizing Al as an excellent reductant. For this reason, Al and TiO<sub>2</sub> nanoparticles were separately placed in an evacuated two-zone tube furnace with pressure lower than 0.5 Pa (Figure 2.15a). The Al and TiO<sub>2</sub> samples were heated at 800°C for 6 h and 300–600°C for 20 h, respectively. As shown in Figure 2.15b using Al-reduction route has gained a lot of importance due to could produce in huge quantities (one batch). The synthesized black TiO<sub>2</sub> photocatalyst can absorb more solar light in the visible-light and near-infrared regions (Figure 2.15c).

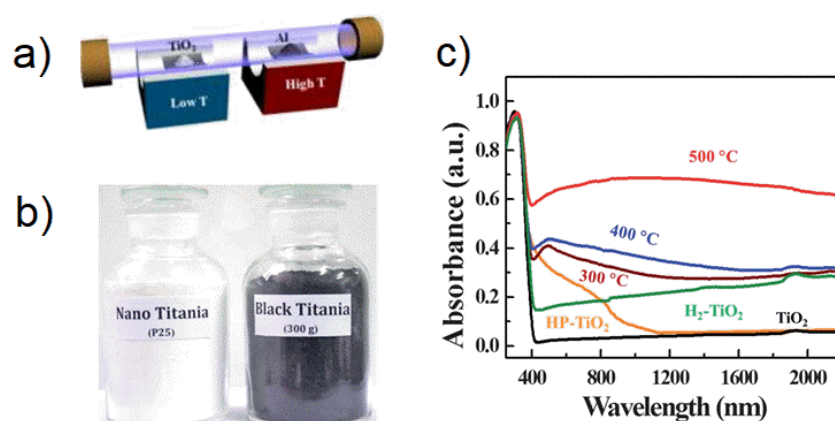


Figure 2.15 a) Schematic illustration reduction of TiO<sub>2</sub> in a two-zone tube furnace, b) images of black and white TiO<sub>2</sub> using Al-reduction method and c) UV-visible absorption spectra of pristine TiO<sub>2</sub>, hydrogenated black TiO<sub>2</sub> with high pressure (HP-TiO<sub>2</sub>) and TiO<sub>2</sub> nanoparticles reduced at different temperatures (300°C, 400°C, 500°C) [137].

2.3.3.4 H<sub>2</sub> plasma

H<sub>2</sub> plasma as highly ionized H<sub>2</sub> gas using an electromagnetic field in a thermal plasma furnace can be employed to produce black TiO<sub>2</sub> nanoparticles [141–143]. The core/shell structure of black TiO<sub>2</sub> nanoparticles using H<sub>2</sub> plasma for 4–8 h at 500°C has reported by Wang et al. [142]. The hydrogenated black TiO<sub>2</sub> nanoparticles enhanced solar light absorption in the visible and near infrared light (Figure 2.16).

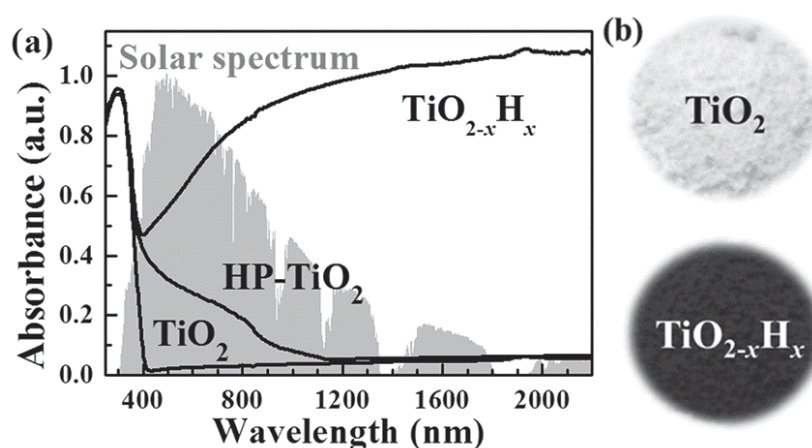


Figure 2.16 a) UV-visible-IR absorption spectra of pristine and plasma-reduced and high presurer hydrogenated TiO<sub>2</sub> and b) images of pristine and plasma-reduced TiO<sub>2</sub> [142].

## 2.3.3.5 Ion bombardment

Oxidation state of surface cations could be lowered during the ion bombardment in an inert atmosphere such as argon (Ar) by partially removing oxygen. The ion-bombarded surface of TiO<sub>2</sub> has been investigated in some literatures which the fractions of the reduced state (Ti<sup>2+</sup> and Ti<sup>3+</sup>) in TiO<sub>2</sub> can be formed. Schmuki et al. [144] reported that Ar ion bombardment of TiO<sub>2</sub> for modification of synthesized TiO<sub>2</sub> nanotubes. Sub-surface lattice defects in the TiO<sub>2</sub> nanotubes can be observed through the X-ray photoelectron spectroscopy and show higher photocatalytic H<sub>2</sub> evolution rate of reduced sample compared to the pristine one (Figure 2.17).

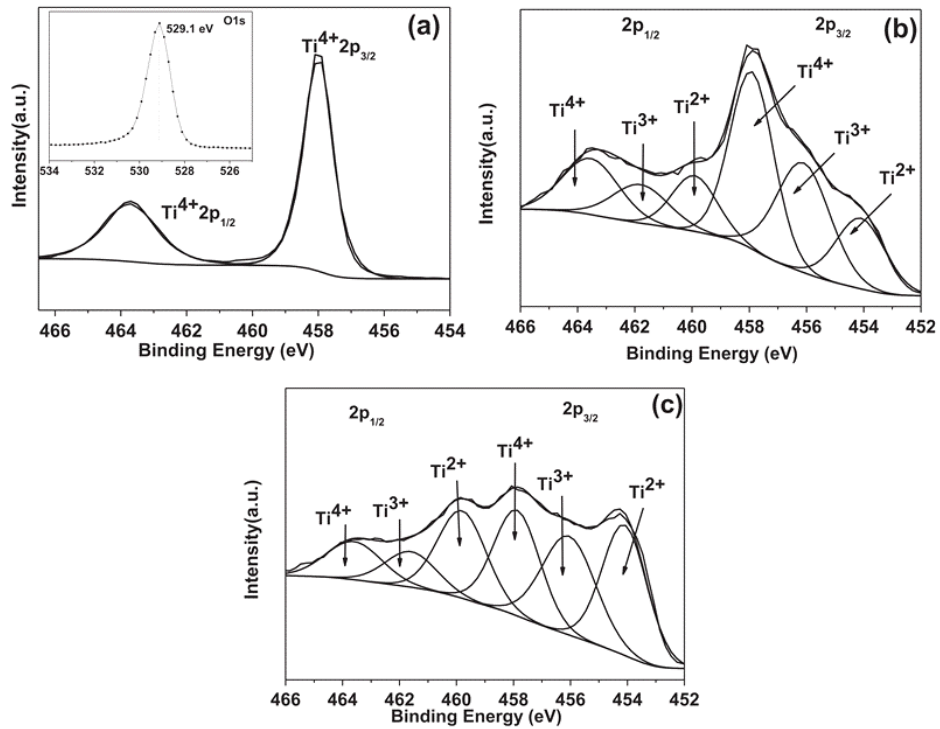


Figure 2.17 HRXPS of Ti2p peaks pristine TiO<sub>2</sub> (a) and after 50 min (b), 5 h (c) Ion bombardment [144].

### 2.3.3.6 Sonication

It is reported that ultrasonication can be used in the aqueous media at ambient temperature to make black TiO<sub>2</sub> via a gentle reduction method [145,146]. The other approaches such as hydrogenation at high temperature has brought some disadvantages including phase transformation, sintering and introducing impurities owing to the harsh reaction conditions. Generally, waves of ultrasound could produce acoustic cavitation along with simultaneous high temperature (> 5000°C) and high pressure (> 100 MPa). In addition, explosion of cavitation bubbles occurs due to prompt cooling rate (> 10<sup>10</sup>°C/s) in a spot at the interface of solid-solution [146–148]. Osorio et. al [145] in 2012, shown changes in the optical, morphological, and surface of commercial P25 using ultrasonic irradiation. They confirmed the presence oxygen vacancy defects in the structure of P25 TiO<sub>2</sub>, which is responsible for visible-light absorption by utilizing electron paramagnetic resonance (EPR) measurements. They suggested that oxygen vacancy defects formation can be attributed to the high-speed inter-particle collisions as well as shock waves

generated by sonication. Later, Fan and co-workers [149] in 2015, reported that beside traditional methods for reduction of TiO<sub>2</sub>, ultrasonic technique could be utilized to enhance the photocatalytic activity of TiO<sub>2</sub>. Based on their investigation, ultrasonication introduce hydroxyls injection into TiO<sub>2</sub> crystal lattice, obtaining disrobed TiO<sub>2</sub> nanoparticle with various degrees of blackness depends on the time of ultrasonication [149]. As a result, the changes in the structure and density of state (DOS) of sonicated TiO<sub>2</sub> nanoparticle could regulate the energy band structure of TiO<sub>2</sub> and increasing in visible light absorption for its better photocatalytic activity. In another study, Whang and his group [146] has employed ultrasonication technique to boost solar-driven photocatalytic activity by 2.33 times in comparison with the pristine P25 by introduction of defects into the TiO<sub>2</sub> crystal lattice and band gap narrowing (Figure 2.18).

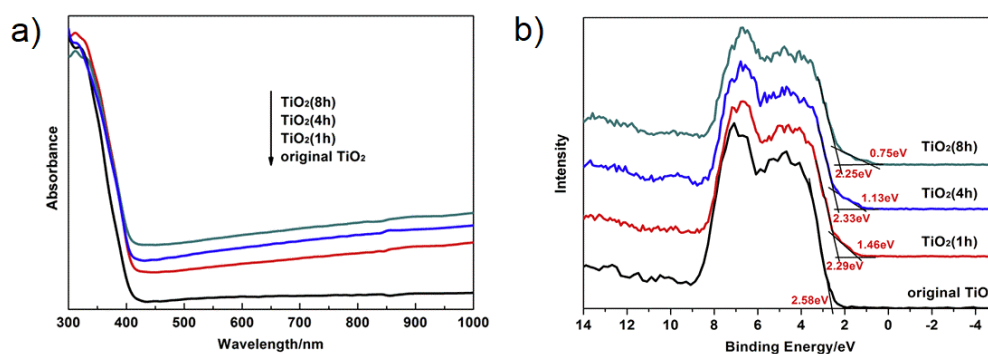


Figure 2.18 UV-vis absorbance spectra and b) valence band XPS spectra of pristine and sonicated TiO<sub>2</sub> nanoparticles for different h [146].

## 2.4 The aim of this work

As previously discussed, TiO<sub>2</sub> has found extensive utility in photocatalysis due to its unique properties. However, the rapid recombination rate of photogenerated electron-hole pairs limits the potential of pure TiO<sub>2</sub> in significant hydrogen (H<sub>2</sub>) production via photocatalysis. This observation has led to the exploration of decorating TiO<sub>2</sub> with noble metals and carbonaceous nanomaterials, capable of acting as electron transfer mediators, thereby considerably enhancing H<sub>2</sub> production. Consequently, the objective of this doctoral thesis was to identify optimized conditions that would elevate the photocatalytic

and photoelectrochemical performance of TiO<sub>2</sub> nanostructures. To achieve this, the initial step involved the synthesis of both compact and discrete one-dimensional (1D) TiO<sub>2</sub> nanotubes. These structures offer the advantages associated with nanoparticles, while simultaneously possessing unique properties, such as a direct pathway for expedited electron transportation. Subsequently, efforts were directed towards creating a discrete TiO<sub>2</sub> nanotubes/platinized cyanographene heterojunction to examine its potential for enhancing photoelectrochemical water splitting performance.

Furthermore, attention was devoted to investigating the controlled single atom decoration of noble metals, such as platinum (Pt), onto TiO<sub>2</sub> nanotubes for photocatalytic H<sub>2</sub> production. Given the scarcity and expense of noble metals, this approach presents a practical avenue for utilizing such precious materials, while concurrently amplifying the catalyst's photolytic activity.



## Chapter 3: Materials and method

### 3.1 Fabrication of different morphology of TiO<sub>2</sub> nanotubes

#### 3.1.1 Compact TiO<sub>2</sub> nanotubes (TNTs)

Ti foils (0.25 mm, 99.5% purity) were purchased from Sigma-Aldrich and were used in all experiment. As shown in Figure 3.1, the electrochemical anodization experiments were carried out in a two-electrode configuration, with a Ti foil as the working electrode and a Pt as a counter electrode, respectively. The anodization cell was made of polyvinyl chloride (PVC) or Teflon. The Pt electrode was placed on the top, parallel and approximately 2 cm away from the working electrode. The copper plate was also pressed against an elastic O-ring due to complete circuit in our experiment by ensuring the backside contact of the Ti foil. Prior to anodization, the Ti foils were cut on pieces with area  $1.5 \times 1.5 \text{ cm}^2$  and were cleaned ultrasonically in acetone, ethanol and deionized water (DI) in sequence for 15 min, and then dried in nitrogen (N<sub>2</sub>) stream. After drying, the reaction was driven by a DC power source at room temperature for 30 min by using a constant voltage of 70 V and an electrolyte solution containing of 94.65 wt% of ethylene glycol (99.5%, Sigma-Aldrich), 0.68 wt% HF (38-40%, Lachner) and 4.67 wt% DI water (Sigma-Aldrich). After the anodization, the synthesized TNTs were washed in DI water and then were calcined at 450°C in air for 2 h (heating and cooling rate of 2°C/min).

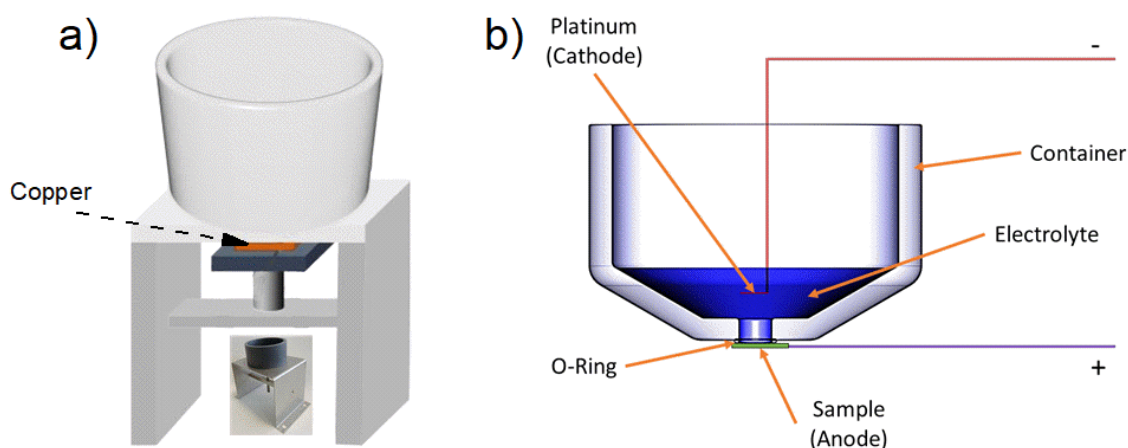


Figure 3.1 Schematic illustration of the a) the whole experimental set-up with an its real image (inset) and b) cross-section of the O-ring, Ti foil as a working electrode (anode) , Pt as counter electrode (cathode).

### 3.1.2 Multi-leg $\text{TiO}_2$ nanotubes (MLTNTs)

MLTNTs were synthesized via electrochemical anodization of Ti foil. This synthesis approach bears quite to the synthesis of TNTs. The anodization system consists of Ti foils served as a working electrode and Pt sheet as the counter electrode, respectively, keeping the distance of 2 cm. The anodization was carried out at  $35^\circ\text{C}$  temperature for 2-6 h. the voltage was applied by using a constant voltage of 30-120 V. Ti foils were anodized in electrolyte consisting of 0.6 wt.% ammonium bi-fluoride salt ( $\text{NH}_4\text{F}\cdot\text{HF}$ ), 96 ml diethylene glycol (DEG, Sigma-Aldrich) and 4 ml deionized (DI) water.

## 3.2 Modification of $\text{TiO}_2$ nanostructures

### 3.2.1 Thermal treatment

The as-synthesized TNTs and MLTNTs are amorphous in structure. Therefore, thermal treatment in the air was performed due to crystallization in  $\text{TiO}_2$  materials. TNTs and MLTNTs were calcined (RTA, Jipelec JetFirst100) at  $450^\circ\text{C}$  in air for 2 h with heating and cooling rate of  $2^\circ\text{C}/\text{min}$ .

H<sub>2</sub> annealing of samples were carried out in a quartz chamber in a tubular furnace. The heating and cooling rate of the tubular furnace was 10°C min<sup>-1</sup> in N<sub>2</sub> flow rate 10 mL min<sup>-1</sup> as well as 1 h dwell in H<sub>2</sub> flow rate 10 mL min<sup>-1</sup> at predefined temperature. Prior to the heat treatment, in order to eliminate the residual contamination such as carbon inside the furnace, the tube furnace was cleaned up increasing the temperature up to 1000°C in the air.

### 3.2.2 Preparation of the cyanographene and platinized cyanographene composite

The cyanographene (G-CN) and platinized cyanographene (G-Pt-CN) were coated over the MLTNTs via the electrodeposition method. Experiment was performed at room temperature using a standard two-electrode, in which MLTNTs on the Ti foil and the Pt foil served as the working and the counter electrodes, respectively. The deposition was conducted under constant applied voltage in the 100 V for 1 min. The resulting TiO<sub>2</sub> composite were then rinsed with DI water and ethanol, respectively. The samples were then dried with nitrogen stream (Figure 3.2). For the sake of simplicity, pristine TiO<sub>2</sub> nanotubes, G-CN-TiO<sub>2</sub> nanotubes and platinized cyanographene TiO<sub>2</sub> nanotubes are hereafter referred to as P-NTs, G-NTs, and G-Pt NTs, respectively.

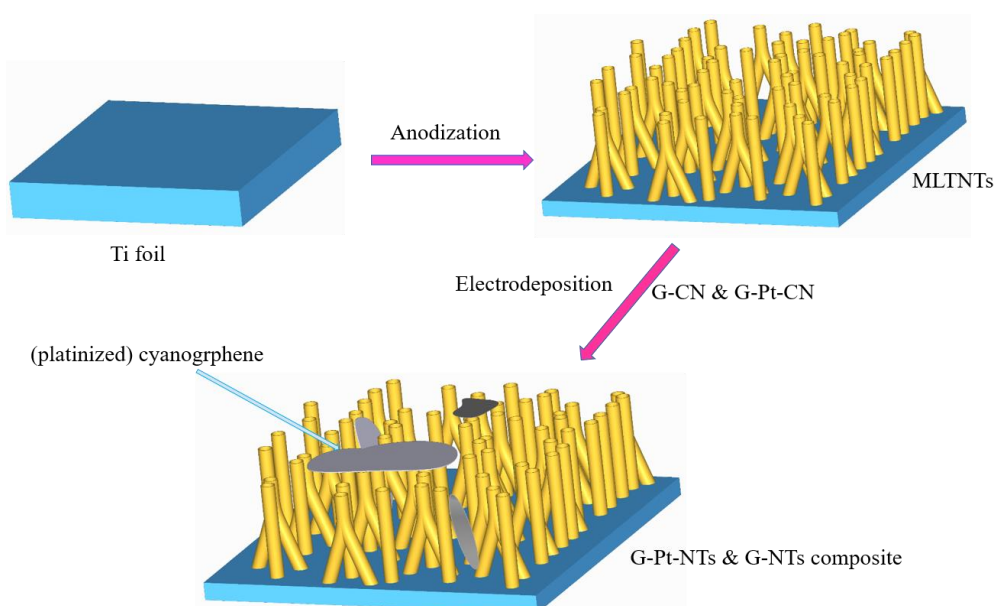


Figure 3.2 Schematic illustration of the preparation of G-Pt NTs and G-NTs composite.

### 3.2.3 Preparation of Pt-SA

Reduced TNTs were fabricated through sonicating the pristine TNTs in the beaker filled with 100 ml DI water and in Ar atmosphere which was kept 2 cm away from the sonication at different sonication time (30, 40, 50, 60, 70 and 80 min). The aqueous solution of the deposition bath contained 100  $\mu\text{M}$  of chloroplatinic acid ( $\text{H}_2\text{PtCl}_6$ , Safina Ltd.) in volume of 50 ml of DI water. Before soaking the sample in the chloroplatinic acid, the solution was purged 30 min in Ar gas to remove oxygen. Immediately after reduction using the tip sonication, in order to decorate Pt-SA, without any further purification, reduced TNTs were immersed in solution for the different time ranging from 1 to 60 min (schematic 1). For the sake of simplicity, pristine  $\text{TiO}_2$  nanotubes arrays, reduced  $\text{TiO}_2$  nanotubes and Pt-decorated  $\text{TiO}_2$  nanotubes are hereafter referred to as P-NT, US $x$ -NT ( $x$ :30, 40, 50, 60, 70 and 80) and US50/Pt-NT $y$  ( $y$ :1, 10, 15, 30 and 60), respectively.

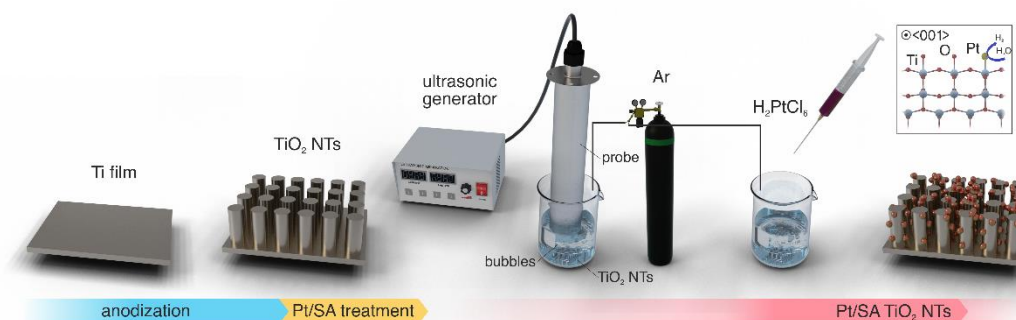


Figure 3.3 Schematic illustration of Pt-SA catalyst process.

## 3.3 Material characterization

### 3.3.1 Scanning electron microscopy (SEM)

The first SEM image from the surface of solid was obtained by Max Knoll in 1930s. Then, Manfred von Ardenne has manufactured his electron microscope for explaining the

principle of the SEM machine such as electron probe, detector position and so on [150]. The SEM microscope consists of an electron gun, electron sources (the cold field and thermionic source), lenses vacuum system, software and electronics. In SEM analysis, a high-energy electron (0.2–30 keV) beam is focused on the surface of a specimen. The interaction between the sample and the electron primary electrons results in either elastic or inelastic scattering, producing back-scattered electrons (BSEs) and secondary electrons (SEs), respectively. Qualitative information regarding the specimen elemental composition can be obtained from the BSEs. SEs are produced by inelastic scattering if the energy transferred is adequate. These electrons require higher energy than the material work function to transfer the detector, achieving topographic contrast (Figure 3.4) [151]. The morphology of fabricated samples were characterized using a scanning electron microscopy (SEM, Hitachi SU 6600).

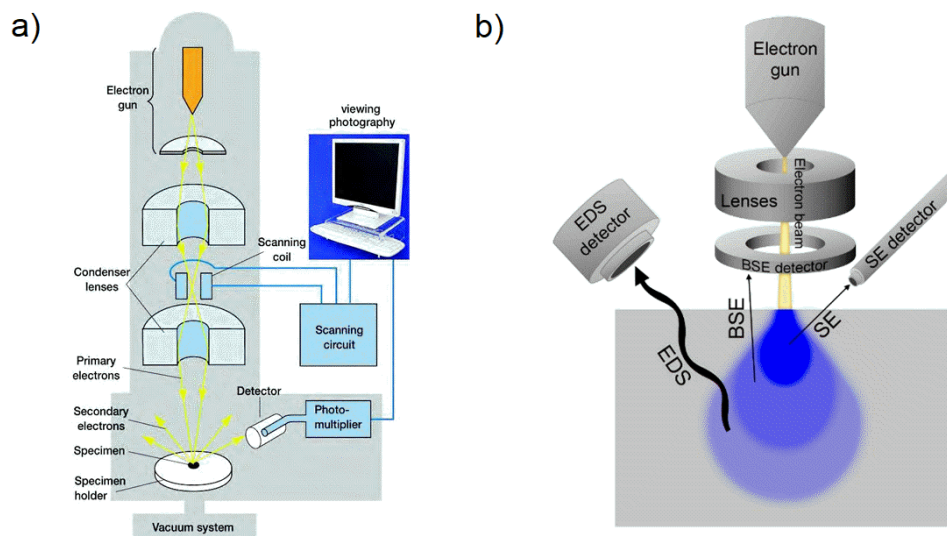


Figure 3.4 Schematic illustration of a) SEM microscope and b) the interaction of electron beam with sample [151].

### 3.3.2 Energy-dispersive X-ray spectroscopy (EDS)

EDS is a powerful technique, which can be utilized to analyze the elemental composition of fabricated samples. It is based on the interaction of some source of X-ray excitation and a sample to eject core electrons from an atom. By removing these electrons

from the inner shell of atom, leave behind a hole that a higher energy electron from the outer shell can fill in, and it can release energy (X-ray). This energy can be attributed to the energy difference of the outer and inner shell of an electron. However, during this relaxation phenomenon, the released energy is unique to each element. The main parts of EDS are an emitter, a collector, and an analyzer, which can be additionally equipped on an electron microscope such as TEM and SEM. In this work, an EDS in the chamber of Transmission electron microscopy was employed to determine the chemical composition of fabricated samples.

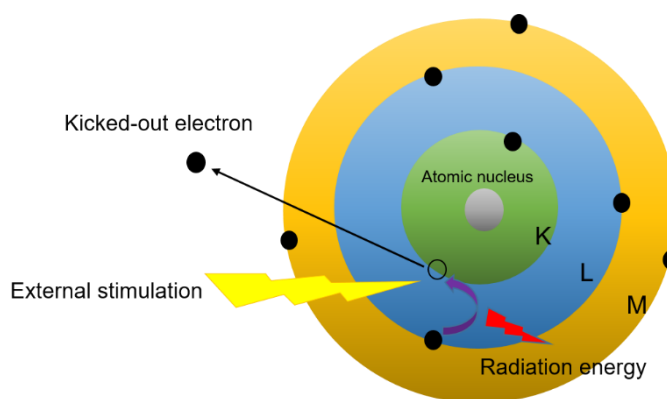


Figure 3.5 Schematic illustration of X-ray generation through the incident electron beam.

### 3.3.3 Transmission electron microscopy (TEM)

TEM is another useful technique of characterization of nanomaterials that uses an electron beam to image a nanoparticle sample, while having much higher resolution than SEM. TEM is the preferred method to directly measure size of nanoparticle, size distribution, grain size, and morphology of samples. Electron gun at the top of the microscope emits electrons that travel through a vacuum in the column of the microscope and are accelerated in high velocity. Due to control the intensity and convergence angle of the electron beam, several electromagnetic lenses are used to focus the electrons into a very thin beam. The electrons passing through the sample and the objective lens. The thickness of specimen should be less than 200 nm thick to allow transmission of incident electron beam (Figure 3.6) [152]. Our synthesized samples were investigate using a TEM

JEOL 2010 with LaB6 type emission gun, operating at 160 kV and high-resolution transmission electron microscopy (HRTEM) images and elemental maps were acquired with a FEI TITAN G2 60-300.

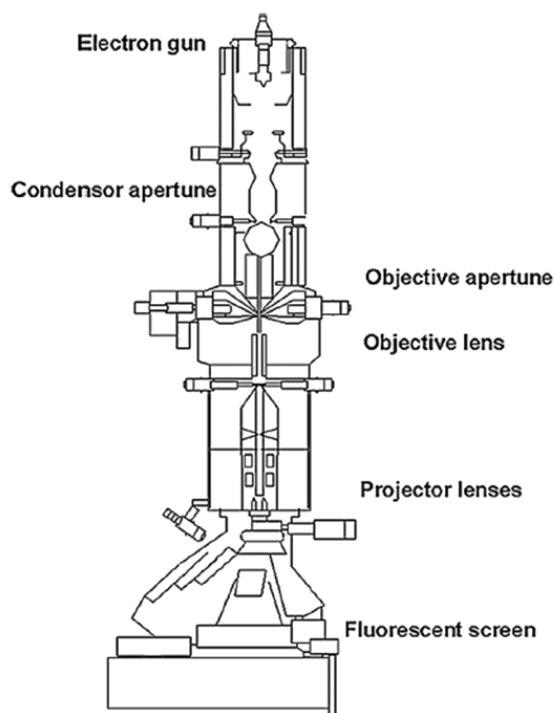


Figure 3.6 Different component of TEM set-up [152].

### 3.3.4 X-ray photoelectron spectroscopy (XPS)

XPS known as electron spectroscopy is quantitative spectroscopic technique for analyzing a material's surface chemistry. XPS analysis can be used for detection of all elements through the detection of the binding energies of the photoelectrons, with the exception of H<sub>2</sub> and helium (He). XPS analysis is a non-destructive and informative technique, which can be applied to any metal alloys, semiconductors, polymers, and catalysts. The principle of the XPS technique is the photoemission of electrons ejected from both core and valence levels of surface atoms into the vacuum when the atom absorbs a monochromatic beam of X-ray upon a solid surface having sufficient energy. However, core level of atoms (without participation in chemical bonding) is defined as the inner shells, while the valence level of atoms (partially filled outer shells) consist of

electrons that more weakly bound. The energy beam of incident aluminium (1486.6 eV) or magnesium (1253.6 eV) X-rays is known and by applying the principle of energy conservation, the binding energy ( $E_B$ ) of each of the emitted photoelectrons is estimated based on the equation below:

$$E_B = h\nu - (E_{kIN} + \phi) \quad (3.1)$$

where  $E_B$  is the binding energy of the electron,  $h\nu$  is the energy of the X-ray being used,  $E_{kIN}$  is the kinetic energy of the emitted electron, and  $\phi$  is the work function of the spectroscope. However, it is worthy to mentioned that XPS can only detect those emitted electrons reach to the vacuum, originating from less than top 10 nm of material (Figure 3.7) [153]. In our work, XPS was obtained by a PHI VersaProbe II (Physical Electronics) spectrometer using an Al  $K\alpha$  source (15 kV, 50 W) at room temperature (23°C), under a partial vacuum ( $1.4 \times 10^{-7}$  Pa). All of the achieved data were analyzed using the Multipack (Ulvac-PHI, Inc.) software package.

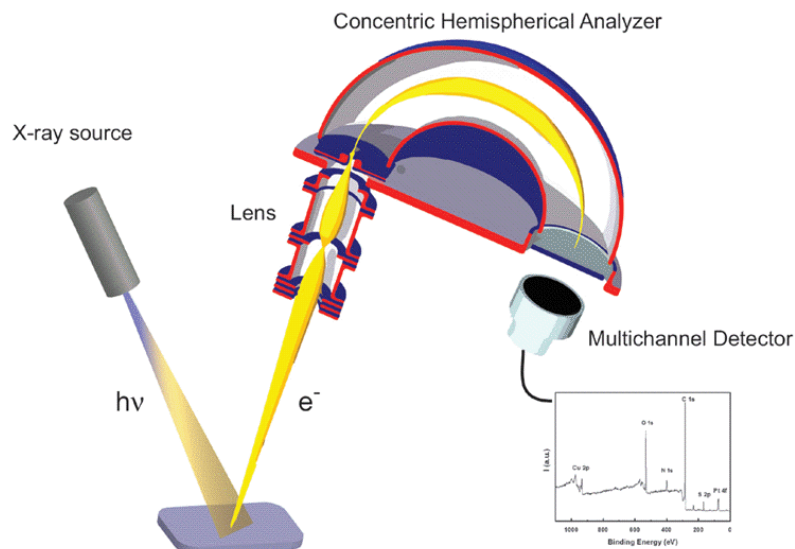


Figure 3.7 Schematic illustration of XPS instrument [153].

### 3.3.5 X-ray diffraction pattern (XRD)

XRD is one of the powerful non-destructive technique employed to analyze different phases present in the fabricated sample, crystal structure. The X-ray source is produced through the bombardment of target metal. When an atom is interacted by an incident X-ray, results in an oscillation of surrounded electron with the frequency as same as electron beam. The XRD diffraction of a crystal can be determined by means of Bragg's law as follows [154]:

$$2d\sin\theta = n\lambda \quad (3.2)$$

Where  $\lambda$  is the wavelength of the X-rays,  $d$  is the distance between crystal planes of Miller indices (h,k,l) and  $\theta$  is the incident angle which is the angle between the planes and the incident X-ray beam (Figure 3.8). In our work, X-ray diffractometer studies (XRD, PANalytical) with Co-K $\alpha$  ( $\lambda = 1.54 \text{ \AA}$ ) radiation source were carried out within the range of  $20^\circ \leq 2\theta \leq 70^\circ$  to investigate the crystalline structure of the synthesized samples.

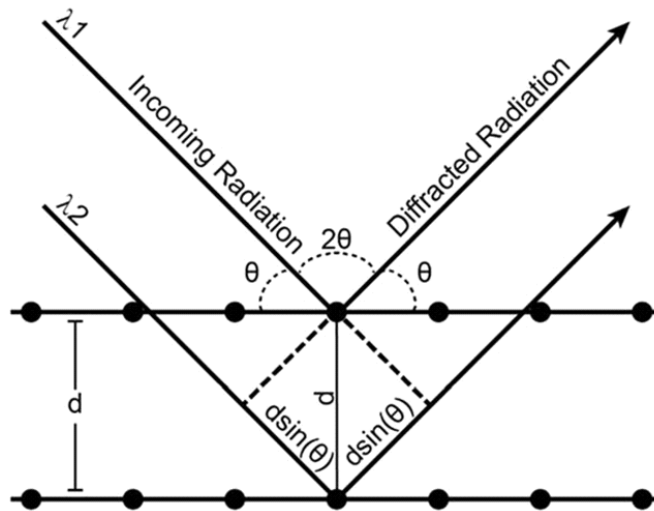


Figure 3.8 representation of Bragg's law [154].

### 3.3.6 Ultraviolet-visible diffuse reflectance spectra (UV-Vis DRS)

UV-Vis DRS as surface analytical and basic spectrophotometric technique is widely used for metals, alloys, and semiconductors. The interaction of light consists of ultraviolet (UV), visible, or infrared (IR) as a probing medium with absorbing surface of material

occurs in the first 10–20 nm. UV-Vis DRS of the synthesized samples were taken using Specord 250 plus (Analytik Jena, Jena, Germany) spectrophotometer. To collect the spectrum and a Spectralon reference sample, an integrating sphere was employed to measure the background. Moreover, diffuse reflectance spectra in combination with the Tauc plot is most widely used to determine the band gap energy ( $E_g$ ) of materials. The idea was originated from Kubelka-Munk theory, which explain the scattering of incident light from the sample when travelling inside of it. The Tauc technique can be defined as a relationship between  $E_g$  and the optical absorption coefficient  $\alpha$ , according to equation 3.3 [155]:

$$\alpha \propto h\nu = A (h\nu - E_g)^n \quad (3.3)$$

Where  $\alpha$  is linear absorption coefficient, A is a proportionality constant,  $h\nu$  is the energy of the incident photon and n is a coefficient that depends on the kind of electronic transition in which is taken equal to the 1/2 for direct band gap materials. The band gap can be obtained by extending the straight line from the straight segment of optical absorption edge of the graph touching the  $h\nu$  axis [155,156].

### 3.3.7 Raman Spectroscopy

Indian physicist C. V. Raman which is known for his work in the field of light scattering, observe Raman scattering in 1928. Raman spectroscopy is a non-destructive analytical technique based on inelastic scattering of monochromatic light (laser source), where scattered light is used to measure the vibrational energy modes in molecules or crystals. As a result of the inelastic scattering, laser photon's energy is shifted up and down and it provides many information about the vibrational, rotational and phonon modes in the system. In this study, Raman spectra were obtained using a DXR Raman spectrometer (Thermo Scientific, Massachusetts, USA). The excitation laser operated at the wavelength of 455 nm with the laser power and exposure time of 0.1 mW cm<sup>-2</sup> and 3s, respectively.

### 3.4 Photoelectrocatalytic and electrochemical characterization

#### 3.4.1 Photoelectrochemistry measurement

The main principles of the PEC have been explained in Chapter 1. Therefore, in this section only some details related to the photoelectrochemical experiments for this thesis will be presented.

The electrochemical impedance spectra (EIS) in a frequency range of 0.1 Hz to 100 KHz was analyzed under the Xe lamp (P=150 W AM 1.5 G) for illumination as the light source in 1 M NaOH solution (pH= 13.6). A standard three-electrode configuration using a Gamry potentiostat (series G300-Warmiste, PA, USA) was used consisting of the 0.28 cm<sup>2</sup> TNTs samples as working electrode, Pt wire as counter electrode, and an Ag/AgCl (3 M KCl) as reference electrode. The incident photon-to-current efficiency (IPCE) can be obtained using the Xe light source combined with a monochromator (Newport Oriel 1/8 Cornerstone). To evaluate photocurrent spectra of the fabricated samples, linear sweep voltammetry (LSV) measurement under stimulated solar spectrum (1 sun, 1.5 AM G and 100 mW cm<sup>-2</sup>) were performed. The applied potential has been converted from V vs. Ag/AgCl to RHE scale using the following formula due to the theoretical thermodynamic cell voltage for water splitting is 1.23 V vs. reversible H<sub>2</sub> electrode (RHE) at 25°C:

$$E_{RHE} = E_{Ag/AgCl}^0 + E_{Ag/AgCl} + 0.059pH \quad (3.4)$$

where the pH is 13.6,  $E_{Ag/AgCl}^0 = 0.197$  V at 298 K, and  $E_{Ag/AgCl}$  is the measured potential vs Ag/AgCl.

#### 3.4.2 Open-circuit hydrogen-evolution

The open-circuit photocatalytic H<sub>2</sub> generation was measured in a quartz tube with 10 mL solution of DI water and methanol (volume ratio 1:1) in front of the solar simulator (1 sun, 1.5 AM G and 100 mW cm<sup>-2</sup>), sealed with a rubber septum. The anodized TiO<sub>2</sub> nanotubes on the Ti foil was directly soaked in the solution. Afterwards, unwanted gasses

and dissolved O<sub>2</sub> inside of solution has been gone through bubbling in Ar gas for 30 min. To ensure about the accuracy of irradiation (1 sun), a calibrated reference solar cell (Newport, California, USA) was used two times, before and after reaction. After a certain time of illumination, 200 μL gas was withdrawn using the syringe through the septum of quartz tube. The photocatalytic H<sub>2</sub> was detected with a gas chromatograph GCMS-QP2010 SE (Shimadzu, Kyoto, Japan ) and a TCD (Thermal conductivity detector).



## Chapter 4: Results and discussions

### 4.1 Fabrication of MLTNTs and influence of process parameters

Highly self-ordered electrochemical anodization of Ti foil can provide a high degree of control over the diameter, length of nanotubes and etc. A new class of TNTs arrays consist of tube-to-tube of spacing TNTs and very well-defined MLTNTs arrays are presented [7]. These discrete MLTNTs can be synthesized under specific anodization conditions and by using either Dimethyl sulfoxide (DMSO) or di-ethylene glycol (DEG), hydrofluoric acid (HF) and DI water as an electrolyte solution. In the next sections, the effects of some key parameters such as applied voltage, electrolyte temperature, anodization time on the morphology of synthesized MLTNTs are briefly presented.

#### 4.1.1 Effect of anodization temperature

One of the most important parameters affecting the fabrication of MLTNTs arrays is the temperature of electrolyte. The formation of MLTNTs morphology has been investigated under controlled temperature of electrolyte in order to keep the uniform distribution of the temperature on the Ti substrate. Figure 4.1 shows that the temperature of electrolyte can highly influence the homogeneity of the spaced MLTNTs. From these SEM images it can be clearly seen that anodization at room temperature (RT) results in formation of more sponge area and less non-uniform nanotubes on Ti substrate. This can be attributed to the local heat generation such as breakdown voltages, causing the high growth rates of local sponge oxide. The uniformity of fabricated MLTNTs is improved

by increasing the temperature to the 35°C. In addition, by the further temperature increase (50°C), some nanotubes were removed from the substrate and the uniformity of nanotubes has changed relatively little.

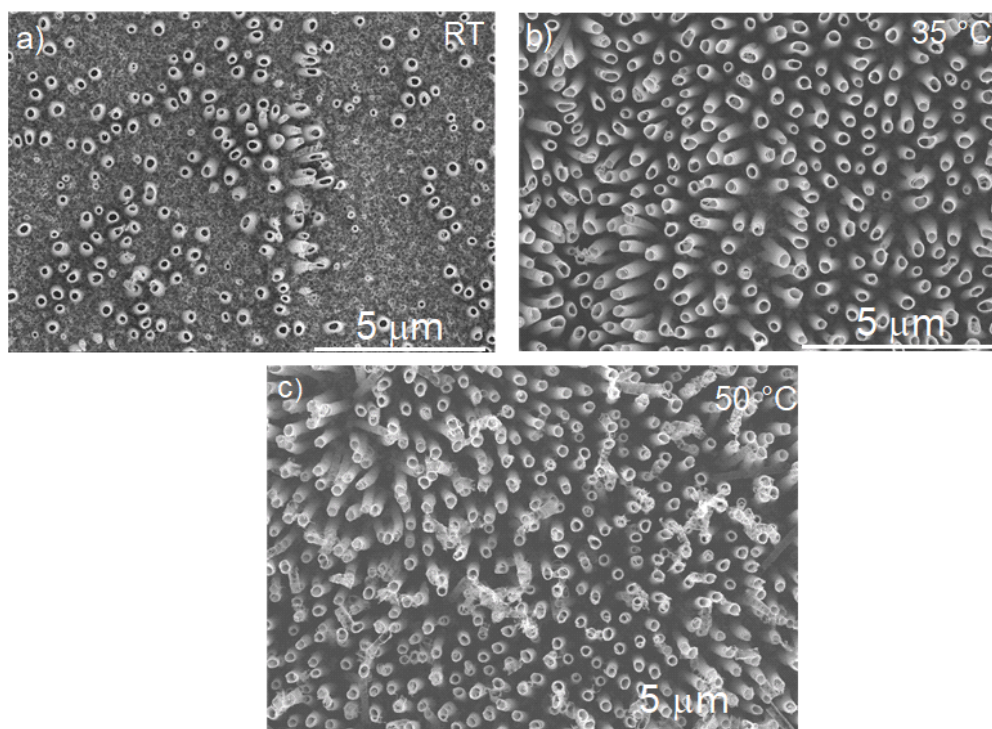


Figure 4.1 SEM images of MLTNTs obtained at a) RT, b) 35°C, and c) 50°C (the anodization was carried out for 2 h by using a constant voltage of 60 V and an electrolyte consisting of 0.6 wt.% ammonium bi-fluoride salt ( $\text{NH}_4\text{F}\cdot\text{HF}$ ), 96 ml diethylene glycol and 4 ml DI water).

#### 4.1.2 Effect of anodization voltage

The morphology of fabricated nanotube arrays highly depends on the applied voltage. Thus, the diameter and length of MLTNTs increased with increasing voltage (Figure 4.2 a-c). At 30 and 40 V, the diameter and the length of nanotube are about 130 nm and 1.3 μm, respectively. However, at 60 V, the diameter and length of synthesized nanotubes increase to approximately 300 nm and 3.3 μm, respectively. Anodization at higher voltages (80 and 100 V) results in an isolated bunch of MLTNTs, which arbitrarily scattered. Therefore, in these two voltages (80 and 100 V), MLTNTs could not be existed on the whole surface of substrate (Figure 4.2 d,e).

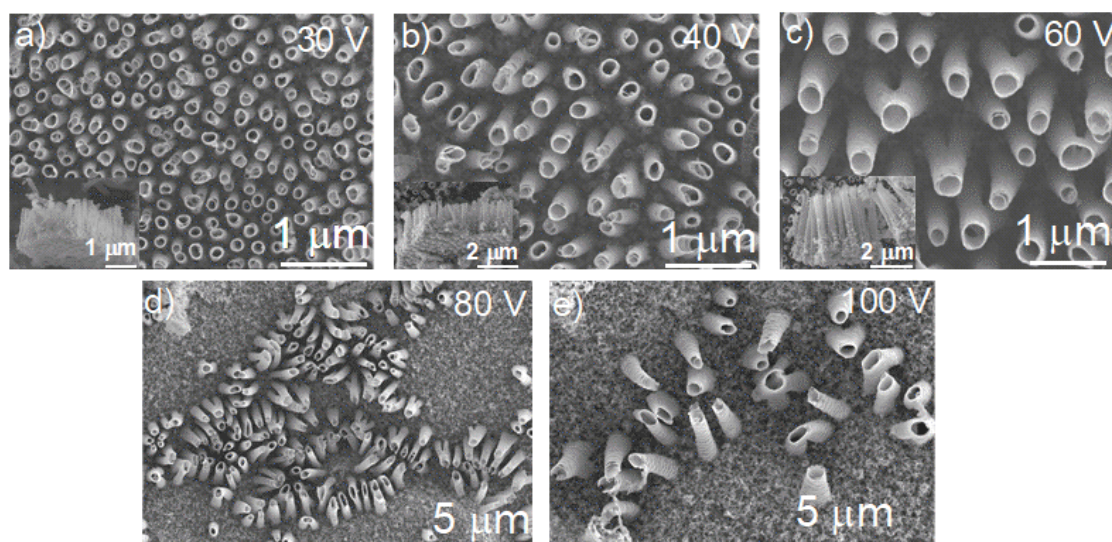


Figure 4.2 Top and cross section SEM images of synthesized MLNTs for various anodization voltage a) 30 V, b) 40 V and c) 60 V. Top SEM images of MLTNTs for d) 80 V and e) 100 V. (the anodization was performed in 0.6 wt.% ammonium bi-fluoride salt ( $\text{NH}_4\text{F.HF}$ ), 96 ml diethylene glycol and 4 ml DI water at  $35^\circ\text{C}$  for 2h).

#### 4.1.3 Effect of anodization time

In this section, the effect of anodization time on the MLTNTs at  $35^\circ\text{C}$  and 60 V was investigated. As shown in Figure 4.3, the homogeneity and uniformity of MLTNTs enhanced by increasing the time of anodization. After 1h anodization, only some isolated bunch of MLTNTs was observed. However, with longer anodization time, the length and diameter of MLTNTs have not significantly altered. For example, the diameter and the length of MLTNTs reaches 330 nm and 4.2 μm after 6 h anodization, respectively.

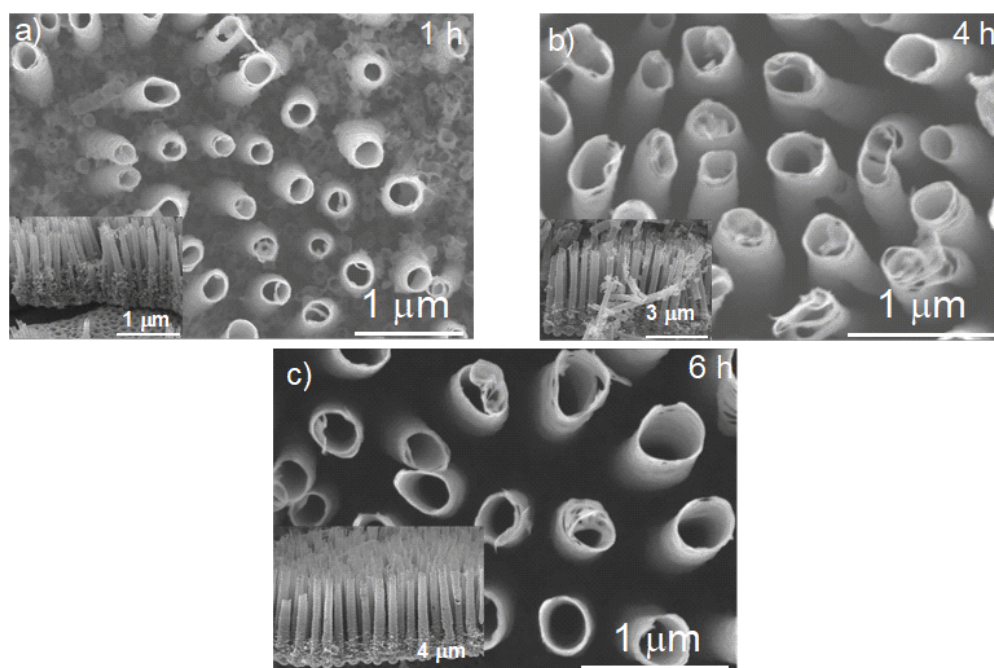


Figure 4.3 Top and cross section (inset) SEM images of MLTNTs for different anodization time a) 1h, b) 4h, and c) 6h (the anodization was conducted in 0.6 wt.% ammonium bi-fluoride salt ( $\text{NH}_4\text{F.HF}$ ), 96 ml DEG and 4 ml DI water at 60 V and temperature of  $35^\circ\text{C}$ ).

#### 4.1.4 Anodization in dimethyl sulfoxide (DMSO) electrolyte

In order to synthesize MLTNTs, DMSO instead of DEG and under similar optimized process at 60 V (for 2 h and  $35^\circ\text{C}$ ) was used. The SEM images show that the density of nanotubes increases while the diameter and length of nanotubes decreases to about 60 nm and 2.7 μm, respectively, compared to use the DEG (Figure 4.4). Regarding the obtained various morphologies of MLTNTs, anodization in presence of DEG and was performed at  $35^\circ\text{C}$  for 2 h by using a constant voltage of 60 V as an optimum situation.

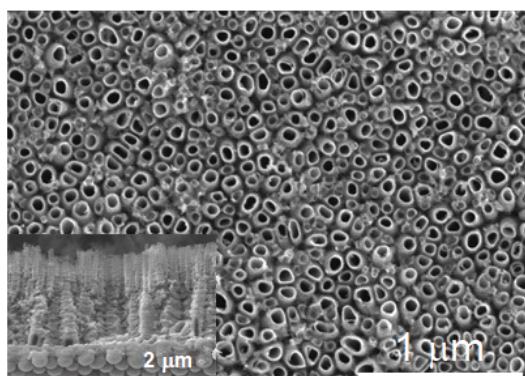


Figure 4.4 Top and inset cross-section SEM images of nanotubes obtained in 0.6 wt.% ammonium bi-fluoride salt ( $\text{NH}_4\text{F.HF}$ ), 96 ml DMSO and 4 ml DI water at  $35^\circ\text{C}$  for 2h.

With the optimum anodization conditions for MLTNTs (*i.e.*, temperature, time and voltage), long spaced TiO<sub>2</sub> nanotubes with appropriate diameter in DEG are obtained within 2 h.

#### **4.2 MLTNTs photoelectrodes modified by platinized cyanographene**

As we mentioned earlier (chapter 2), among various types of metal oxide semiconductors, TiO<sub>2</sub> as core component of PEC cell has been widely used owing to its many beneficial properties. During the last decade, 1D TNTs have been widely utilized because they can behave quite differently to the bulk counterparts in photocatalytic activity. As an example, not only do they provide a high aspect ratio that considerably increases the surface area available for catalytic reaction but also the light harvesting efficiency as well. The fast and directional pathway of photogenerated charge carriers is another advantage of 1D TNTs in which the drawback of the electron–hole recombination rate can be significantly suppressed. The new class of TiO<sub>2</sub> nanotube arrays consist of very well- defined and discrete MLTNTs has been reported when using DEG, HF, and DI water as an electrolyte solution under specific appropriate anodization conditions. However, in spite of favourable band edge positions *i.e.*, for H<sub>2</sub> evolution, TiO<sub>2</sub> suffers from low solar light absorption and high recombination rate of photoexcited charge carriers to provide appropriate corresponding redox half-reactions. Considerable effort has been made to introduce new approaches to overcoming its main disadvantages as well as improving the PEC activity of TiO<sub>2</sub> using various methods such as either doping of a foreign elements into TiO<sub>2</sub> or establishing different heterojunctions. Over the past decade, hundreds of articles have been published on the combination of TiO<sub>2</sub> nanostructures with carbon-based allotropes, such as carbon dots, graphitic carbon nitride (C<sub>3</sub>N<sub>4</sub>), graphene and its derivatives. The charge separation and absorption of light could be enhanced based on various heterojunctions owing to obtain the highly active hybrid photocatalysts. Graphene oxide (GO) and other derivatives of GO, such as reduced

graphene oxide (rGO), which are cost-effective is used to make a composites with  $\text{TiO}_2$  because of its unique physicochemical properties.

In the following section, we demonstrate that, platinized cyanographene (G-CN/Pt) MLTNTs and cyanographene (G-CN) MLTNTs composites (hereafter referred as G-NTs and G-Pt-NTs, respectively) have been successfully synthesized using a simple electrodeposition approach. The unique structure of highly ordered MLTNTs functionalized with G-CN and G-CN/Pt provide the morphology for formation of proper heterojunction, which can access to the top surface as well as space between the nanotubes walls. Compared to the pristine  $\text{TiO}_2$  nanotubes (P-NTs), G-CN and G-CN/Pt functionalized MLTNTs enhanced the PEC-WS activity response as well as declined the recombination rate of the charge carrier.

#### 4.2.1 Synthesis and characterization

Pristine and platinized cyanographene sheets have been synthesized successfully. Then, the fabricated material were characterized as shown in Figure 4.5. Cyanographene (G-CN) demonstrated the typical layered structure of fluorographene-derived (the reaction of NaCN with fluorographene) functionalized graphene [157,158] (Figure 4.5a). The G-CN decorated with homogeneous deposition of single  $\text{Pt}^{2+}$  ions using microwave has also been previously confirmed in detail by HRTEM, chemical mapping with EDS, and XPS spectroscopy [159]. After the reduction with  $\text{NaBH}_4$ , ultra-small Pt nanoparticles (nearly 98%) with diameter ranging from 0.5 to 2 nm have clearly appeared. The full spectrum of G-CN and G-CN/Pt are displayed in Figure 4.5e, showing the characteristic peak of Pt. Figure 4.5f shows the deconvoluted high-resolution XPS spectra of the Pt4f region for the atomic scale decorated G-CN/Pt sample. The peaks with binding energy for around 73.2 eV and 76.5 eV is higher than the typical binding energies for bulk metallic Pt. In addition, for the ultra-small size of Pt [159], such positive shifts could

be detected. The exact amount of Pt in the G-CN/Pt contained 2.3 wt.% determined by atomic absorption spectroscopy.

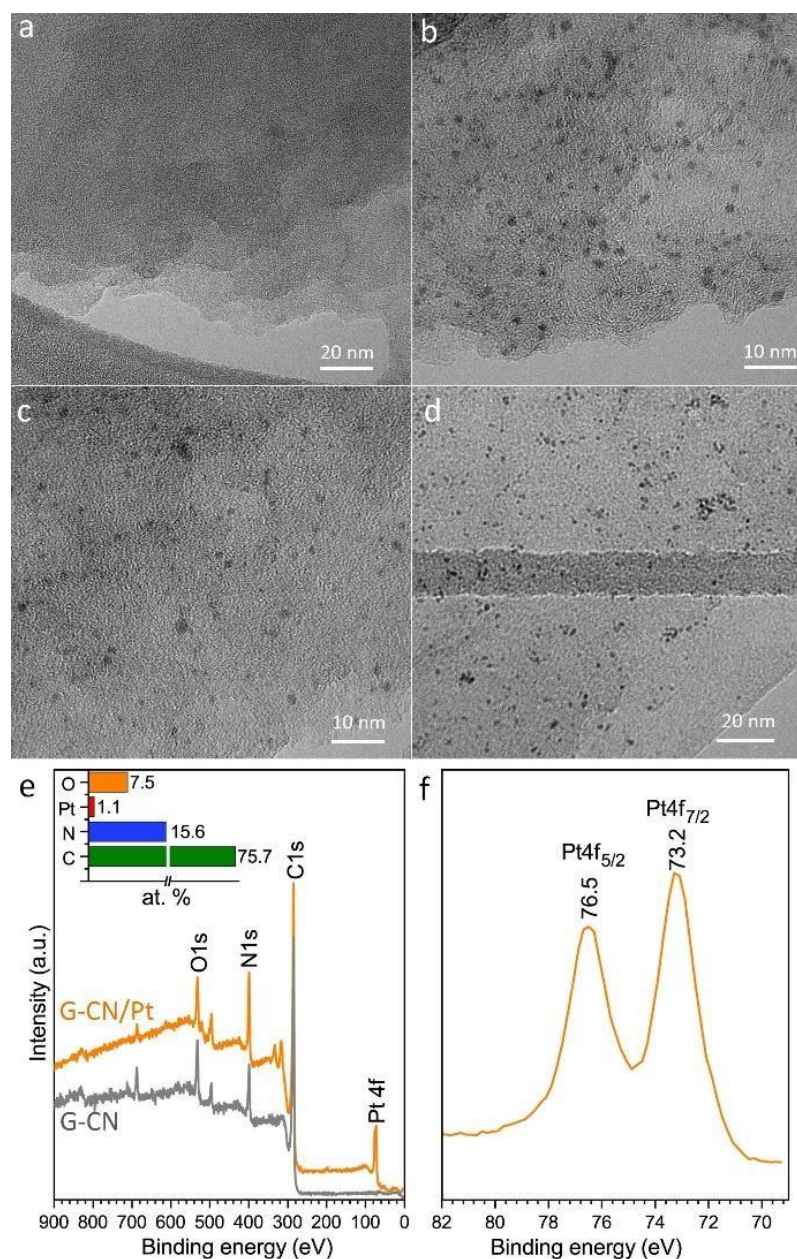


Figure 4.5 TEM images of a) the pristine cyanographene (G-CN) and b-d) after the formation and decoration with Pt nanoparticles (G-CN/Pt), (e) full XPS survey of G-CN and G-CN/Pt. The inset shows the atomic composition of G-CN/Pt. (f) HRXPS of the G-CN/Pt sample, showing the Pt 4f region.

In the following step, we synthesized MLTNTs at 60 V (35°C) for 2 h and combined them with G-CN and G-CN/Pt sheets. Figure 4.6a–f shows SEM images of the G-NTs and G-Pt-NTs composite that the G-CN and G-CN/Pt sheets electrodeposited onto TiO<sub>2</sub>

nanotubes not only randomly cover the top surface of the TiO<sub>2</sub> nanotubes but also accommodate deep inside the nanostructure, thus also covering the walls of the TiO<sub>2</sub> nanotubes. This would not be happen in typical close-packed arrays of TNTs, where the G-CN sheets would only be deposited on the top of the TiO<sub>2</sub> nanotubes arrays.

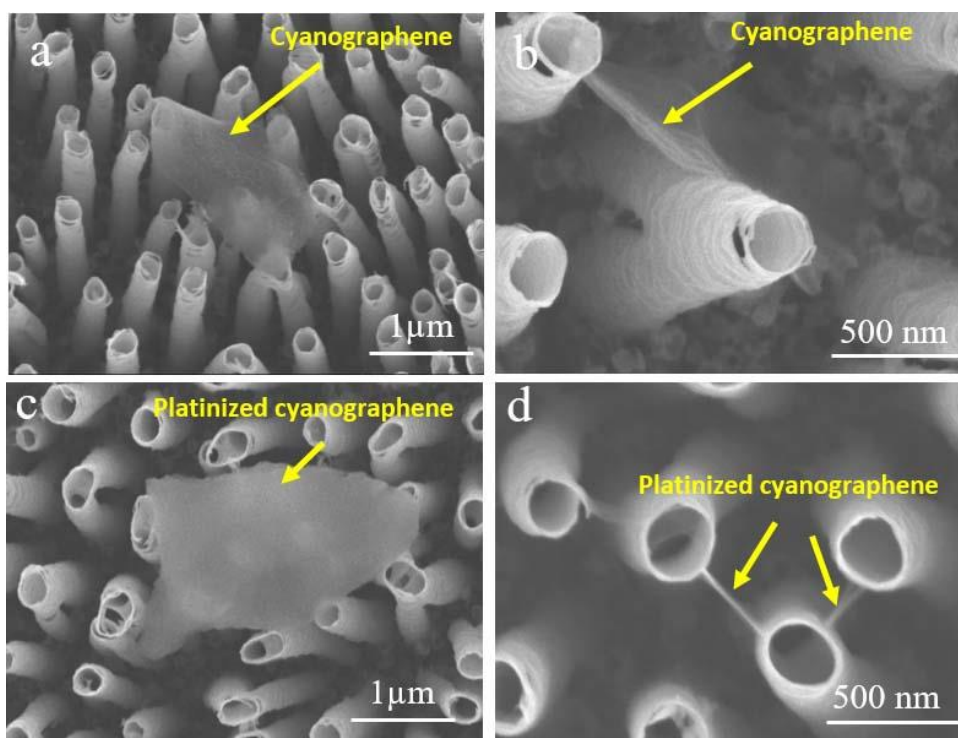


Figure 4.6 Top SEM images with different magnification of: a-b) G-NTs, c-d) G-Pt-NTs.

Raman spectroscopy was employed to confirm the existence of G-CN and G-CN/Pt on the surface of MLTNTs arrays. For those three samples (P-NTs, G-NTS, G-Pt-NTs), Figure 4.7a demonstrate the Raman peak at about 148, 396, 516 and 636 cm<sup>-1</sup> which is ascribed to the E<sub>g</sub>, B<sub>1g</sub>, B<sub>1g</sub> or A<sub>1g</sub> and E<sub>g</sub> vibration modes of anatase phase, respectively [160]. In addition, the two main peaks placed at 1365 and 1569 cm<sup>-1</sup> for the G-NTs and G-Pt-NTs composite samples, are attributed to the characteristic D band and G band of G-CN sample [161]. However, the D peaks is related to the structural disorder/defects and the G peaks stem from the bond stretching of all sp<sup>2</sup> carbon atoms (C-C) in G-CN sample [161,162]. Therefore, the presence of the G-CN on the MLTNTs was confirmed.

The amorphous as-prepared TiO<sub>2</sub> nanotubes were annealed at 450 °C for 180 min in air due to transformation them into crystalline structure. After the calcination, the crystal phase structures of the synthesized TiO<sub>2</sub> nanotubes were examined by XRD. As shown in Figure 4.7b, the XRD analysis showed that the formation of crystalline anatase phase with a very little contribution of rutile phase. The position of peaks is slightly shifted because of using Co source (instead of the commonly used Cu source) X-rays. Also, the oxidation of Ti metal beneath the TiO<sub>2</sub> nanotubes arrays at the interface of Ti/TiO<sub>2</sub> nanotubes during the annealing the sample results in the formation of very little rutile phase [163]. UV-vis DRS of pristine and composite samples (P-NTS, G-NTs, and G-Pt-NTs) were measured from 320 to 700 nm (Figure 4.7c). Further, the optical absorption enhancement phenomenon has also been investigated in a massive number of scientific works such as functionalization of semiconductors with nanocarbons (e.g., CNT and rGO) [164–166]. However, we found that there is a red-shift of absorption edge about 10-20 nm as well as a higher absorption of composite samples compared to pristine TiO<sub>2</sub> nanotubes (P-NTS) in the visible range of light spectrum. This could be ascribed to the electronic interactions between deposited cyanographene and TiO<sub>2</sub> nanotubes. The HRXPS C1s, Ti2P and Pt4f spectra of the G-Pt-NTs composite are shown in Figure 4.7d–f. The C1s peak for the G-Pt-NTs sample can be deconvoluted into four peaks. The peaks at 284.5, 286.0, 287 and 288.8 eV correspond to C-C, C-N, C=O and O=C-O, respectively, are related to the G-CN sample [161]. It means that the chemical structures of cyanographene has not changed during the electrodeposition process onto TiO<sub>2</sub> nanotubes. As shown in Figure 4.7e, the peaks at 459 and 464.7 belong to titanium (Ti<sup>4+</sup>). Moreover, as depicted in Figure 4.7f, the presence of Pt in metallic state (*i.e.*, Pt<sup>0</sup>) in G-Pt-NTs sample is confirmed by the two peaks at 71.4 and 42.9 eV.

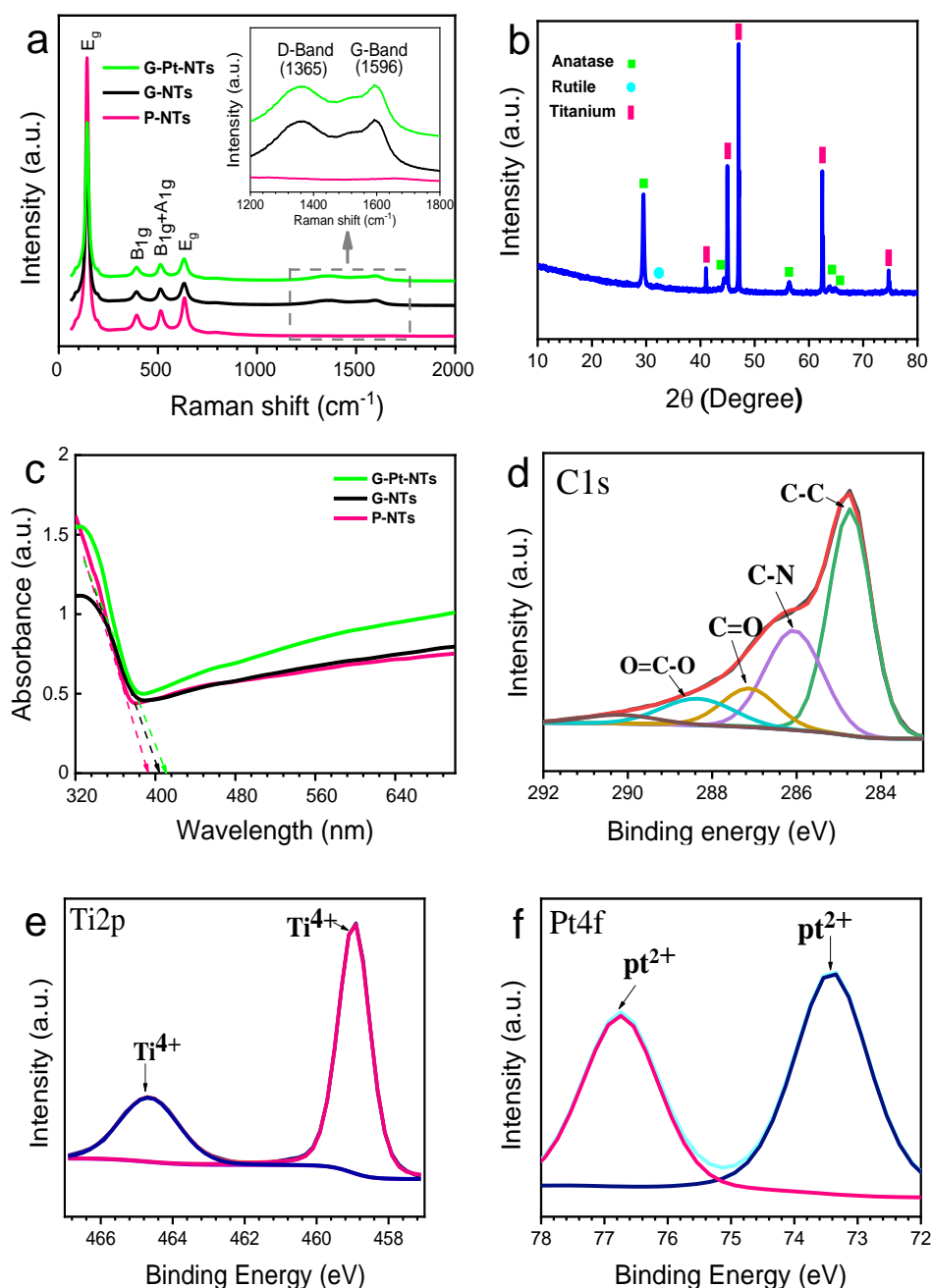


Figure 4.7 a) Raman spectra of P-NTs, G-NTs and G-Pt-NTs samples (the inset shows the magnified Raman spectra), b) XRD analysis of TiO<sub>2</sub> nanotubes using cobalt X-ray source calcined at 450°C in air, c) UV-vis DRS measurement of P-NTs, G-NTs, and G-Pt-NTs samples, and d–f) HRXPS spectra of d) C1s, e) Ti2p (e), and f) Pt4f of G-Pt-NTs sample.

#### 4.2.2 Photoelectrochemical performance of the structures

The electrochemical behaviour of the fabricated photoanode was investigated using LSV measurement under the simulated solar light illumination. Thermodynamically, the minimum voltage needed for water splitting is 1.23 V vs. reversible H<sub>2</sub> electrode (RHE).

Firstly, as shown in Figure 4.8 and Figure 4.9, the concentration of cyanographene was optimized (10 mg/L) and then has been coated onto the MLTNTs using the electrodeposition method. The MLTNTs on the titanium foils served as counter electrode, and the platinum sheet was used as the working electrode. The deposition was performed by applying a constant voltage of 100 V for 1 min, in which the G-CN solution was employed as an electrolyte. Finally, the fabricated composite sample was rinsed with DI water and ethanol respectively, and then dried using  $N_2$  stream. The photocurrent density

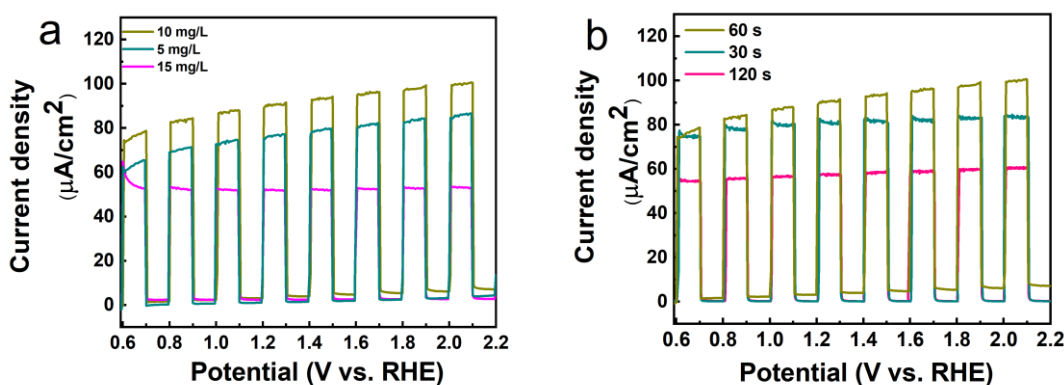


Figure 4.8 Photoelectrochemical response of composite samples obtained under 1 sun illumination ( $100 \text{ mW/cm}^2$  - AM1.5 G) in 1 M NaOH solution at different a) concentration of cyanographene and (b) electrodeposition time.

of P-NTs, G-NTs and G-Pt-NTs versus applied voltage (J-V curve) were measured in 1 M NaOH solution under AM 1.5 G illumination ( $100 \text{ mW/cm}^2$ ). From the Figure 4.10a, it is evident that for the composite samples compared to the P-NTs the photocurrent density is enhanced. For the G-Pt-NTs sample, the photocurrent density of  $121 \mu\text{A/cm}^2$

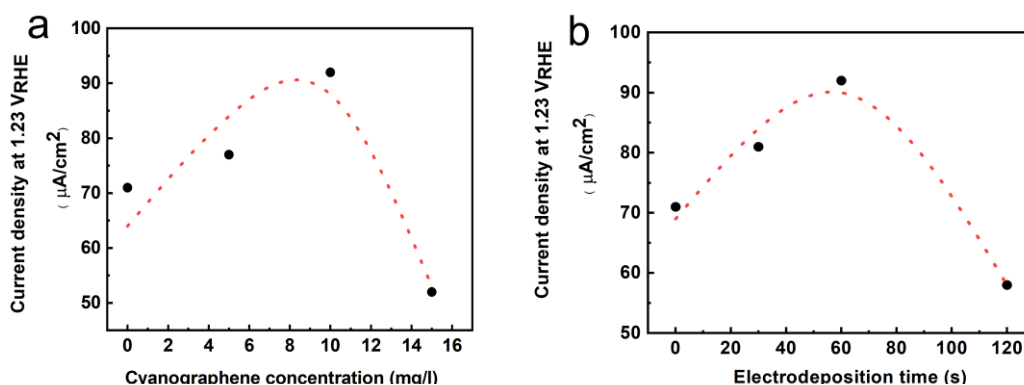


Figure 4.9 The effect of (a) G-CN concentration and (b) electrodeposition time on the PEC-WS.

(hereafter at 1.3 V vs. RHE) was achieved. In addition, for the G-NTs sample the photocurrent density was  $91 \mu\text{A}/\text{cm}^2$ , showing higher than P-NTs ( $91 \mu\text{A}/\text{cm}^2$ ). Thus, the photocurrent of the G-Pt-NTs sample is about 66% and 25% higher than that of P-NTs and G-NTs, respectively. This can be attributed to the efficient charge separation, as a direct result of using cyanographene and Pt in the composite sample. Moreover, the high work function of Pt metal could suppress the electron–hole recombination rate due to electron trapping in the metal.

Figure 4.10b shows the incident photon to current efficiency (IPCE) spectra of P-NTs, G-NTs and G-Pt-NTs samples in a 1 M NaOH solution at +1.5 V vs. RHE. The same trend was observed in the photoactivity among all three tested samples. Also, based on our experiment, all three photoanodes samples (P-NTs, G-NTs and G-Pt-NTs) show significantly enhanced photoactivity in the UV region. Furthermore, the G-Pt-NTs sample shows, in comparison with the other samples, the highest IPCE value which was approximately 58% at 300 nm. There are good agreement between the results of the PEC activity of the synthesized samples and their corresponding IPCE. The chronoamperometry test was carried out on the most active G-Pt-NTs sample to examine its photostability over the time (Figure 4.10c). The test was performed with the fixed bias voltage +1.5 V vs. RHE and continuous light irradiation for 7 h in 1 sun. After this certain time, the PEC test of the photoanode (G-Pt-NTs) has represented acceptable stability and reached about 90% of initiating current.

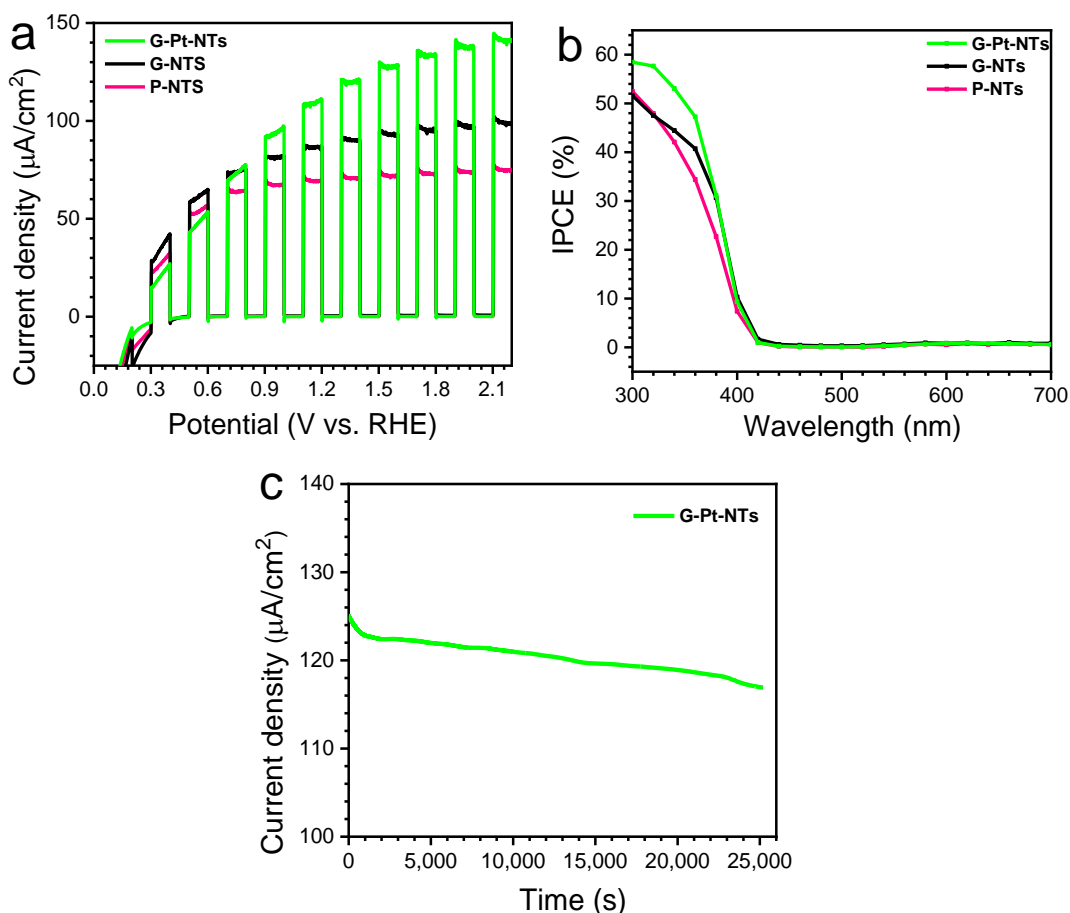


Figure 4.10 a) Photoelectrochemical response of fabricated samples measured under 1 sun illumination ( $100 \text{ W}/\text{m}^2$ - AM1.5 G) in 1 M NaOH solution, b) corresponding IPCE spectra, and c) chronoamperometry test of G-Pt-NTs in 1 M NaOH solution, potential 1.5 V vs RHE for 7 h where the pH is 13.6 ( $E_{\text{Ag}/\text{AgCl}}^0 = 0.197 \text{ V}$  at 298 K, and  $E_{\text{Ag}/\text{AgCl}}^0$  is the measured potential vs. Ag/AgCl).

We assumed that the enhanced PEC activity of the composite samples could be ascribed to the increased charge separation efficiency. In order to prove this, we measured the electrochemical impedance spectroscopy (EIS) under 1 sun illumination in the frequency range of 0.1 Hz to 100 kHz at the bias potential +1.5 V vs RHE. The Nyquist plots obtained for P-NTs, G-NTs and G-Pt-NTs samples are shown in Figure 4.11a. Furthermore, we have fitted the impedance spectra of photoelectrodes shown as an inset of Figure 4.10a under illumination to an equivalent circuit using Z-View software (see Table 4.1). The  $R_s$  representing as the overall resistance between the electrode and electrolyte. This value was determined from the X-intercept of Nyquist plot.

Table 4.1 Equivalent circuit components calculated by fitting the experimental electrochemical impedance spectroscopy data.

Sample	$R_s$ ( $\Omega$ )	$R_{sc}$ ( $\Omega$ )	$R_{ct}$ ( $\Omega$ )	CPE-1 ( $\mu\text{F}$ )	CPE-2 ( $\mu\text{F}$ )	$\tau = R_{ct} \times$ CPE2 (s)
P-NTs	$11.46 \pm 0.11$	$95.7 \pm 11.1$	$105,940 \pm 2828$	$2.61 \pm 0.15$	$70.20 \pm 0.7$	7.43
G-NTs	$10.22 \pm 0.09$	$88.28 \pm 9.2$	$38,442 \pm 992$	$27.2 \pm 0.9$	$102.99 \pm 0.5$	3.95
G-Pt-NTs	$11.01 \pm 0.09$	$106 \pm 19.1$	$27,954 \pm 625$	$187 \pm 11$	$78.10 \pm 0.9$	2.18

The  $R_s$  value for P-NTs, G-NTs, and G-Pt-NTs composite was determined to be 11.46  $\Omega$ , 10.22  $\Omega$  and 11.01  $\Omega$ , respectively. Similarly, the  $R_{sc}$  value, which is corresponding to the bulk charge transport, was also determined; however, the difference is negligible. In addition, the radius of semicircle for the G-Pt-NTs sample is smaller than P-NTs and G-NTs ones, and it decreases in the following order: P-NTs > G-NTs > G-Pt-NTs, showing fastest interfacial hole transfer and efficient separation of electron-hole pairs. The  $R_{ct}$  is assigned to the interfacial charge transfer resistance. The fitting these parameters ( $R_{ct}$ ) yield a value of 105940  $\Omega$  for P-NTs, which is much higher than 38442  $\Omega$ , and 27954  $\Omega$  for G-NTs, and G-Pt-NTs composite sample, respectively. Several insights can be deduced from this data; i) when compared to the pristine nanotubes (MLTNTs), the pristine G-CN greatly enhanced the charge transfer kinetics to TiO<sub>2</sub> nanotubes, reducing by approximately 63.7%  $R_{ct}$ ; ii) the presence of Pt in G-CN/Pt sample could be the key point in further enhancing composite performance by an additional ~27%, attributed to the positive influence of Pt on charge separation. The constant phase elements (CPE) reflects capacitance of space charge layer ( $C_{sc}$ ) as well as the semiconductor electrolyte interface ( $C_{SE}$ ), calculated by CPE-1 and CPE-2 respectively [167,168]. The value of CPE-1 follows the trend of P-NTs < G-NTs < G-Pt-NTs, indicating the considerable improvement in e<sup>-</sup>-h<sup>+</sup> pair separation of G-Pt-NTs in comparison with two other samples (P-NTs and G-NTs). Interestingly, the value of CPE1 is greatly increased for G-Pt-NTs (approximately 72 times) than P-NTs. It can be

concluded that the efficient role of G-CN/Pt as a charge carrier separator across the space charge region compare to Pt and G alone of the composite photoanodes, which is indeed the beneficial role of platinized G-CN, acting as a charge storage reservoir that can improve overall photocurrent enhancement. Further, the obtained value of CPE-2 represents the charge transferability of photoanode to the electrolyte, which is higher for G-Pt-NTs compared to Pt-NTs, but lower compared to G-NTs.

The rate constant ( $\tau$ ) of the charge transfer process across the photoanode/electrolyte interface (Table 4.1) is determined to get the correlation between charge transfer efficiency and corresponding photocurrent enhancement [168]. The lower value of  $\tau$ , the higher the charge transfer efficiency, following the order P-NTs > G-NTs > G-Pt-NTs, and is well in accordance with the trend for photocurrent enhancement. Therefore, the higher photocurrent of G-Pt-NTs than two others (P-NTs and G-NTs) could be attributed to two issues. Firstly, the improvement of charge separation (CPE1). Secondly, reduction of charge transfer resistance ( $R_{ct}$ ) of photoanodes, and the same is reflected in time constant corresponding to charge transfer process. This trend can be ascribed to the presence of G-CN/Pt and G-CN in the fabricated composite samples. Indeed, to test the transport time of photo-generated electron, the intensity-modulated photocurrent spectroscopy (IMPS) was conducted at different intensity of light. Furthermore, the transform time of photo-generated electron can be calculated using the formula below [169]:

$$\tau_{trans} = \frac{1}{2\pi f_{min}} \quad (4.1)$$

Where  $\tau_{trans}$  means the electron transform time to the back layer and  $f_{min}$  is the minimum frequency of IMPS plot. A comparison between IMPS results of P-NTs and the TiO<sub>2</sub> composite samples (G-NTs and G-Pt-NTs) is shown in Figure 4.11b. The G-Pt-NTs and G-NTs shown the fastest electron-transfer time, respectively (see Table 4.2). Based on

this observation, using cyanographene and platinized cyanographene can provide better charge separation, thereby increasing the photocurrent which is in correlation with  $\tau$  obtained from EIS measurements discussed above. The open-circuit voltage decay ( $V_{\text{OCD}}$ ) measurement was examined according the investigation reported by Zaban et al. [170] to access the recombination properties of fabricated samples. A photogenerated potential is built up by illumination of photoelectrode at open-circuit potential. Then, the illumination is interrupted and the exponential decay of  $V_{\text{OCD}}(t)$  from the illuminated quasi-equilibrium state to darkness is monitored while the cell is kept at open circuit potential. According to the  $V_{\text{OCD}}$  curve, the electron lifetime could be obtained through the equation below [170]:

$$\tau_n = -\frac{k_B T}{e} \left( \frac{dV_{\text{OC}}}{dt} \right)^{-1} \quad (4.2)$$

Where  $k_B$  is the Boltzmann constant,  $T$  is a temperature (K) and  $e$  is a charge of electron. The open-circuit voltage decay curves for the three samples and the electron lifetime ( $\tau_n$ ) as a function of  $V_{\text{OCD}}$  plot are shown in Figure 4.11c and d, respectively. It can be seen, the G-Pt-NTs composite sample shows the slowest voltage decay rate in comparison with the other samples, while the pristine  $\text{TiO}_2$  shows a much faster. Therefore, at the equal potential and by applying the equation (4.2) to the data in Figure 4.11c, the electron lifetime was observed in the following order  $\text{G-Pt-NTs} > \text{G-NTs} > \text{P-NTs}$  (Figure 4.11d). For instance, at voltage of 1.6 V the electron lifetime for pristine and composite samples i.e.; P-NTs, G-NTs, and G-Pt-NTs was 1.3 s, 2.21 s, and 11.25 s, respectively. The obtained results showed that the photo-electrodes recombination rate in the cyanographene composite samples are slower than of pristine  $\text{TiO}_2$  nanotubes.

Table 4.2 The electron transfer time ( $\tau_{trans}$ ) of photogenerated electrons for the pristine and composite samples calculated through IMPS data analysis.

Sample	$\tau_{trans}$ (ms) at light power 80 W	$\tau_{trans}$ (ms) at lightpower 25 W	$\tau_{trans}$ (ms) at lightpower 8 W
P-NTs	1.5	2	5
G-NTs	1	1.3	2.5
G-Pt-NTs	0.5	1	2.1

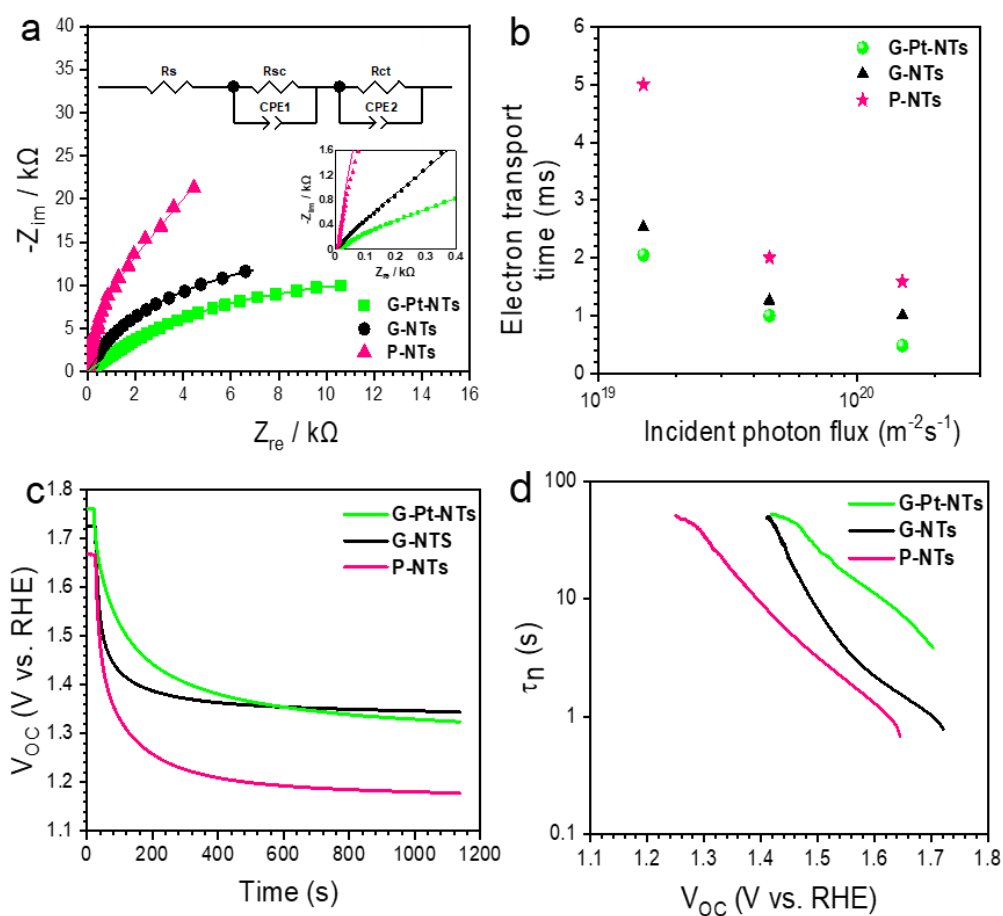


Figure 4.11 a) The Nyquist plots demonstrating EIS spectra of P-NTs, G-NTs, and G-Pt-NTs samples obtained in 1 M NaOH solution at 1.5 V vs. RHE. The EIS at high frequency and the equivalent circuits used to fit the impedance spectra has shown in inset. b) Comparison of  $\tau_{trans}$  of photogenerated electron for the pristine nanotube (P-NTs) and composite samples (G-NTs, and G-Pt-NTs) as a function of incident photon flux at 369 nm (monochromatic light). c)  $V_{OC}$  decay measurement of P-NTs, G-NTs, and G-Pt-NTs samples under 1 sun ( $100 W/m^2$  –AM 1.5 G) illumination, and d) corresponding  $\tau_n$ .

### 4.2.3 Conclusion

In conclusion, we applied a simple electrodeposition technique to successfully make the (platinized) cyanographene MLTNTs composites. The unique structure of MLTNTs with combination of G-CN and G-CN/Pt provides the special morphology, to functionalize not only the top surface of the nanotubes but also the space between the synthesized  $\text{TiO}_2$ . In Comparison with P-NTs (pristine  $\text{TiO}_2$  nanotubes), it has been observed that the G-Pt-NTs and G-NTs samples improved the photocurrent density by 66% and 25% under 1 sun illumination, respectively. This can be as a consequence of the efficient charge separation and transfer. Based on EIS and IMPS analysis, cyanographene as well as the small Pt nanocrystals deposited on it can play an important role in enhancing the photoelectrochemical performances in the composites materials.

### 4.3 Fabrication of compact $\text{TiO}_2$ nanotubes (TNTs)

To investigate the feasibility of employing post-treatment on  $\text{TiO}_2$  nanotubes grown on Ti sheet with two different electrolytes ( $\text{NH}_4\text{F}$  and HF) with the aim of synthesizing open nanotubes without initiation layer, we applied the two different strategies.

#### 4.3.1 Mechanical treatment

The TNTs used in Figure 4.12 are formed by double-anodization of Ti sheet in  $\text{NH}_4\text{F}$  (0.15 M), ethylene glycol and DI water (3 wt. %) at 20V for 10 min. Then, we increased the anodization voltage to 70 V for 10 min. The results showed the formation of two various shape of  $\text{TiO}_2$  nanotubes: (i) short nanotubes on the top and (ii) long nanotubes with the length of 6  $\mu\text{m}$  on the beneath of short nanotubes. After synthesizing TNTs, the initiation layer covered the top surface of nanotubes. The sonication in water and dilute HF solution was used for removing the short nanotubes as well as the inanition layer.

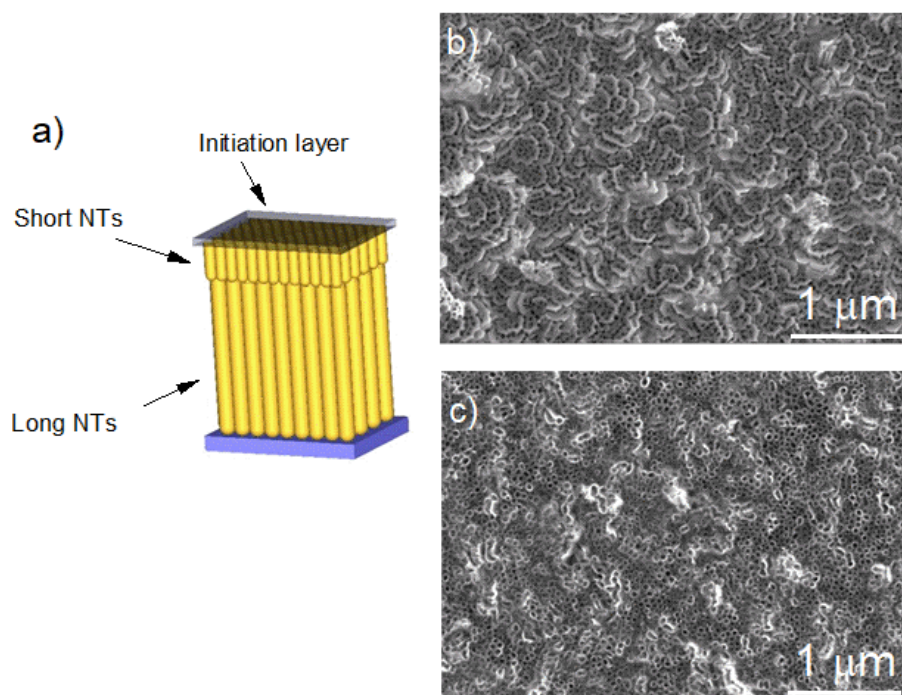


Figure 4.12 a) Schematic illustration of synthesized TNTs. Top SEM images of b) as-synthesized TNTs and c) after post-treatment. (Anodization was performed in 0.15 M  $\text{NH}_4\text{F}$  ethylene glycol and 3 wt. % DI water at 20V for 10 min, followed by 70 V for 10 min).

### 4.3.2 Chemical treatment

As shown in Figure 4.13, TNTs were prepared by anodizing of Ti sheet in an electrochemical bath consisting of HF (0.2 M), ethylene glycol and distilled water (4 wt. %) at room temperature for 30 min by using a constant voltage of 70 V. To remove the initiation layer from top of synthesized nanotubes, the sonication in water and dilute HF solution was employed. After sonication of fabricated TNTs, the initiation layer was removed and only completely open TNTs appear.

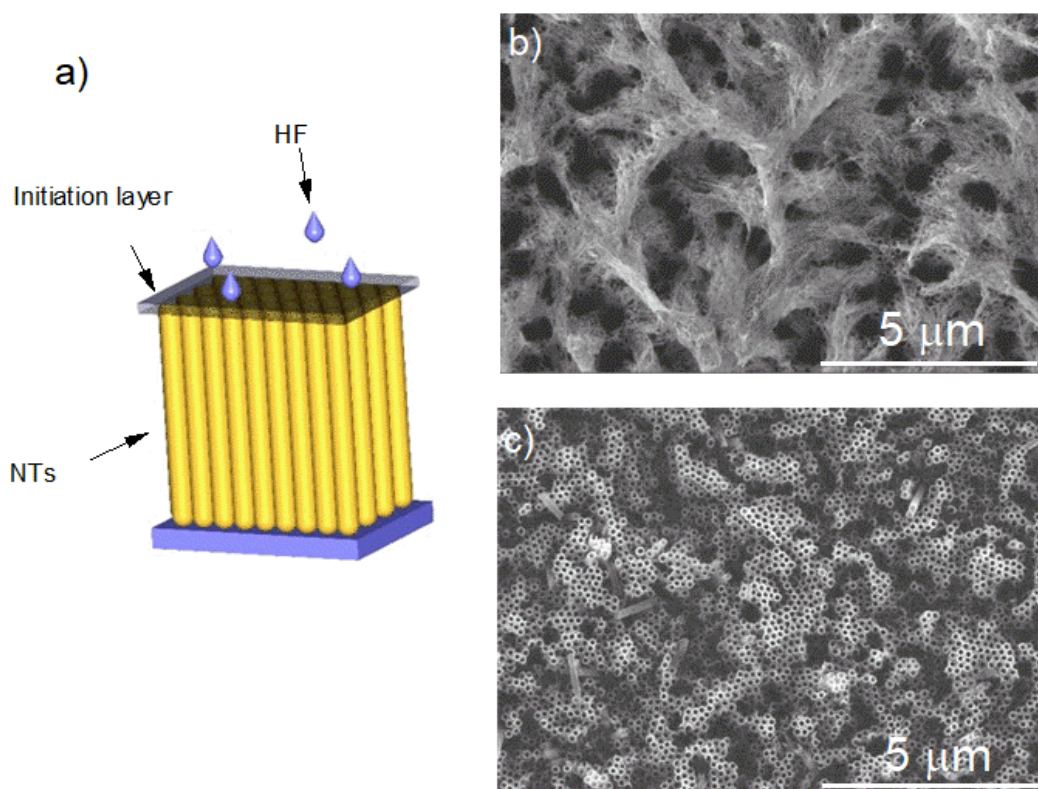


Figure 4.13 a) Schematic representation of synthesized TNTs. Top SEM images of b) as-synthesized TNTs and c) after post-treatment. (Anodization was performed in 0.2 M HF ethylene glycol and 4 wt. % DI water at 70 V for 30 min)

#### 4.4 Controlled loading of Pt single atoms as a co-catalyst on reduced TiO<sub>2</sub>

Because of environmental crisis and energy shortage [7,171–173], the chemical conversion of molecular pollutants into added-value products by chemical reactions is one of the significant strategy to tackle these urgent issues. In this scenario, appropriate catalysts with high active surface area have been designed in order to increase the rate of desirable reactions with higher products selectivity and catalyst efficiency.

Single-atom catalysts (SACs) have recently shown to provide higher selectivity and excellent catalytic behaviour in a variety of chemical reactions, which provide the opportunity to the 100% of atomic utilization in catalytic reactions [174,175]. Compared to nanoparticles catalysts (NPCs), SACs performing the construction of an affordable catalyst by thrifting the use of precious metals such as Pt, Au, Rh and Pd [176,177] because of their remarkable reactivity and utmost atom efficiency.

Control of synthesis parameters along with supporting material play crucial role to tune interaction between atoms and thereby providing highly active SA catalysts. TiO<sub>2</sub> among various types of metal oxide as a model supporting material, has been the focus of high interest due to its unique properties, mentioned before as well as formation of various defects [70,124,178–180]. Decoration of TiO<sub>2</sub> surface with noble metals like Pt, which has the lowest overpotential and largest work function (from the electronic and catalytic point of view), is one of the promising approach to improve the photocatalytic H<sub>2</sub> production [181]. Since, Pt is scarce and expensive, with reducing the particle size of catalyst to the atomic-scale, not only the efficiency of catalyst is reached to the highest level but also makes it cost-effective [108,182]. For the sake of simplicity, pristine TNTs arrays, sonicated TNTs and Pt-decorated TNTs are hereafter referred to as P-NT, Rx-NT (x=30, 40, 50, 60, 70 and 80 min) and R50/Pt-NTy (y=1, 10, 15, 30 and 60 min), respectively.

#### **4.4.1 Characterization of fabricated nanostructures**

The TNTs were synthesized through the electrochemical anodization of Ti foil. The as-synthesized nanotubes have amorphous phase, while, as shown in Figure 4.14, the XRD pattern of the calcined P-NT sample shows the anatase phase at 450°C for 2h. Then, in order to form structural and electronic defects on the TNTs surface, the fabricated samples have been subjected to the ultrasound post-treatment (140 W with a frequency of 18.1 KHz) for different sonication time (30, 40, 50, 60, 70 and 80 min) in Ar atmosphere. All the TNTs sonicated samples maintained only the anatase crystalline phase without any phase changes.

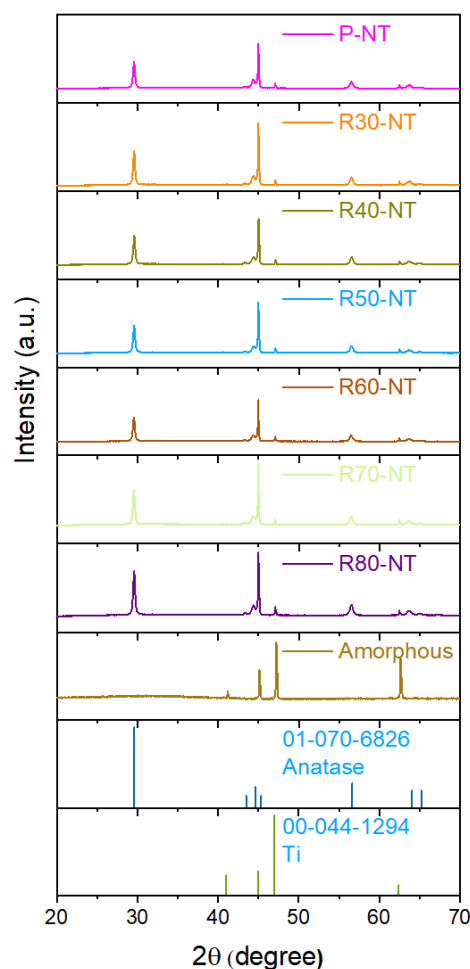


Figure 4.14 XRD patterns of pristine and sonicated TNTs using a cobalt X-ray source.

Figure 4.15a shows SEM images of the P-NT sample featuring a morphology with the open top. We report the SEM image of sample sonicated for 50 min (R50-NT), as an example morphology of sonicated TNTs for different time. The quite similar morphology and completely open TNTs can be seen for sonicated sample (Figure 4.15b). The mean diameter and the length of P-NT sample were 100 nm and 6.1  $\mu\text{m}$ , respectively (Figure 4.15a,c).

To gain some information in regard to the band gap narrowing phenomenon and improvement of photophysical properties of the sonicated sample (R50-NT), the occupied density of state (DOS) through the valence band (VB) XPS spectra and UV-DRS

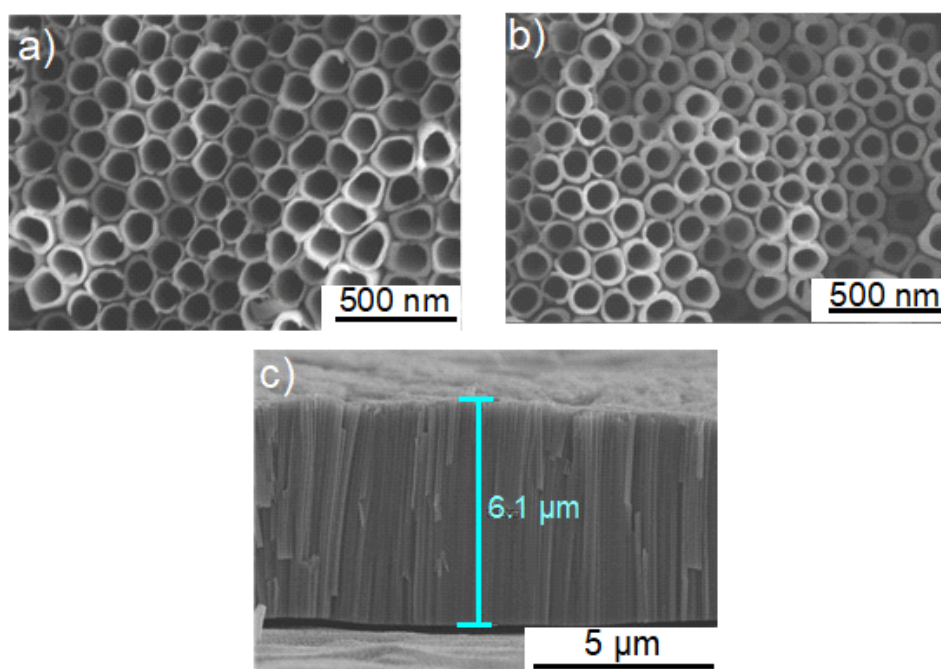


Figure 4.15 SEM image of samples: a) pristine synthesized  $\text{TiO}_2$  (P-NT), b) sonicated sample for 50 min (R50-NT), and c) demonstrating cross section of P-NT.

reflectance results (Figure 4.16a-d) has been measured. Valence band maxima is determined by linear extrapolation of the peaks to the baseline. The P-NT sample showed the maximum energy of VB in DOS at +2.8 eV. However, as shown in Figure 4.16d for the sonicated sample (R50-NT), the maximum level of VB energy was calculated at +2.9 eV, following by a band tail extending up to +1.5 eV. The optical band gap energy of P-NT and R50-NT sample based on UV-Vis DRS measurements are 3.2 eV and 3.1 eV, respectively. As a result, the conduction band minimum of sonicated sample for 50 min and pristine nanotubes (R50-NT and P-NT) could be located at -0.2 and -0.4 eV, respectively. Thus, the observed band gap narrowing of the sonicated sample (R50-NT) can be ascribed to the small tailing of valence band. A combination of these results (valence band XPS along with the optical band gap measurement) confirms that using the sonication to reduce TNTs could form structural disorder and defects thereby inducing a shift of the valence band maxima and conduction band minima [183].

In addition, as demonstrated in Figure 4.16c,d, these results represent the formation of localized states above the valence band upon TNTs reduction. From the Figure 4.16e, the influence of sonication on the chemical composition and the surface characterization of R50-NT sample was further investigated by XPS analysis. The Ti2p spectrum of the pristine and sonicated samples (P-NT and R50-NT, respectively) contains two broad peaks at 458.6 eV and 464.4 eV are related to the Ti2p<sub>3/2</sub> and Ti2p<sub>1/2</sub> orbitals of Ti<sup>4+</sup> in TNTs lattice, respectively [138,184]. The two more small peaks appear at lower binding energies for the R50-NT sample can be assigned to Ti<sup>3+</sup> species [185,186].

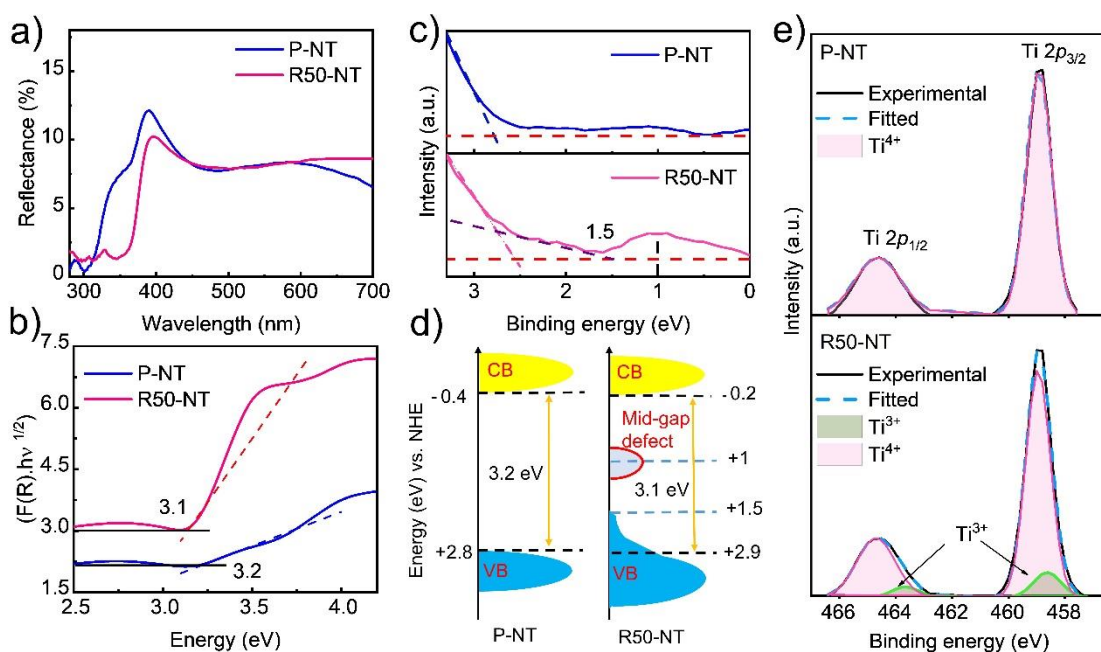


Figure 4.16 a) UV-Vis DRS measurement of P-NT, R50-NT samples, b) bandgap energies calculation for P-NT and R50-NT, c) XPS valence band spectra of P-NT and R50-NT, d) schematic illustration of DOS for P-NT and R50-NT, and e) HRXPS spectra in the Ti2p region for P-NT and R50-NT.

#### 4.4.2 Photoelectrochemical performance of TiO<sub>2</sub> as a substrate

The PEC-WS activity of sonicated samples with different time of sonication has been carried out owing to select the most efficient sample for decoration with SA-trapping of Pt. Current density-voltage (J-V) behaviour of sonicated samples were obtained in the dark and light using AM 1.5 G illumination (100 mW cm<sup>-2</sup>). As shown in Figure 4.17a,

b, PEC activity shows that all sonicated samples possess higher PEC activity compared to the pristine one (P-NT) because of the defect formation, which may enhance donor density and charge carrier transport [187,188]. The R50-NT sample demonstrated highest anodic photocurrent density of  $100 \mu\text{A cm}^{-2}$  at 1.23 V under solar light irradiation. Sonicated TNTs (*i.e.*, R50-NT) has shown about two times higher PEC activity in comparison with non-sonicated TNTs (P-NT). Consequently, R50-NT as main sample for decoration with Pt-SA, Pt-NP has been selected.

As seen in Figure 4.17c, the Mott-Schottky plots has shown a positive slopes for both samples (P-NT and R50-NT electrodes), presenting n-type semiconductor behaviour [189]. In addition, the carrier density is determined by the following equation:

$$N_D = - \left( \frac{2}{e\epsilon\epsilon_0} \right) \left( \frac{d\left(\frac{1}{C^2}\right)}{d(E_S)} \right)^{-1} \quad (4.3)$$

Where  $N_D$  is the carrier density of electrons, the  $C$  is the space charge capacitance for the semiconductor,  $e$  is the electrical charge,  $\epsilon_0$  is the permittivity of the vacuum,  $K_B$  is the Boltzmann constant,  $\epsilon$  is the relative permittivity of semiconductor,  $E_s$  is the applied potential,  $E_{FB}$  is flat potential and  $T$  is the absolute temperature. Here,  $e = -1.6 \times 10^{-19}$ ,  $\epsilon_0 = 8.86 \times 10^{-12} \text{ Fm}^{-1}$ , and  $\epsilon = 48$  for  $\text{TiO}_2$  in anatase phase [190]. The carrier density values obtained for R50-NT and P-NT were  $1.43 \times 10^{16} \text{ cm}^{-3}$  and  $0.92 \times 10^{16} \text{ cm}^{-3}$ , respectively. It can be deduced that the sonication reduction process boosted the electron density of sonicated sample (R50-NT). This is because of the insertion of defects such as oxygen vacancy and  $\text{Ti}^{3+}$  states [191]. To understand the contribution of each wavelength to the photocurrent density, incident photon to current efficiency (IPCE) spectra of P-NTs, R50-NT photoanode were carried out at +1.5 V vs. RHE in a 1 M NaOH solution. The IPCE can be calculated according to the following formula below [173]:

$$IPCE (\%) = \frac{I_{sc}(A)}{P(W)} \times \frac{1240}{\lambda(\text{nm})} \times 100 \quad (4.4)$$

Where  $I$  is the obtained photocurrent density ( $\mu\text{A cm}^{-2}$ ),  $\lambda$  is the incident light wavelength (nm) and  $P$  is the irradiated incident light at specific wavelengths. The R50-NT demonstrated the greatly enhanced IPCE value in the UV region and reached to the approximately 70% at 380 nm, whereas for the P-NT sample was about 50%. (Figure 4.17d). From this observation, we can see that the efficient charge separation and transfer is mainly improved for UV-promoted electronic transitions (*i.e.* associated to VB to CB transitions) [138]. In particular, a relatively small increased photocurrent of R50-NT is observed over the visible region (inset Figure 4.17d), which can be ascribed to the higher absorption of light in this region [192,193].

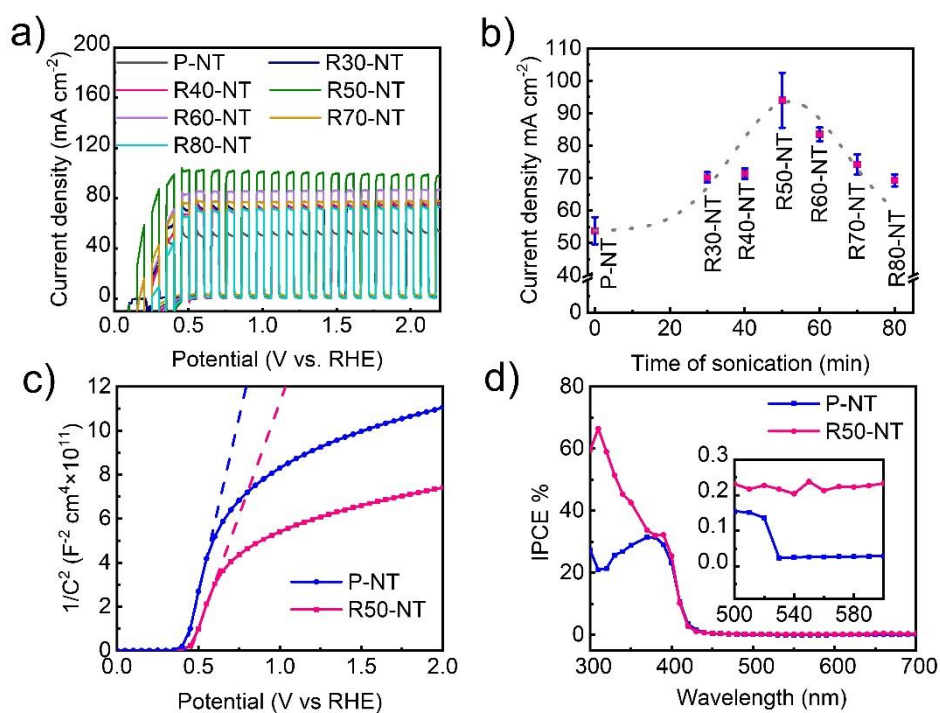


Figure 4.17 a) Photoelectrochemical measurement of TNTs samples sonicated for different time (from 30 to 80 min) under 1 sun illumination ( $100 \text{ mW cm}^{-2}$  - AM1.5 G) in 1 M NaOH solution, b) comparison of photocurrent density at 1.23 V for the corresponding samples, c) The Mott-Schottky plots of P-NT and R50-NT samples obtained at a frequency of 5 KHz in the dark and d) corresponding IPCE spectra.

EIS was conducted under 1 sun illumination at the bias voltage +1.5 vs. RHE in the range of 0.1 Hz to 100 KHz ( $100 \text{ mW cm}^{-2}$ ). It revealed that the lower resistance to charge transfer at the electrode/electrolyte interface due to the obtained semicircle radius from

Nyquist diagram of EIS data, for the R50-NT sample is smaller than that of P-NT (Figure 4.18) [7]. Therefore, the sonicated TNTs for 50 min (R50-NT) because of lower resistivity (promotion of faster charge transfer) as well as higher concentration of electron donor ( $N_D$ ) have shown higher PEC activity than pristine nanotubes.

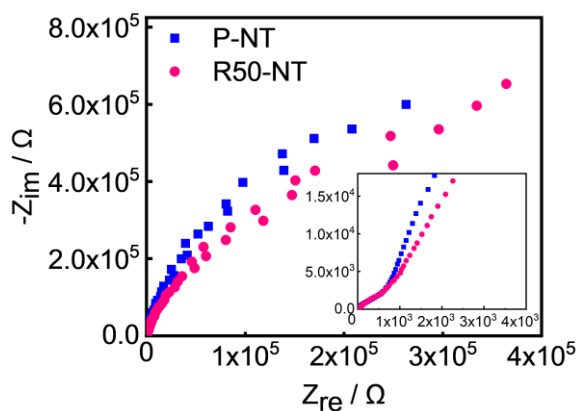


Figure 4.18 Nyquist plots representing electrochemical impedance spectra of P-NT and R50-NT samples.

#### 4.4.3 Deposition of Pt single atom and material characterization

To decorate with Pt SA-trapping, we soaked the fabricated substrate in very dilute Pt containing solution. TEM images of samples sonicated for 50 min and decorated with different amount of Pt is shown in Figure 4.19. The impregnation process was carried out in 100  $\mu$ M hexachloroplatinic acid solution for various time, including 1, 10, 15, 30 and 60 min. The results of energy dispersive spectrometry (EDS) analysis shows that Pt is not detectable in the final composition of elements for the impregnation time less than 15 min, which is in agreement with the TEM observation (Figure 4.20a). However, Pt can be clearly visualized for the 30 and 60 min impregnation time (R50/Pt-NT30 and R50/Pt-NT60). Moreover, the Figure 4.20b shows very narrow Pt nanoparticles on sonicated TNTs (R50/Pt-NT60) with an average diameter of about 1.5 nm. As shown in Figure 4.19b, the presence of Pt-SA on the surface of TNTs has been confirmed by carrying out the high-angle-annular-dark-field scanning transmission electron microscopy (HAADF-STEM). The large number of marked bright dots, presenting highly distributed Pt-SA in

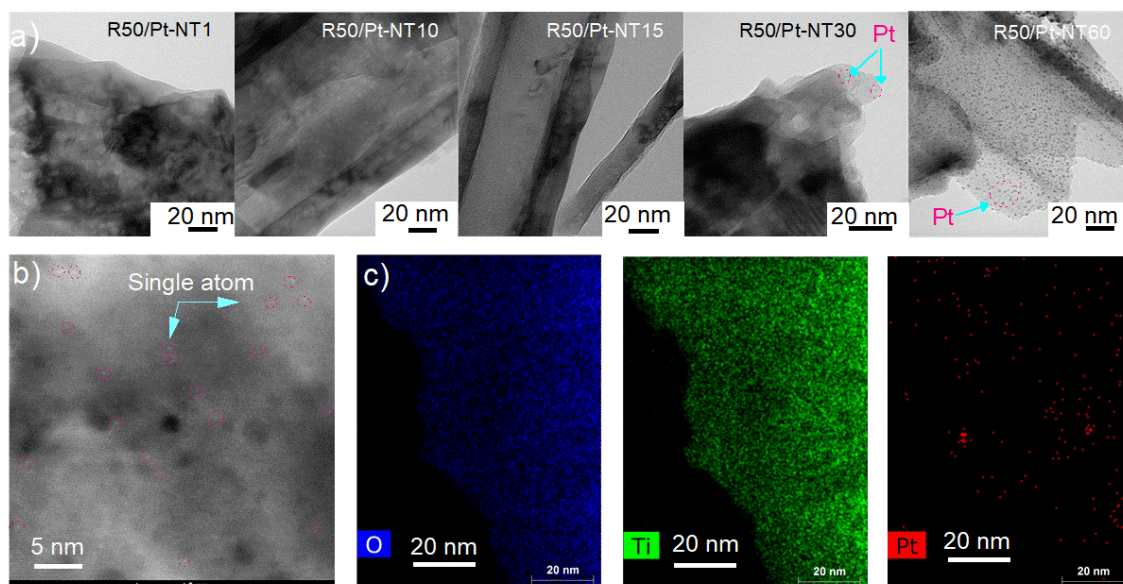


Figure 4.19 a) TEM images of treated samples at various soaking time ranging from 1 to 60 min in very dilute hexachloroplatinic acid solution, b) HAADF-STEM image and c) the corresponding EDS elemental mapping of R50/Pt-NT10 sample.

the form of the isolated single atom on the surface of R50/Pt-NT10 sample. EDS mapping was performed for evaluation the distribution of O, Ti and Pt of the catalyst. As shown in Figure 4.19c, the EDS map of Pt, Ti and O elements of the R50/Pt-NT10 sample confirms

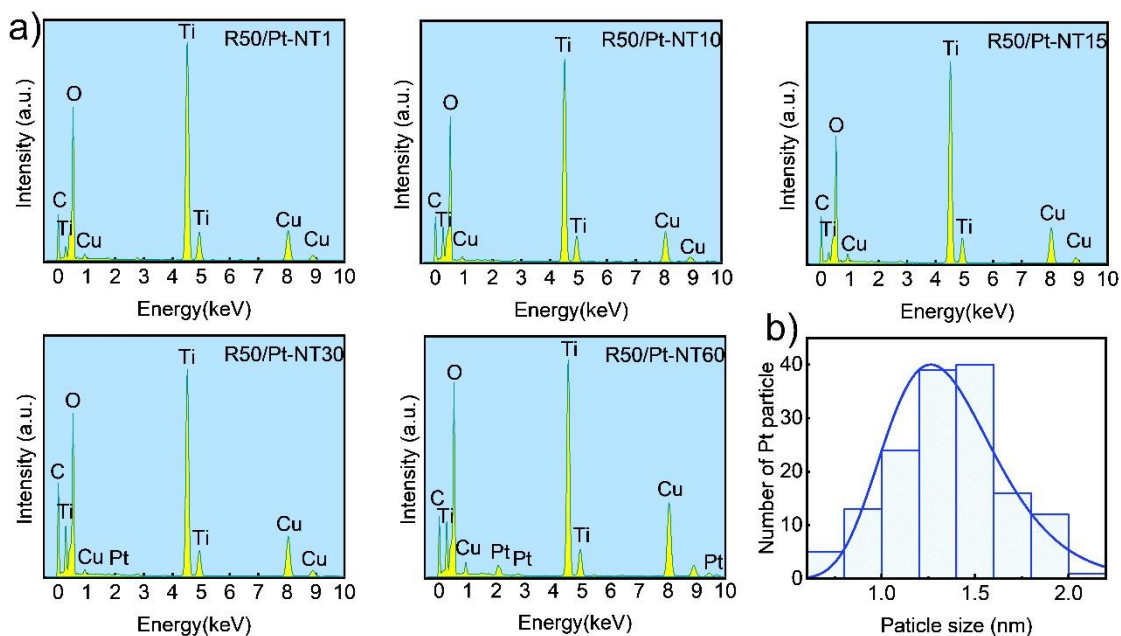


Figure 4.20 a) EDS analysis of Pt-SA and Pt-NP decorated on the TNTs and b) Pt nanoparticles size distribution on TNTs for R50/Pt-NT60 sample.

the relatively uniform distribution of those elements, including Pt single atoms and no contamination was observed.

To characterize the structure composition of the investigated samples, XPS analysis was carried out. The spectra of deposited Pt samples for different soaking time are illustrated in Figure 4.21a-c and Figure 4.22a-d. From the whole survey spectrum of treated samples, the elements of Ti, O, Pt and adventitious C can be observed (Figure 4.21a and Figure 4.22a) and the atomic ratio of Ti:O based on atomic composition of  $\text{TiO}_2$  is about 1:2. Deconvoluted HR-XPS spectra of the Pt4f region for the single-atoms (R50/Pt-NT10) and Pt nanoparticles decorated (R50/Pt-NT30) samples (emerging threshold of nanoparticles based on TEM image in Figure 4.19a) are shown in Figure 4.21b,c, respectively. Figure 4.21b shows that the XPS spectrum of Pt4f for the R50/Pt-NT10 sample (Pt-SA sample soaked 10 min in hexachloroplatinic acid solution) can be fitted into four peaks. The peaks appearing at 72.3 eV and 75.7 eV can be attributed to  $\text{Pt}^{2+}4f_{7/2}$  and  $\text{Pt}^{2+}4f_{5/2}$ , respectively, whereas the peaks at 73.2 eV and 76.5 eV assigned to  $\text{Pt}^{4+}4f_{7/2}$  and  $\text{Pt}^{4+}4f_{5/2}$  signals, correspondingly. By contrast, it can be observed from XPS in Figure 4.21c, for the sample by 30 min impregnation time in hexachloroplatinic acid solution (R50/Pt-NT30), the region corresponding to the Pt peak may be deconvoluted into three components ( $\text{Pt}^{2+}$ ,  $\text{Pt}^{4+}$  and  $\text{Pt}^0$ ). However, two peaks in metallic state located at 71.1 eV and 74.5 eV are corresponding to  $\text{Pt}^04f_{7/2}$  and  $\text{Pt}^04f_{5/2}$ , respectively [97,194,195]. These results are in good agreement with TEM results (Figure 4.19a) where the nanoparticles can be observed after 30 min impregnation time in hexachloroplatinic acid solution. The formation of  $\text{Pt}^{4+}$  coming from the covalent metals-support interaction is proof of a strong Pt- $\text{TiO}_2$  interaction [97,196]. The Pt-4O and Pt-2O structures are the most stable geometric and electronic configurations of Pt with O which are stable against the initial states of agglomeration [197]. Therefore, the atomic-scale deposition of single atom Pt on the sonicated TNTs surface (R50/Pt-NT10 sample) is confirmed. The HRXPS

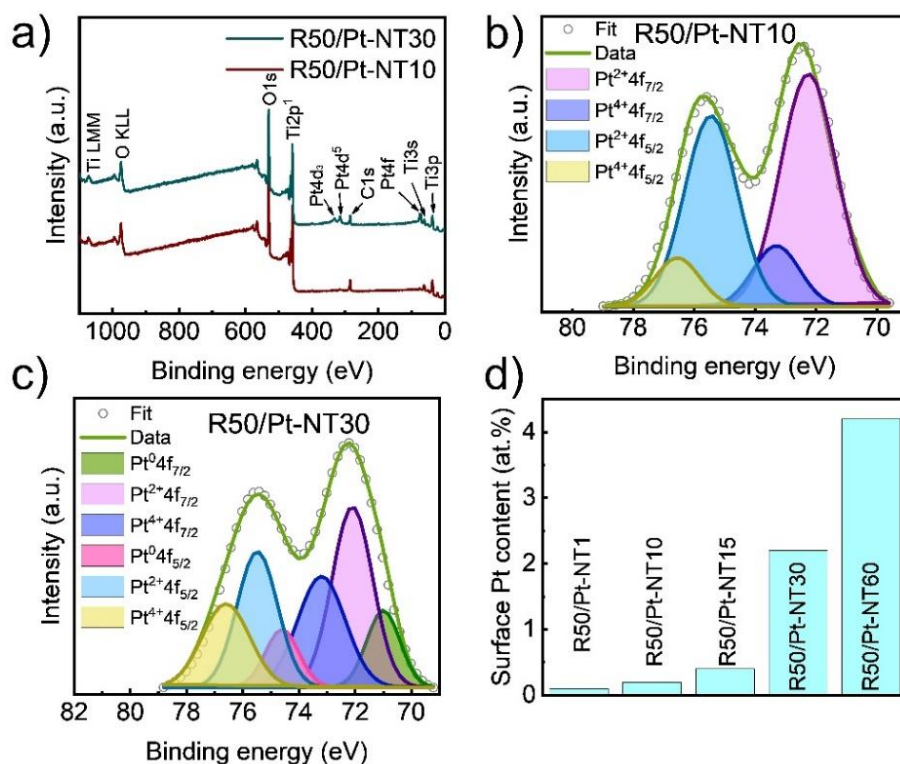


Figure 4.21 a) Whole XPS survey spectra of sonicated TNTs at different impregnation time (10 and 30 min) in in the hexachloroplatinic acid solution, b,c) HRXPS spectra of Pt4f for: b) sonicated TNTs for 50 min, followed by immersion in the hexachloroplatinic acid solution for 10 min, c) for 30 min and d) quantitative comparison of surface Pt on Pt-decorated TNTs.

analysis of the R50/Pt1-NT and R50/Pt-NT15 samples (Figure 4.22b.c) showed the presence of Pt in the oxidized state ( $Pt^{2+}$  and  $Pt^{4+}$ ). Moreover, the HRXPS spectra of Pt4f for these two samples (R50/Pt-NT1 and R50/Pt-NT15) is quite similar to the Pt4f peaks of R50/Pt-NT10 sample. The results demonstrate that these three samples are in the Pt-SA regime. In contrast, for the R50/Pt-NT60 sample, the Pt in the metallic state ( $Pt^0$ ) with peaks located at 70.2 eV and 73.5 eV are observed and can be assigned to  $Pt^0 4f_{7/2}$  and  $Pt^0 4f_{5/2}$ , respectively [198,199]. The XPS results of decorated samples with Pt are in line with the TEM images, confirming that the concentration of stabilized surface Pt is adjustable by increasing the soaking time in a diluted hexachloroplatinic acid solution. As the ICP-mass measurement for the film sample was very challenging to clarify the exact amount of the Pt on the TNTs film, XPS measurement was applied [97]. It was used to further evaluate the surface atomic concentration of Pt in the two forms of single atom

and nanoparticles, which were deposited onto the reduced TNTs successfully. The obtained results showed that increasing the soaking time in the hexachloroplatinic acid solution leads to an increase in the number of Pt deposited on the surface. As a result, the concentration of Pt in atomic-scale decoration for the R50/Pt-NT1, R50/Pt-NT10 and R50/Pt-NT15 samples is approximately 0.1, 0.2 and 0.4 at%, respectively. Whereas, based on XPS results, the amount of Pt in the form of nanoparticles for the R50/Pt-NT30, R50/Pt-NT60 samples are around 2.2 and 4.2 at%, respectively (Figure 4.21d). Interestingly, as shown in Figure 4.23 the peak area of  $\text{Ti}^{3+}$  removed after soaking the sonicated TNTs in the hexachloroplatinic acid solution. This can be as result of incorporation of Pt into the vacancies.

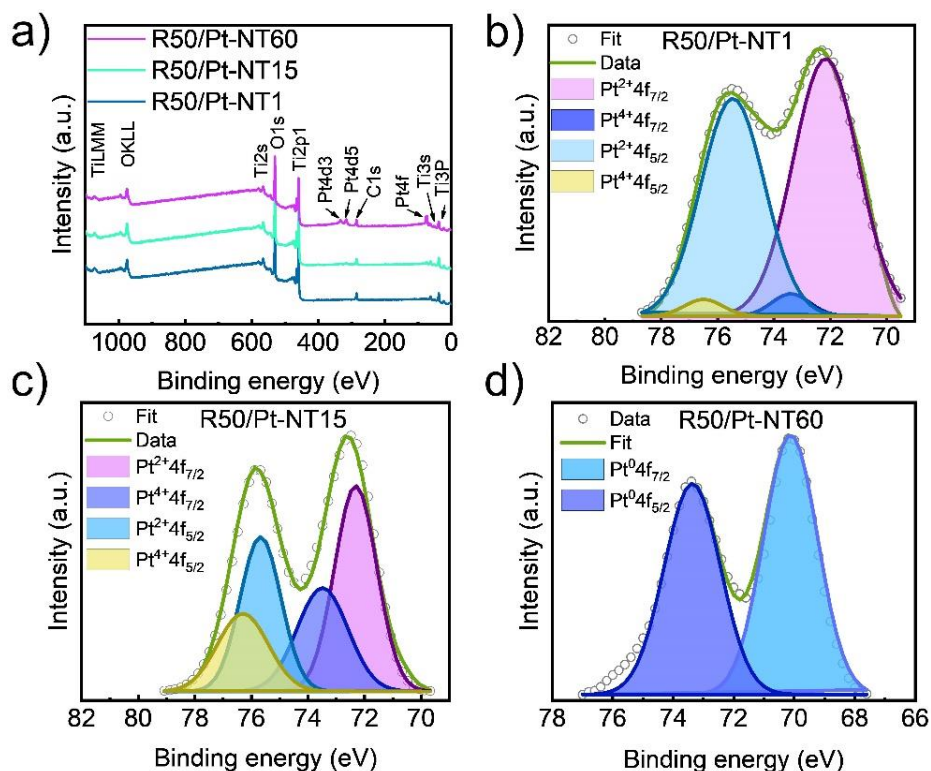


Figure 4.22 a) Whole XPS survey spectra of Pt decorated samples for different impregnation times in dilute hexachloroplatinic acid solution; b, c, d) HRXPS spectra in the Pt4f region of TNTs sonicated for 50 min, followed by immersion in the Pt solution for 1, 15 and 60 min (R50/Pt-NT1, R50/Pt-NT15 and R50/Pt-NT60), respectively.

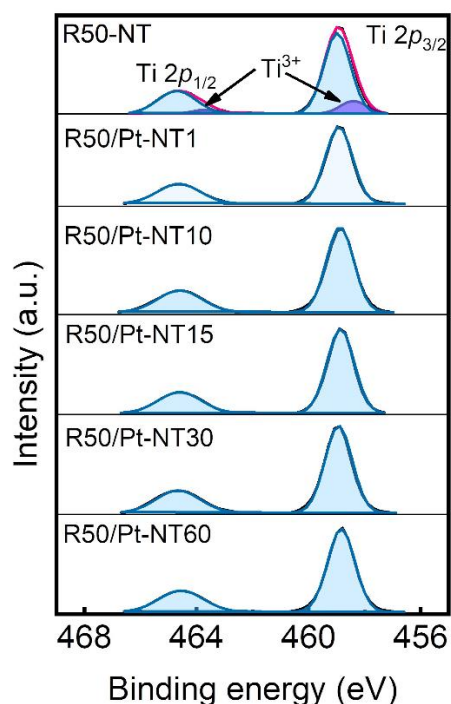


Figure 4.23 HRXPS spectra in the Ti2p region of sonicated TNTs for 50 min, followed by immersion in the Pt solution for 1, 10, 15, 30 and 60 min (R50/Pt-NT1, R50/Pt-NT10, R50/Pt-NT15, R50/Pt-NT30 and R50/Pt-NT60).

Figure 4.24 demonstrate the XRD pattern spectra for Pt-decorated samples. The results showed that anatase is only crystalline phase presents in the samples. Furthermore, no peak corresponding to Pt was detected in XRD results due to the small loading amount of Pt and highly dispersivity of metal in catalyst sample as well.

#### 4.4.4 Photocatalytic hydrogen evolution

To evaluate the photocatalytic H<sub>2</sub> production on platinized TNTs, the open circuit H<sub>2</sub> evolution was investigated in methanol-water solution using 1 sun solar simulator (AM 1.5 G-100 mW cm<sup>-2</sup>). Under light illumination, all the Pt-decorated TNTs demonstrated a higher amount of H<sub>2</sub> evolution compared to the pristine and sonicated TNTs without Pt (nearly 0.4 μl h<sup>-1</sup> cm<sup>-2</sup> for P-NT and R50-NT samples).

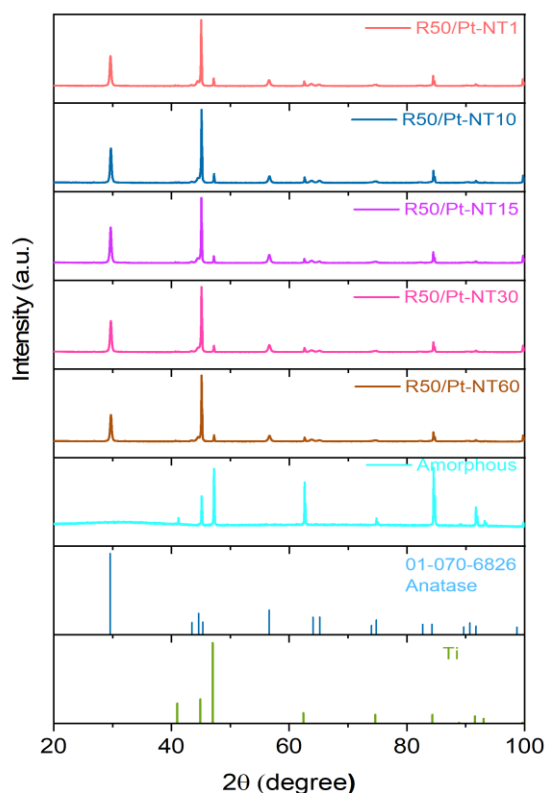


Figure 4.24 XRD pattern of Pt-SA and Pt-NP decorated samples.

In fact, the H<sub>2</sub> evolution of Pt-decorated samples (for the lowest amount of Pt in R50/Pt-NT1) is at least 10 times higher than the value obtained for pristine TNTs sample (P-NT). Likewise, because of the higher loading Pt on the surface of sonicated TNTs by increasing the impregnation time of sonicated samples in the dilute hexachloroplatinic acid solution, the H<sub>2</sub> evolution rate increased. The samples contain Pt-SA in shows less H<sub>2</sub> evolution rate in comparison with the samples with higher loading of Pt in nanoparticles (Figure 4.25a). However, normalization to the surface amount of Pt has done to show the influence of the Pt content on the H<sub>2</sub> evolution rate. Figure 4.25b compares the normalized H<sub>2</sub> evolution of Pt-decorated samples by the surface amount of Pt in two forms of SA and NP. The Pt-SA TNTs (R50/Pt-NT1, R50/Pt-NT10 and R50/Pt-NT15) demonstrated significantly higher amount of H<sub>2</sub> compared to the decorated TNTs with Pt-NP (R50/Pt-NT30 and R50/Pt-NT60), indicating the high effectiveness of photocatalytic activity of catalyst in atomic scale. Moreover, the efficiency of the active

catalytic centre could be explained as the turnover frequency (TOF) number. The TOF is calculated using Pt single atom density from HAADF-STEM image (Figure 4.19) and the evolved H<sub>2</sub>, showing significant value of  $2.9 \times 10^7 \text{ h}^{-1}$ . The reusability test of Pt-SA site on the sonicated TNTs surface demonstrated no obvious decrease of efficiency for H<sub>2</sub> production after five successive cycles of reuse, which indicated an impressive stability of synthesized catalyst. In addition, H<sub>2</sub> evolution was measured for better comparison of ultrasonication with traditional reduction method under like H<sub>2</sub> gas at high temperature. We compared the H<sub>2</sub> evolution rate of the highest active Pt-SA catalyst (R50/Pt-NT10) with the pristine and hydrogenated one at 450°C, followed by decoration with Pt in hexachloroplatinic acid solution for 10 min (P/Pt-NT10 and H/Pt-NT10 respectively) under 1 sun. The schematic illustration of the reaction of photocatalytic H<sub>2</sub> production through illumination of Pt SA-TiO<sub>2</sub> is shown in Figure 4.26. Photogenerated electrons-holes after absorption of the light by the TiO<sub>2</sub> can be separated into the conduction (CB) and valence (VB) bands, respectively. Pt plays an important role as the reductive co-catalyst reducing H<sup>+</sup> to H<sub>2</sub> while the methanol solution acts as a sacrificial reducing agent reacting with photo-generated holes as shown in Figure 4.26.

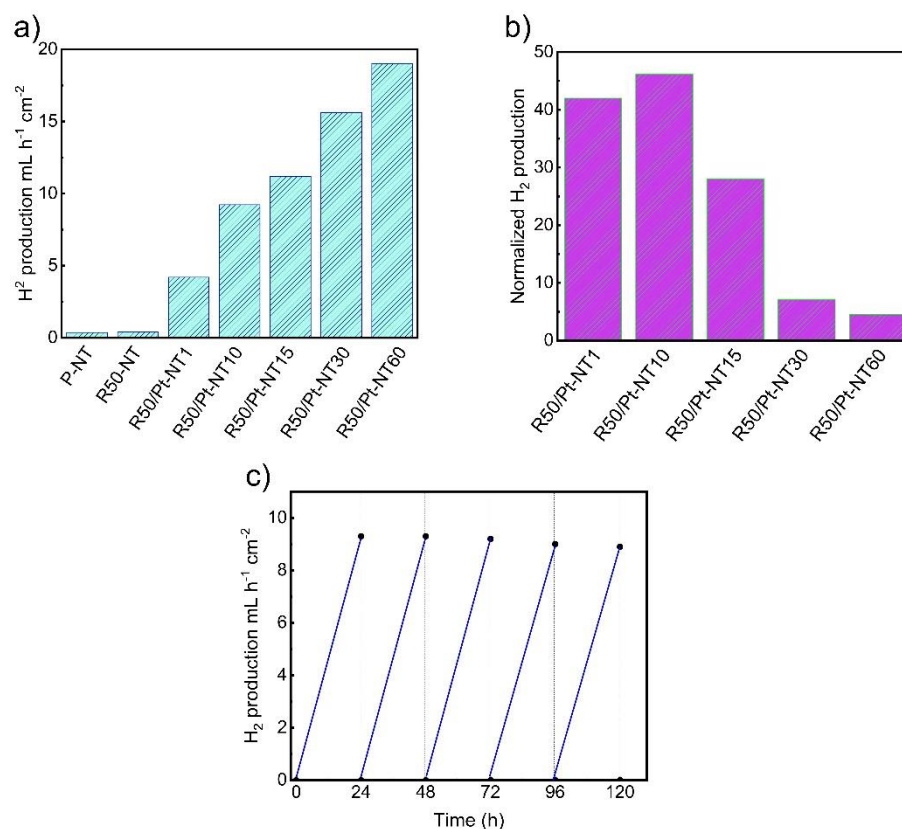


Figure 4.25 a) H<sub>2</sub> evolution of pristine, sonicated and Pt-decorated TNTs, b) Normalized H<sub>2</sub> evolution of Pt decorate sample, and c) reusability test of H<sub>2</sub> evolution of R50/Pt-NT10, sonicated for 50 min, followed by immersion in the hexachloroplatinic acid solution for 10 min

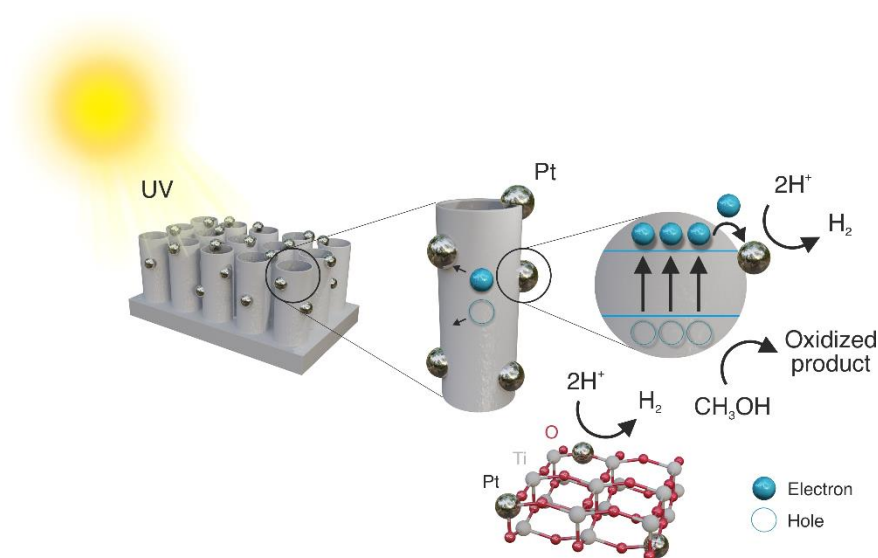


Figure 4.26 The mechanism of photocatalytic hydrogen evolution using ultrasound-reduced TNTs with embedded Pt single-atoms co-catalysts.

#### 4.4.5 Conclusion

In conclusion, we have shown for the first time, single atomic-scale Pt site on the defective TNTs arrays film using state-of-the-art technique to form lattice-defect on the surface of the substrate. Tip sonication set-up was employed under Ar atmosphere to form oxygen vacancy/ $\text{Ti}^{3+}$  state on the surface of TNTs, which were confirmed by HRXPS, UV-DRS measurement, and Mott-Schottky plot. Such defect can not only shift the maxima of the valence band of  $\text{TiO}_2$  upwards for band-gap narrowing but also some mid-gap defect might be formed. The outcomes showed that the impregnation time plays an important role to control Pt-SA decoration on the surface of TNTs. As a result, the ideal immersion duration resulted in the presence of Pt-SA atoms, as confirmed by the existence of  $\text{Pt}^{2+}$  and  $\text{Pt}^{4+}$  species. This configuration led to an approximately 10 fold increase in the photocatalytic  $\text{H}_2$  evolution rate compared to TNTs decorated with Pt nanoparticles. These outstanding results will most probably develop highly efficient SA-catalysts for the future.



## Chapter 5: Summary and Outlook

### 5.1 Summary

Within the scope of this doctoral dissertation, the formation of morphological and properties of TiO<sub>2</sub> NTs via anodization method on Ti foil were briefly investigated. Moreover, TiO<sub>2</sub> surface modification by platinized cyanographene as well as Pt single-atom decoration technique in order to decrease the usage of noble metal as co-catalysts in TiO<sub>2</sub> nanostructure were studied. The fabricated samples were characterized by different methods such as SEM, HRTEM, XRD, XPS, UV-vis DRS techniques to clarify the effect of the various treatments on structure of TiO<sub>2</sub> and consequently on its photocatalytic activity.

Through a systematic study of anodization parameters, the investigation delved into the effects of key variables, such as temperature, time, voltage, and electrolyte on the discrete-tube growth of TiO<sub>2</sub>. Among the different factors involved in the synthesis process, anodization temperature stands out as a key element with the potential to significantly influence the uniformity of tube formation. The establishment of a

heterojunction between the synthesized TiO<sub>2</sub> nanotubes and cyanographene (G-CN)/platinized cyanographene (G-CN/Pt) has been carried out. This step is crucial in creating a hybrid nanostructures that facilitates charge transfer and effective charge separation. The G-CN/MLTNTs and G-CN/Pt/MLTNTs composite improved the PEC-WS activity response by 1.66 and 1.25 times in comparison with pristine MLTNTs, respectively. Furthermore, by using various measurement techniques such as electrochemical impedance spectroscopy (EIS), open circuit VOC decay (VOCD), and intensity-modulated photocurrent spectroscopy (IMPS), the fabricated electrodes were investigate. The results indicate that surface functionalization of MLTNTs with G-CN and G-CN/Pt led to a reduction in the overall charge carrier recombination rate and transfer time of photogenerated electrons. Additionally, this functionalization resulted in an enhanced photoelectrochemical performance attributed to the decreased charge transfer resistance.

As a major breakthrough on noble metal usage as well as benefit from decoration of TNTs with it, the combination of a novel strategy for surface defect engineering and Pt single atom decoration has been presented. Through the reduction of an ideal metal oxide support using the ultrasonication method, atomic-scale defects can be generated. These defects then capture and stabilize Pt single atoms, achieved by employing a highly diluted hexachloroplatinic acid solution. The Pt content on the sonicated TNTs was regulated by adjusting the impregnation time in a diluted aqueous-based Pt solution. The high-resolution transmission electron microscopy (HRTEM) image further validates the presence of Pt single atoms (Pt-SA) on the surface of TNTs.

The innovative approach facilitates achieving almost 50 fold greater normalized hydrogen evolution in comparison to the unmodified TiO<sub>2</sub> nanotubes. Additionally, the newly established technique permits the incorporation of ultrasmall nanoparticles onto the TiO<sub>2</sub> surface by extending the substrate's exposure time to an extremely diluted

hexachloroplatinic acid solution. A comparison reveals that platinum single atoms yield a 10 fold increase in normalized hydrogen production compared to nanoparticles.

## 5.2 Outlook

This thesis work has focused on the enhancement of the photocatalytic activity of TiO<sub>2</sub> nanostructures. Specifically, enhancements were achieved through the introduction of novel materials like platinized cyanographene as well as single atom. Moreover, we investigated the TiO<sub>2</sub> nanostructure decorated with noble metal co-catalysts (Pt), which exhibited superior efficiency for photocatalytic H<sub>2</sub> evolution compared to nanoparticles. Therefore, investigating other noble metals in both single atom and nanoparticle forms for their photocatalytic activity is of merit. Innovatively, ultrasonication was utilized to introduce defect on TiO<sub>2</sub> nanotubes for anchoring Pt-single atom. However, a question arises regarding the applicability of ultrasonication for other semiconductors. Furthermore, other defective semiconductors might serve as suitable single atom hosts for photocatalytic reactions.

Concerning spaced TiO<sub>2</sub> NTs, further investigation is essential, and alternative strategies can be explored to synthesize longer tubes with controlled spacing. This has the potential to affect various applications of TiO<sub>2</sub> nanotubes, particularly in their photocatalytic activity. A prospective approach for discrete TiO<sub>2</sub> nanotubes involves enhancing photocatalytic H<sub>2</sub> evolution by extending the lifetime of photogenerated carriers. By depositing various materials on both sides of the fabricated TiO<sub>2</sub> nanotubes (interior and exterior), interactions with photoexcited charge carriers' electrons and holes can occur. Consequently, this approach can significantly reduce recombination rates, thereby boosting photocatalytic activity.



## References

- [1] M. Shahbaz, A. Sinha, C. Raghutla, X. Vinh, Decomposing scale and technique effects of financial development and foreign direct investment on renewable energy consumption, *Energy*. 238 (2022) 121758. doi:10.1016/j.energy.2021.121758.
- [2] Š. Kment, K. Sivula, A. Naldoni, S.P. Sarmah, H. Kmentová, M. Kulkarni, Y. Rambabu, P. Schmuki, R. Zboril, FeO-based nanostructures and nanohybrids for photoelectrochemical water splitting, *Prog. Mater. Sci.* 110 (2020) 100632. doi:10.1016/j.pmatsci.2019.100632.
- [3] S.E. Hosseini, M.A. Wahid, Hydrogen production from renewable and sustainable energy resources: Promising green energy carrier for clean development, *Renew. Sustain. Energy Rev.* 57 (2016) 850–866. doi:10.1016/j.rser.2015.12.112.
- [4] J. Mohtasham, Review Article-Renewable Energies, *Energy Procedia*. 74 (2015) 1289–1297. doi:10.1016/j.egypro.2015.07.774.
- [5] J. Barber, Photosynthetic energy conversion: Natural and artificial, *Chem. Soc. Rev.* 38 (2009) 185–196. doi:10.1039/b802262n.
- [6] C. Jiang, S.J.A. Moniz, A. Wang, T. Zhang, J. Tang, Photoelectrochemical devices for solar water splitting-materials and challenges, *Chem. Soc. Rev.* 46 (2017) 4645–4660. doi:10.1039/c6cs00306k.
- [7] M. Shahrezaei, S.M.H. Hejazi, Y. Rambabu, M. Vavrečka, A. Bakandritsos, S. Oezkan, R. Zboril, P. Schmuki, A. Naldoni, S. Kment, Multi-Leg TiO<sub>2</sub> Nanotube Photoelectrodes Modified by Platinized Cyanographene with Enhanced Photoelectrochemical Performance, *Catalysts*. 10 (2020) 717.
- [8] R.A.M. Ramachandran, R.K. Menon, AN OVERVIEW OF INDUSTRIAL USES OF HYDROGEN, *Int. J. Hydrog. Energy*. 23 (1998) 593–598.
- [9] A.P. Simpson, A.E. Lutz, Exergy analysis of hydrogen production via steam methane reforming, *Int. J. Hydrogen Energy*. 32 (2007) 4811–4820. doi:10.1016/j.ijhydene.2007.08.025.
- [10] L. Barelli, G. Bidini, F. Gallorini, S. Servili, Hydrogen production through sorption-enhanced steam methane reforming and membrane technology: A review, *Energy*. 33 (2008) 554–570. doi:10.1016/j.energy.2007.10.018.
- [11] S. Anwar, F. Khan, Y. Zhang, A. Djire, Recent development in electrocatalysts for hydrogen production through water electrolysis, *Int. J. Hydrogen Energy*. 46 (2021) 32284–32317. doi:10.1016/j.ijhydene.2021.06.191.
- [12] H. Zhang, G. Lin, J. Chen, Evaluation and calculation on the efficiency of a water electrolysis system for hydrogen production, *Int. J. Hydrogen Energy*. 35 (2010) 10851–10858. doi:10.1016/j.ijhydene.2010.07.088.
- [13] S. Zhu, D. Wang, Photocatalysis: Basic Principles , Diverse Forms of

- Implementations and Emerging Scientific Opportunities, *Adv. Energy Mater.* 7 (2017) 1700841. doi:10.1002/aenm.201700841.
- [14] X. Yang, D. Wang, Photocatalysis: From Fundamental Principles to Materials and Applications, *ACS Appl. Energy Mater.* 1 (2018) 6657–6693. doi:10.1021/acsaem.8b01345.
- [15] A. Albini, M. Fagnoni, 1908: Giacomo ciamician and the concept of green chemistry, *ChemSusChem*. 1 (2008) 63–66. doi:10.1002/cssc.200700015.
- [16] C. Baly, I.M. Heilbron, W.F. Barker, The Synthesis of Fmmaldehyde and Carbohydrates from Carbon Dioxide and Water, *J. Chem. Soc. Trans.* 119 (1921) 1025–1035.
- [17] L. Ji, M.D. Mcdaniel, S. Wang, A.B. Posadas, X. Li, H. Huang, J.C. Lee, A.A. Demkov, A.J. Bard, J.G. Ekerdt, E.T. Yu, A silicon-based photocathode for water reduction with an epitaxial SrTiO<sub>2</sub> protection layer and a nanostructured catalyst, *Nat. Nanotechnol.* 10 (2015) 84–90. doi:10.1038/nnano.2014.277.
- [18] X. Liu, C. Xu, L. Zhu, X. Wang, Molecular imprinting produces high photoelectric effect facilitating the efficient photocatalytic degradation of salicylic acid by TiO<sub>2</sub>, *React. Kinet. Mech. Catal.* 135 (2022) 529–537. doi:10.1007/s11144-021-02132-3.
- [19] Q. Yang, L. Yu, X. Zhao, Y. Wang, H. Zhu, Y. Zhang, Highly stable  $\gamma$ -NiOOH/ZnCdS photocatalyst for efficient hydrogen evolution, *Int. J. Hydrogen Energy.* 47 (2022) 27516–27526. doi:10.1016/j.ijhydene.2022.06.093.
- [20] X. Wang, L. Li, H. Gu, H. Zhang, J. Zhang, Q. Zhang, W.L. Dai, Highly efficient noble-metal-free NiS/rGO/Cd<sub>0.3</sub>Zn<sub>0.7</sub>S nanorods in visible-light-driven H<sub>2</sub> evolution with enhanced surface photoinduced charge transfer, *Appl. Surf. Sci.* 574 (2022) 151553. doi:10.1016/j.apsusc.2021.151553.
- [21] J.L. Bredas, Mind the gap!, *Mater. Horizons.* 1 (2014) 17–19. doi:10.1039/c3mh00098b.
- [22] J.A. Talla, Pressure induced phase transition and band gap controlling in defective graphene mono-sheet: Density functional theory, *Mater. Res. Express.* 6 (2019). doi:10.1088/2053-1591/ab4408.
- [23] M.E. Abdelhamid, A.P. O’Mullane, G.A. Snook, Storing energy in plastics: A review on conducting polymers & their role in electrochemical energy storage, *RSC Adv.* 5 (2015) 11611–11626. doi:10.1039/c4ra15947k.
- [24] M.B. Tahir, M. Sohaib, M. Sagir, M. Rafique, Role of Nanotechnology in Photocatalysis, *Encycl. Smart Mater.* (2021) 578–589. doi:10.1016/B978-0-12-815732-9.00006-1.
- [25] V. Etacheri, C. Di Valentin, J. Schneider, D. Bahnemann, S.C. Pillai, Visible-Light Activation of TiO<sub>2</sub> Photocatalysts: Advances in Theory and Experiments, *J. Photochem. Photobiol. C Photochem. Rev.* 25 (2015) 1–29. doi:10.1016/j.jphotochemrev.2015.08.003.
- [26] R. Acharya, B. Naik, K. Parida, Cr(VI) remediation from aqueous environment through modified-TiO<sub>2</sub>-mediated photocatalytic reduction, *Beilstein J. Nanotechnol.* 9 (2018) 1448–1470. doi:10.3762/bjnano.9.137.
- [27] T. Kawawaki, M. Kawachi, D. Yazaki, Y. Akinaga, D. Hirayama, Y. Negishi, Development and Functionalization of Visible-Light-Driven Water-Splitting Photocatalysts, *Nanomaterials.* 12 (2022) 344. doi:10.3390/nano12030344.
- [28] R.M. Navarro Yerga, M. Consuelo Álvarez Galván, F. del Valle, J.A. Villoria de la Mano, J.L.G. Fierro, Water splitting on semiconductor catalysts under visiblelight irradiation, *ChemSusChem.* 2 (2009) 471–485. doi:10.1002/cssc.200900018.
- [29] T. Banerjee, K. Gottschling, G. Savasci, C. Ochsenfeld, B. V. Lotsch, H<sub>2</sub> Evolution with Covalent Organic Framework Photocatalysts, *ACS Energy Lett.* 3 (2018)

- 400–409. doi:10.1021/acseenergylett.7b01123.
- [30] Y. Zhang, Y.J. Heo, J.W. Lee, J.H. Lee, J. Bajgai, K.J. Lee, S.J. Park, Photocatalytic hydrogen evolution via water splitting: A short review, *Catalysts*. 8 (2018) 655. doi:10.3390/catal8120655.
- [31] A.A. Ismail, D.W. Bahnemann, Photochemical splitting of water for hydrogen production by photocatalysis: A review, *Sol. Energy Mater. Sol. Cells*. 128 (2014) 85–101. doi:10.1016/j.solmat.2014.04.037.
- [32] R. Van De Krol, M. Gratzel, photoelectrochemical hydrogen production, 2011.
- [33] Z. Chen, H.N. Dinh, E. Miller, Photoelectrochemical water splitting: standards, experimental methods, and protocols, 2013. doi:10.1007/978-1-4614-8298-7.
- [34] J. Joy, J. Mathew, S.C. George, Nanomaterials for photoelectrochemical water splitting – review, *Int. J. Hydrogen Energy*. 43 (2018) 4804–4817. doi:10.1016/j.ijhydene.2018.01.099.
- [35] I. Roger, M.A. Shipman, M.D. Symes, Earth-abundant catalysts for electrochemical and photoelectrochemical water splitting, *Nat. Rev. Chem*. 1 (2017) 0003. doi:10.1038/s41570-016-0003.
- [36] W. Yang, R.R. Prabhakar, J. Tan, S.D. Tilley, J. Moon, Strategies for enhancing the photocurrent, photovoltage, and stability of photoelectrodes for photoelectrochemical water splitting, *Chem. Soc. Rev*. 48 (2019) 4979–5015. doi:10.1039/c8cs00997j.
- [37] T. Hisatomi, J. Kubota, K. Domen, Recent advances in semiconductors for photocatalytic and photoelectrochemical water splitting, *Chem. Soc. Rev*. 43 (2014) 7520–7535. doi:10.1039/c3cs60378d.
- [38] L.M. Peter, Photoelectrochemical Water Splitting. A Status Assessment, *Electroanalysis*. 27 (2015) 864–871. doi:10.1002/elan.201400587.
- [39] S. Wang, G. Liu, L. Wang, Crystal Facet Engineering of Photoelectrodes for Photoelectrochemical Water Splitting, *Chem. Rev*. 119 (2019) 5192–5247. doi:10.1021/acs.chemrev.8b00584.
- [40] K. Arifin, R.M. Yunus, L.J. Minggu, M.B. Kassim, Improvement of TiO<sub>2</sub> nanotubes for photoelectrochemical water splitting: Review, *Int. J. Hydrogen Energy*. 46 (2021) 4998–5024. doi:10.1016/j.ijhydene.2020.11.063.
- [41] C. Xia, T. Hong Chuong Nguyen, X. Cuong Nguyen, S. Young Kim, D.L.T. Nguyen, P. Raizada, P. Singh, V.H. Nguyen, C. Chien Nguyen, V. Chinh Hoang, Q. Van Le, Emerging cocatalysts in TiO<sub>2</sub>-based photocatalysts for light-driven catalytic hydrogen evolution: Progress and perspectives, *Fuel*. 307 (2022) 121745. doi:10.1016/j.fuel.2021.121745.
- [42] H. Lee, V.S. Kumbhar, J. Lee, H. Oh, K. Lee, Boosted photocatalytic hydrogen evolution by tuning inner pore size and co-catalyst thickness of the anodic TiO<sub>2</sub> nanotubes, *Catal. Today*. 359 (2021) 3–8. doi:10.1016/j.cattod.2019.03.066.
- [43] C. Chen, Y. Wei, G. Yuan, Q. Liu, R. Lu, X. Huang, Y. Cao, P. Zhu, Synergistic Effect of Si Doping and Heat Treatments Enhances the Photoelectrochemical Water Oxidation Performance of TiO<sub>2</sub> Nanorod Arrays, *Adv. Funct. Mater*. 27 (2017) 1–9. doi:10.1002/adfm.201701575.
- [44] A. Ishigaki, Y. Fukuda, *Kogyo Kagaku Zasshi, J. Soc. Chem. Ind. Japan*. 67 (1964) 509–513. doi:10.1246/nikkashi1898.67.2\_A17.
- [45] M. Shahrezaei, S. Habibzadeh, A.A. Babaluo, M. Haghghi, A. Hasanzadeh, R. Tahmasebpour, Study of synthesis parameters and photocatalytic activity of TiO<sub>2</sub> nanostructures, *J. Exp. Nanosci*. 12 (2017) 45–61. doi:10.1080/17458080.2016.1258495.
- [46] A.J. Haider, Z.N. Jameel, I.H.M. Al-Hussaini, Review on: Titanium dioxide applications, *Energy Procedia*. 157 (2019) 17–29. doi:10.1016/j.egypro.2018.11.159.

- [47] M.H. Samat, A.M.M. Ali, M.F.M. Taib, O.H. Hassan, M.Z.A. Yahya, Hubbard U calculations on optical properties of 3d transition metal oxide TiO<sub>2</sub>, *Results Phys.* 6 (2016) 891–896. doi:10.1016/j.rinp.2016.11.006.
- [48] J.F. Banfield, B.L. Bischoff, M.A. Anderson, TiO<sub>2</sub> accessory minerals: coarsening, and transformation kinetics in pure and doped synthetic nanocrystalline materials, *Chem. Geol.* 110 (1993) 211–231. doi:10.1016/0009-2541(93)90255-H.
- [49] D.A.H. Hanaor, C.C. Sorrell, Review of the anatase to rutile phase transformation, *J. Mater. Sci.* 46 (2011) 855–874. doi:10.1007/s10853-010-5113-0.
- [50] T.A. Kandiel, L. Robben, A. Alkaim, D. Bahnemann, Brookite versus anatase TiO<sub>2</sub> photocatalysts: Phase transformations and photocatalytic activities, *Photochem. Photobiol. Sci.* 12 (2013) 602–609. doi:10.1039/c2pp25217a.
- [51] K. Lee, A. Mazare, P. Schmuki, One-Dimensional Titanium Dioxide Nanomaterials: Nanotubes, *Chem. Rev.* 114 (2014) 9385–9454.
- [52] A.A. Ismail, T.A. Kandiel, D.W. Bahnemann, Novel (and better?) titania-based photocatalysts: Brookite nanorods and mesoporous structures, *J. Photochem. Photobiol. A Chem.* 216 (2010) 183–193. doi:10.1016/j.jphotochem.2010.05.016.
- [53] T.A. Kandiel, A. Feldhoff, L. Robben, R. Dillert, D.W. Bahnemann, Tailored titanium dioxide nanomaterials: anatase nanoparticles and brookite nanorods as highly active photocatalysts, *Chem. Mater.* 22 (2010) 2050–2060. doi:10.1021/cm903472p.
- [54] M. Addamo, M. Bellardita, A. Di Paola, L. Palmisano, Preparation and photoactivity of nanostructured anatase, rutile and brookite TiO<sub>2</sub> thin films, *Chem. Commun.* (2006) 4943–4945. doi:10.1039/b612172a.
- [55] L. Zhang, V.M. Menendez-Flores, N. Murakami, T. Ohno, Improvement of photocatalytic activity of brookite titanium dioxide nanorods by surface modification using chemical etching, *Appl. Surf. Sci.* 258 (2012) 5803–5809. doi:10.1016/j.apsusc.2012.02.103.
- [56] X. Chen, S.S. Mao, Titanium dioxide nanomaterials: Synthesis, properties, modifications and applications, *Chem. Rev.* 107 (2007) 2891–2959. doi:10.1021/cr0500535.
- [57] L. Kavan, M. Grätzel, S.E. Gilbert, C. Klemenz, H.J. Scheel, Electrochemical and photoelectrochemical investigation of single-crystal anatase, *J. Am. Chem. Soc.* 118 (1996) 6716–6723. doi:10.1021/ja954172l.
- [58] U. Diebold, The surface science of titanium dioxide, *Surf. Sci. Rep.* 48 (2003) 53–229. <http://linkinghub.elsevier.com/retrieve/pii/S0167572902001000>.
- [59] M. Ge, C. Cao, J. Huang, S. Li, Z. Chen, K. Zhang, S.S. Al-Deyab, Y. Lai, A Review of One-dimensional TiO<sub>2</sub> Nanostructured Materials for Environmental and Energy Applications, *J. Mater. Chem. A.* (2013) 1–26. doi:10.1039/x0xx00000x.
- [60] M. Shahrezaei, S. Habibzadeh, A.A. Babaluo, H. Hosseinkhani, M. Haghighi, A. Hasanzadeh, R. Tahmasebpour, Study of synthesis parameters and photocatalytic activity of TiO<sub>2</sub> nanostructures, *J. Exp. Nanosci.* 12 (2017) 45–61. doi:10.1080/17458080.2016.1258495.
- [61] J. Tian, Z. Zhao, A. Kumar, R.I. Boughton, H. Liu, Recent progress in design, synthesis, and applications of one-dimensional TiO<sub>2</sub> nanostructured surface heterostructures: A review, *Chem. Soc. Rev.* 43 (2014) 6920–6937. doi:10.1039/c4cs00180j.
- [62] M. Qamar, C.R. Yoon, H.J. Oh, A. Czoska, K. Park, N.H. Lee, K.S. Lee, S.J. Kim, Preparation of Titanium Oxide Nanotube by Hydrothermal Process, *Solid State Phenom.* 124–126 (2007) 1165–1168. doi:10.4028/www.scientific.net/ssp.124-126.1165.
- [63] T. Gupta, Samriti, J. Cho, J. Prakash, Hydrothermal synthesis of TiO<sub>2</sub> nanorods: formation chemistry, growth mechanism, and tailoring of surface properties for

- photocatalytic activities, *Mater. Today Chem.* 20 (2021) 100428. doi:10.1016/j.mtchem.2021.100428.
- [64] V. Zwillig, M. Aucouturier, E. Darque-Ceretti, Anodic oxidation of titanium and TA6V alloy in chromic media. An electrochemical approach, *Electrochim. Acta.* 45 (1999) 921–929. doi:10.1016/S0013-4686(99)00283-2.
- [65] D. Gong, C.A. Grimes, O.K. Varghese, W. Hu, R.S. Singh, Z. Chen, E.C. Dickey, Titanium oxide nanotube arrays prepared by anodic oxidation, *J. Mater. Res.* 16 (2001) 3331–3334. doi:10.1557/JMR.2001.0457.
- [66] B.M. Rao, A. Torabi, O.K. Varghese, Anodically grown functional oxide nanotubes and applications, *MRS Commun.* 6 (2016) 375–396. doi:10.1557/mrc.2016.46.
- [67] T.M. David, P.R. Dev, P. Wilson, P. Sagayaraj, T. Mathews, A critical review on the variations in anodization parameters toward microstructural formation of TiO<sub>2</sub> nanotubes, *Electrochem. Sci. Adv.* (2021) e202100083. doi:10.1002/elsa.202100083.
- [68] Y. Fu, A. Mo, A Review on the Electrochemically Self-organized Titania Nanotube Arrays: Synthesis, Modifications, and Biomedical Applications, *Nanoscale Res. Lett.* 13 (2018) 187. doi:10.1186/s11671-018-2597-z.
- [69] X.C. Dai, S. Hou, M.H. Huang, Y.B. Li, T. Li, F.X. Xiao, Electrochemically anodized one-dimensional semiconductors: A fruitful platform for solar energy conversion, *JPhys Energy.* 1 (2019). doi:10.1088/2515-7655/ab0718.
- [70] P. Roy, S. Berger, P. Schmuki, TiO<sub>2</sub> Nanotubes: Synthesis and Applications, *Angew. Chem. Int. Ed.* 50 (2011) 2904–2939. doi:10.1002/anie.201001374.
- [71] J.M. Macak, H. Tsuchiya, A. Ghicov, K. Yasuda, R. Hahn, S. Bauer, P. Schmuki, TiO<sub>2</sub> nanotubes: Self-organized electrochemical formation, properties and applications, *Curr. Opin. Solid State Mater. Sci.* 11 (2007) 3–18. doi:10.1016/j.cossms.2007.08.004.
- [72] D. Regonini, C.R. Bowen, A. Jaroenworarluck, R. Stevens, A review of growth mechanism, structure and crystallinity of anodized TiO<sub>2</sub> nanotubes, *Mater. Sci. Eng. R Reports.* 74 (2013) 377–406. doi:10.1016/j.mser.2013.10.001.
- [73] K. Indira, U.K. Mudali, T. Nishimura, N. Rajendran, A Review on TiO<sub>2</sub> Nanotubes: Influence of Anodization Parameters, Formation Mechanism, Properties, Corrosion Behavior, and Biomedical Applications, *J. Bio- Tribo-Corrosion.* 1 (2015) 1–22. doi:10.1007/s40735-015-0024-x.
- [74] C. Dette, M.A. Pérez-Osorio, C.S. Kley, P. Punke, C.E. Patrick, P. Jacobson, F. Giustino, S.J. Jung, K. Kern, TiO<sub>2</sub> anatase with a bandgap in the visible region, *Nano Lett.* 14 (2014) 6533–6538. doi:10.1021/nl503131s.
- [75] X. Kang, S. Liu, Z. Dai, Y. He, X. Song, Z. Tan, Titanium dioxide: From engineering to applications, 2019. doi:10.3390/catal9020191.
- [76] A. Mittal, B. Mari, S. Sharma, V. Kumari, S. Maken, K. Kumari, N. Kumar, Non-metal modified TiO<sub>2</sub>: a step towards visible light photocatalysis, *J. Mater. Sci. Mater. Electron.* 30 (2019) 3186–3207. doi:10.1007/s10854-018-00651-9.
- [77] P.S. Basavarajappa, S.B. Patil, N. Ganganagappa, K.R. Reddy, A. V. Raghu, C.V. Reddy, Recent progress in metal-doped TiO<sub>2</sub>, non-metal doped/codoped TiO<sub>2</sub> and TiO<sub>2</sub> nanostructured hybrids for enhanced photocatalysis, *Int. J. Hydrogen Energy.* 45 (2020) 7764–7778. doi:10.1016/j.ijhydene.2019.07.241.
- [78] S.Z. Islam, S. Nagpure, D.Y. Kim, S.E. Rankin, Synthesis and catalytic applications of non-metal doped mesoporous titania, *Inorganics.* 5 (2017) 1–43. doi:10.3390/inorganics5010015.
- [79] S.N.A. Sulaiman, M. Zaky Noh, N. Nadia Adnan, N. Bidin, S.N. Ab Razak, Effects of photocatalytic activity of metal and non-metal doped TiO<sub>2</sub> for Hydrogen production enhancement - A Review, *J. Phys. Conf. Ser.* 1027 (2018) 012006.

- doi:10.1088/1742-6596/1027/1/012006.
- [80] A. Piątkowska, M. Janus, K. Szymański, S. Mozia, C-,n-and s-doped TiO<sub>2</sub> photocatalysts: A review, *Catalysts*. 11 (2021) 1–56. doi:10.3390/catal11010144.
- [81] X. Chen, S. Shen, L. Guo, S.S. Mao, Semiconductor-based photocatalytic hydrogen generation, *Chem. Rev.* 110 (2010) 6503–6570. doi:10.1021/cr1001645.
- [82] K. Siuzdak, M. Szkoda, M. Sawczak, A. Lisowska-Oleksiak, Novel nitrogen precursors for electrochemically driven doping of titania nanotubes exhibiting enhanced photoactivity, *New J. Chem.* 39 (2015) 2741–2751. doi:10.1039/c5nj00127g.
- [83] M. Ge, Q. Li, C. Cao, J. Huang, S. Li, S. Zhang, Z. Chen, K. Zhang, S.S. Al-Deyab, Y. Lai, One-dimensional TiO<sub>2</sub> Nanotube Photocatalysts for Solar Water Splitting, *Adv. Sci.* 4 (2017) 1600152. doi:10.1002/advs.201600152.
- [84] A.S. Mestre, A.P. Carvalho, Photocatalytic Degradation of Pharmaceuticals Carbamazepine, Diclofenac, and Sulfamethoxazole by Semiconductor and Carbon Materials: A Review, *Molecules*. 24 (2019) 3702. <https://www.mdpi.com/1420-3049/24/20/3702/pdf>.
- [85] X. Zhao, G. Zhang, Z. Zhang, TiO<sub>2</sub>-based catalysts for photocatalytic reduction of aqueous oxyanions: State-of-the-art and future prospects, *Environ. Int.* 136 (2020) 105453. doi:10.1016/j.envint.2019.105453.
- [86] V. Kumaravel, S. Mathew, J. Bartlett, S.C. Pillai, Photocatalytic hydrogen production using metal doped TiO<sub>2</sub>: A review of recent advances, *Appl. Catal. B Environ.* 244 (2019) 1021–1064. doi:10.1016/j.apcatb.2018.11.080.
- [87] N.S. Ibrahim, W.L. Leaw, D. Mohamad, S.H. Alias, H. Nur, A critical review of metal-doped TiO<sub>2</sub> and its structure–physical properties–photocatalytic activity relationship in hydrogen production, *Int. J. Hydrogen Energy*. 45 (2020) 28553–28565. doi:10.1016/j.ijhydene.2020.07.233.
- [88] M. Ismael, A review and recent advances in solar-to-hydrogen energy conversion based on photocatalytic water splitting over doped-TiO<sub>2</sub> nanoparticles, *Sol. Energy*. 211 (2020) 522–546. doi:10.1016/j.solener.2020.09.073.
- [89] Z. Zafar, S. Yi, J. Li, C. Li, Y. Zhu, A. Zada, W. Yao, Z. Liu, X. Yue, Recent Development in Defects Engineered Photocatalysts: An Overview of the Experimental and Theoretical Strategies, *Energy Environ. Mater.* 5 (2022) 68–114. doi:10.1002/eem2.12171.
- [90] Y. Wang, Q. Wang, X. Zhan, F. Wang, M. Safdar, J. He, Visible light driven type II heterostructures and their enhanced photocatalysis properties: A review, *Nanoscale*. 5 (2013) 8326–8339. doi:10.1039/c3nr01577g.
- [91] J. Yang, H. Yan, X. Zong, Fuyuwen, M. Liu, C. Li, Roles of cocatalysts in semiconductor-based photocatalytic hydrogen production, *Philos. Trans. R. Soc. A Math. Phys. Eng. Sci.* 371 (2013). doi:10.1098/rsta.2011.0430.
- [92] B. Łosiewicz, M. Popczyk, I. Napłoszek, A. Budniok, Intermetallic compounds as catalysts in the reaction of electroevolution/absorption of hydrogen, *Solid State Phenom.* 228 (2015) 16–22. doi:10.4028/www.scientific.net/SSP.228.16.
- [93] C. Li, J.B. Baek, Recent Advances in Noble Metal (Pt, Ru, and Ir)-Based Electrocatalysts for Efficient Hydrogen Evolution Reaction, *ACS Omega*. 5 (2020) 31–40. doi:10.1021/acsomega.9b03550.
- [94] L. Li, X. Chang, X. Lin, Z.J. Zhao, J. Gong, Theoretical insights into single-atom catalysts, *Chem. Soc. Rev.* 49 (2020) 8156–8178. doi:10.1039/d0cs00795a.
- [95] M. Yang, S. Li, Y. Wang, J.A. Herron, Y. Xu, L.F. Allard, S. Lee, J. Huang, M. Mavrikakis, M. Flytzani-Stephanopoulos, Catalytically active Au-O(OH)<sub>x</sub>- species stabilized by alkali ions on zeolites and mesoporous oxides, *Science*. 346 (2014) 1498–1502.
- [96] B. Qiao, A. Wang, X. Yang, L.F. Allard, Z. Jiang, Y. Cui, J. Liu, J. Li, T. Zhang,

- Single-atom catalysis of CO oxidation using Pt<sub>1</sub>/FeO<sub>x</sub>, *Nat. Chem.* 3 (2011) 634–641. doi:10.1038/nchem.1095.
- [97] S. Hejazi, S. Mohajernia, B. Osuagwu, G. Zoppellaro, P. Andryskova, O. Tomanec, S. Kment, R. Zboril, P. Schmuki, On the Controlled Loading of Single Platinum Atoms as a Co-Catalyst on TiO<sub>2</sub> Anatase for Optimized Photocatalytic H<sub>2</sub> Generation, *Adv. Mater.* 32 (2020) 1908505. doi:10.1002/adma.201908505.
- [98] X. Yang, A. Wang, B. Qiao, J.U.N. Li, J. Liu, T. Zhang, Single-Atom Catalysts: A New Frontier in Heterogeneous Catalysis, *Acc. Chem. Res.* 46 (2013) 1740–1748.
- [99] A.-W. Zhou, D.-S. Wang, Y.-D. Li, Hollow microstructural regulation of single-atom catalysts for optimized electrocatalytic performance, *Microstructures.* 2 (2022) 022005. doi:10.20517/microstructures.2021.08.
- [100] H. Yan, H. Cheng, H. Yi, Y. Lin, T. Yao, C. Wang, J. Li, S. Wei, J. Lu, Single-Atom Pd 1/Graphene Catalyst Achieved by Atomic Layer Deposition: Remarkable Performance in Selective Hydrogenation of 1,3-Butadiene, *J. Am. Chem. Soc.* 137 (2015) 10484–10487. doi:10.1021/jacs.5b06485.
- [101] S. Sun, G. Zhang, N. Gauquelin, N. Chen, J. Zhou, S. Yang, W. Chen, X. Meng, D. Geng, M.N. Banis, R. Li, S. Ye, S. Knights, G.A. Botton, T. Sham, X. Sun, Single-atom Catalysis Using Pt/Graphene Achieved through Atomic Layer Deposition, *Sci. Rep.* 3 (2013) 1775. doi:10.1038/srep01775.
- [102] J. Lin, B. Qiao, J. Liu, Y. Huang, A. Wang, L. Li, W. Zhang, L.F. Allard, X. Wang, T. Zhang, Design of a Highly Active Ir/Fe(OH)<sub>x</sub> Catalyst: Versatile Application of Pt-Group Metals for the Preferential Oxidation of Carbon Monoxide, *Angew. Chem. Int. Ed.* 51 (2012) 2920–2924. doi:10.1002/anie.201106702.
- [103] P. Liu, Y. Zhao, R. Qin, S. Mo, G. Chen, L. Gu, D.M. Chevrier, P. Zhang, Q. Guo, D. Zang, B. Wu, G. Fu, N. Zheng, Photochemical route for synthesizing atomically dispersed palladium catalysts, *Science.* 352 (2016) 797–800.
- [104] D.C. Marcano, D. V Kosynkin, J.M. Berlin, A. Sinitskii, Z. Sun, A. Slesarev, L.B. Alemany, W. Lu, J.M. Tour, Improved Synthesis of Graphene Oxide, *ACS Nano.* 4 (2010) 4806–4814. doi:10.1021/nn1006368.
- [105] J. Lu, C. Aydin, N.D. Browning, B.C. Gates, Imaging Isolated Gold Atom Catalytic Sites in Zeolite NaY, *Angew. Chem. Int. Ed.* 51 (2012) 5842–5846. doi:10.1002/anie.201107391.
- [106] H. Zhang, J. Wei, J. Dong, G. Liu, L. Shi, P. An, G. Zhao, J. Kong, X. Wang, X. Meng, J. Zhang, J. Ye, Efficient Visible-Light-Driven Carbon Dioxide Reduction by a Single-Atom Implanted Metal – Organic Framework, *Angew. Chem. Int. Ed.* 55 (2016) 14310–14314. doi:10.1002/anie.201608597.
- [107] T. He, S. Chen, B. Ni, Y. Gong, Z. Wu, L. Song, L. Gu, W. Hu, X. Wang, Zirconium–Porphyrin-Based Metal–Organic Framework Hollow Nanotubes for Immobilization of Noble-Metal Single Atoms, *Angew. Chem. Int. Ed.* 57 (2018) 3493–3498. doi:10.1002/anie.201800817.
- [108] H. Zhang, G. Liu, L. Shi, J. Ye, Single-Atom Catalysts: Emerging Multifunctional Materials in Heterogeneous Catalysis, *Adv. Energy Mater.* (2017) 1701343. doi:10.1002/aenm.201701343.
- [109] J. Li, H. Huang, P. Liu, X. Song, D. Mei, Y. Tang, X. Wang, C. Zhong, Metal-organic framework encapsulated single-atom Pt catalysts for efficient photocatalytic hydrogen evolution, *J. Catal.* 375 (2019) 351–360. doi:10.1016/j.jcat.2019.06.024.
- [110] R. Lang, X. Du, Y. Huang, X. Jiang, Q. Zhang, Y. Guo, K. Liu, B. Qiao, A. Wang, T. Zhang, Single-Atom Catalysts Based on the Metal-Oxide Interaction, *Chem. Rev.* 120 (2020) 11986–12043. doi:10.1021/acs.chemrev.0c00797.
- [111] L. Yao, W. Wang, Y. Liang, J. Fu, H. Shi, Plasmon-enhanced visible light

- photoelectrochemical and photocatalytic activity of gold nanoparticle-decorated hierarchical TiO<sub>2</sub>/Bi<sub>2</sub>WO<sub>6</sub> nanorod arrays, *Appl. Surf. Sci.* 469 (2019) 829–840. doi:10.1016/j.apsusc.2018.11.031.
- [112] J. Cai, X. Wu, S. Li, F. Zheng, L. Zhu, Z. Lai, Synergistic effect of double-shelled and sandwiched TiO<sub>2</sub>@Au@C hollow spheres with enhanced visible-light-driven photocatalytic activity, *ACS Appl. Mater. Interfaces.* 7 (2015) 3764–3772. doi:10.1021/am508554t.
- [113] W. Hou, S.B. Cronin, A review of surface plasmon resonance-enhanced photocatalysis, *Adv. Funct. Mater.* 23 (2013) 1612–1619. doi:10.1002/adfm.201202148.
- [114] Y. Sang, H. Liu, A. Umar, Photocatalysis from UV Vis to Near-Infrared Light Towards Full Solar-Light Spectrum Activity, *ChemCatChem* 2015, 7 (2015) 559–573.
- [115] K. Marchuk, K.A. Willets, Localized surface plasmons and hot electrons, *Chem. Phys.* 445 (2014) 95–104. doi:10.1016/j.chemphys.2014.10.016.
- [116] T. Tatsuma, H. Nishi, T. Ishida, Plasmon-induced charge separation: Chemistry and wide applications, *Chem. Sci.* 8 (2017) 3325–3337. doi:10.1039/c7sc00031f.
- [117] Q. Zhang, T. Gao, J.M. Andino, Y. Li, Copper and iodine co-modified TiO<sub>2</sub> nanoparticles for improved activity of CO<sub>2</sub> photoreduction with water vapor, *Appl. Catal. B Environ.* 123–124 (2012) 257–264. doi:10.1016/j.apcatb.2012.04.035.
- [118] X. Wu, S. Yin, Q. Dong, C. Guo, T. Kimura, J.I. Matsushita, T. Sato, Photocatalytic properties of Nd and C Codoped TiO<sub>2</sub> with the Whole range of visible light absorption, *J. Phys. Chem. C.* 117 (2013) 8345–8352. doi:10.1021/jp402063n.
- [119] H. Zhang, Y. Liang, X. Wu, H. Zheng, Enhanced photocatalytic activity of (Zn, N)-codoped TiO<sub>2</sub> nanoparticles, *Mater. Res. Bull.* 47 (2012) 2188–2192. doi:10.1016/j.materresbull.2012.06.008.
- [120] J. Zhang, J. Xi, Z. Ji, Mo + N Codoped TiO<sub>2</sub> sheets with dominant {001} facets for enhancing visible-light photocatalytic activity, *J. Mater. Chem.* 22 (2012) 17700–17708. doi:10.1039/c2jm32391e.
- [121] X. Chen, L. Liu, P.Y. Yu, S.S. Mao, Increasing solar absorption for photocatalysis with black hydrogenated titanium dioxide nanocrystals, *Science* 331 (2011) 746–750. doi:10.1126/science.1200448.
- [122] H. Li, J. Li, Z. Ai, F. Jia, L. Zhang, Oxygen Vacancy-Mediated Photocatalysis of BiOCl: Reactivity, Selectivity, and Perspectives, *Angew. Chemie - Int. Ed.* 57 (2018) 122–138. doi:10.1002/anie.201705628.
- [123] J. Nowotny, M.A. Alim, T. Bak, M.A. Idris, M. Ionescu, K. Prince, M.Z. Sahdan, K. Sopian, M.A. Mat Teridi, W. Sigmund, Defect chemistry and defect engineering of TiO<sub>2</sub>-based semiconductors for solar energy conversion, *Chem. Soc. Rev.* 44 (2015) 8424–8442. doi:10.1039/c4cs00469h.
- [124] A. Naldoni, M. Altomare, G. Zoppellaro, N. Liu, Š. Kment, R. Zbořil, P. Schmuki, Photocatalysis with reduced TiO<sub>2</sub>: From Black TiO<sub>2</sub> to cocatalyst-free hydrogen production, *ACS Catal.* 9 (2019) 345–364. doi:10.1021/acscatal.8b04068.
- [125] A. Naldoni, M. Allietta, S. Santangelo, M. Marelli, F. Fabbri, S. Cappelli, C.L. Bianchi, R. Psaro, V. Dal Santo, Effect of nature and location of defects on bandgap narrowing in black TiO<sub>2</sub> nanoparticles, *J. Am. Chem. Soc.* 134 (2012) 7600–7603. doi:10.1021/ja3012676.
- [126] X. Chen, C. Burda, The electronic origin of the visible-light absorption properties of C-, N- and S-doped TiO<sub>2</sub> nanomaterials, *J. Am. Chem. Soc.* 130 (2008) 5018–5019. doi:10.1021/ja711023z.
- [127] R.L. Penn, J.F. Banfield, Formation of rutile nuclei at anatase {112} twin interfaces and the phase transformation mechanism in nanocrystalline titania, *Am. Mineral.*

- 84 (1999) 871–876. doi:10.2138/am-1999-5-621.
- [128] M. Liu, D. Jing, Z. Zhou, L. Guo, Twin-induced one-dimensional homojunctions yield high quantum efficiency for solar hydrogen generation, *Nat. Commun.* 4 (2013) 2278. doi:10.1038/ncomms3278.
- [129] Y.H. Hu, A highly efficient photocatalyst-hydrogenated black TiO<sub>2</sub> for the photocatalytic splitting of water, *Angew. Chemie - Int. Ed.* 51 (2012) 12410–12412. doi:10.1002/anie.201206375.
- [130] M. Janczarek, E. Kowalska, Defective dopant-free TiO<sub>2</sub> as an efficient visible light-active photocatalyst, *Catalysts*. 11 (2021) 978. doi:10.3390/catal11080978.
- [131] J. Mu, E. Spiecker, P. Schmuki, Black TiO<sub>2</sub> Nanotubes: Cocatalyst-Free Open-Circuit Hydrogen Generation, *Nano Lett.* 14 (2014) 3309–3313.
- [132] C. Xu, Y. Song, L. Lu, C. Cheng, D. Liu, X. Fang, X. Chen, X. Zhu, D. Li, Electrochemically hydrogenated TiO<sub>2</sub> nanotubes with improved photoelectrochemical water splitting performance, *Nanoscale Res. Lett.* 8 (2013) 1–7. doi:10.1186/1556-276X-8-391.
- [133] Z. Zhang, M.N. Hedhili, H. Zhu, P. Wang, Electrochemical reduction induced self-doping of Ti<sup>3+</sup> for efficient water splitting performance on TiO<sub>2</sub> based photoelectrodes, *Phys. Chem. Chem. Phys.* 15 (2013) 15637–15644. doi:10.1039/c3cp52759j.
- [134] L. Zheng, H. Cheng, F. Liang, S. Shu, C.K. Tsang, H. Li, S.T. Lee, Y.Y. Li, Porous TiO<sub>2</sub> photonic band gap materials by anodization, *J. Phys. Chem. C*. 116 (2012) 5509–5515. doi:10.1021/jp212416c.
- [135] H. Zhou, Y. Zhang, Electrochemically Self-Doped TiO<sub>2</sub> Nanotube Arrays for Supercapacitors, *J. Phys. Chem. C*. 118 (2014) 5626–5696.
- [136] H. Li, Z. Chen, C.K. Tsang, Z. Li, X. Ran, C. Lee, B. Nie, L. Zheng, T. Hung, J. Lu, B. Pan, Y.Y. Li, Electrochemical doping of anatase TiO<sub>2</sub> in organic electrolytes for high-performance supercapacitors and photocatalysts, *J. Mater. Chem. A*. 2 (2014) 229–236. doi:10.1039/c3ta13963h.
- [137] Z. Wang, C. Yang, T. Lin, H. Yin, P. Chen, D. Wan, F. Xu, F. Huang, J. Lin, X. Xie, M. Jiang, Visible-light photocatalytic, solar thermal and photoelectrochemical properties of aluminium-reduced black titania, *Energy Environ. Sci.* 6 (2013) 3007–3014. doi:10.1039/c3ee41817k.
- [138] H. Cui, W. Zhao, C. Yang, H. Yin, T. Lin, Y. Shan, Y. Xie, H. Gu, F. Huang, Black TiO<sub>2</sub> nanotube arrays for high-efficiency photoelectrochemical water-splitting, *J. Mater. Chem. A*. 2 (2014) 8612–8616. doi:10.1039/c4ta00176a.
- [139] Z. Zhao, H. Tan, H. Zhao, Y. Lv, L.J. Zhou, Y. Song, Z. Sun, Reduced TiO<sub>2</sub> rutile nanorods with well-defined facets and their visible-light photocatalytic activity, *Chem. Commun.* 50 (2014) 2755–2757. doi:10.1039/c3cc49182j.
- [140] Q. Kang, J. Cao, Y. Zhang, L. Liu, H. Xu, J. Ye, Reduced TiO<sub>2</sub> nanotube arrays for photoelectrochemical water splitting, *J. Mater. Chem. A*. 1 (2013) 5766–5774. doi:10.1039/c3ta10689f.
- [141] F. Teng, M. Li, C. Gao, G. Zhang, P. Zhang, Y. Wang, L. Chen, E. Xie, Preparation of black TiO<sub>2</sub> by hydrogen plasma assisted chemical vapor deposition and its photocatalytic activity, *Appl. Catal. B Environ.* 148–149 (2014) 339–343. doi:10.1016/j.apcatb.2013.11.015.
- [142] Z. Wang, C. Yang, T. Lin, H. Yin, P. Chen, D. Wan, F. Xu, F. Huang, J. Lin, X. Xie, M. Jiang, H-doped black titania with very high solar absorption and excellent photocatalysis enhanced by localized surface plasmon resonance, *Adv. Funct. Mater.* 23 (2013) 5444–5450. doi:10.1002/adfm.201300486.
- [143] Y. Yan, B. Hao, D. Wang, G. Chen, E. Markweg, A. Albrecht, P. Schaaf, Understanding the fast lithium storage performance of hydrogenated TiO<sub>2</sub> nanoparticles, *J. Mater. Chem. A*. 1 (2013) 14507–14513.

- doi:10.1039/c3ta13491a.
- [144] X. Zhou, N. Liu, P. Schmuki, Ar<sup>+</sup>-ion bombardment of TiO<sub>2</sub> nanotubes creates co-catalytic effect for photocatalytic open circuit hydrogen evolution, *Electrochem. Commun.* 49 (2014) 60–64. doi:10.1016/j.elecom.2014.09.013.
- [145] P.A. Osorio-Vargas, C. Pulgarin, A. Sienkiewicz, L.R. Pizzio, M.N. Blanco, R.A. Torres-Palma, C. Pétrier, J.A. Rengifo-Herrera, Low-frequency ultrasound induces oxygen vacancies formation and visible light absorption in TiO<sub>2</sub> P-25 nanoparticles, *Ultrason. Sonochem.* 19 (2012) 383–386. doi:10.1016/j.ultsonch.2011.11.013.
- [146] C. Fan, X. Fu, L. Shi, S. Yu, G. Qian, Z. Wang, Disorder modification and photocatalytic activity enhancement of TiO<sub>2</sub> nanocrystals through ultrasonic hydroxylation, *J. Alloys Compd.* 703 (2017) 96–102. doi:10.1016/j.jallcom.2017.01.197.
- [147] K.S. Suslick, D.A. Hammerton, R.E. Cline, The Sonochemical Hot Spot, *J. Am. Chem. Soc.* 108 (1986) 5641–5642. doi:10.1021/ja00278a055.
- [148] L.H. Thompson, L.K. Doraiswamy, Sonochemistry: Science and engineering, *Ind. Eng. Chem. Res.* 38 (1999) 1215–1249. doi:10.1021/ie9804172.
- [149] C. Fan, C. Chen, J. Wang, X. Fu, Z. Ren, G. Qian, Z. Wang, Black Hydroxylated Titanium Dioxide Prepared via Ultrasonication with Enhanced Photocatalytic Activity, *Nat. Publ. Gr.* (2015) 1–10. doi:10.1038/srep11712.
- [150] D. MCMULLAN, Scanning Electron Microscopy 1928–1965, *Scanning.* 17 (1995) 175–185.
- [151] W. Giurlani, E. Berretti, M. Innocenti, A. Lavacchi, Measuring the thickness of metal coatings: A review of the methods, *Coatings.* 10 (2020) 1–36. doi:10.3390/coatings10121211.
- [152] Y. Alqaheem, A.A. Alomair, Microscopy and spectroscopy techniques for characterization of polymeric membranes, 2020. doi:10.3390/MEMBRANES10020033.
- [153] M.R. Linford, Introduction to surface and interface analysis and to Various Analytical Techniques, *Vac. Technol. Coat.* 78 (2014) 401–407. doi:10.2320/jinstmet.JB201403.
- [154] C. V. Stan, C.M. Beavers, M. Kunz, N. Tamura, X-ray diffraction under extreme conditions at the advanced light source, *Quantum Beam Sci.* 2 (2018) 1–33. doi:10.3390/qubs2010004.
- [155] P. Makuła, M. Pacia, W. Macyk, How To Correctly Determine the Band Gap Energy of Modified Semiconductor Photocatalysts Based on UV-Vis Spectra, *J. Phys. Chem. Lett.* 9 (2018) 6814–6817. doi:10.1021/acs.jpcclett.8b02892.
- [156] J. Tauc, OPTICAL PROPERTIES AND ELECTRONIC STRUCTURE OF AMORPHOUS Ge AND Si, *Mat. Res. Bull.* 3 (1968) 37–46.
- [157] A. Bakandritsos, M. Pykal, P. Blonski, P. Jakubec, D.D. Chronopoulos, K.K. Poláková, V. Georgakilas, K. Cepe, O.O. Tomanec, V.V. Ranc, A.B. Bourlinos, R. Zboril, M. Otyepka, D.D. Chronopoulos, P. Błoński, O.O. Tomanec, A. Bakandritsos, R. Zbořil, K. Čépe, A.B. Bourlinos, M. Otyepka, M. Pykal, P. Jakubec, V. Georgakilas, K.K. Poláková, Cyanographene and Graphene Acid: Emerging Derivatives Enabling High-Yield and Selective Functionalization of Graphene, *ACS Nano.* 11 (2017) 2982–2991. doi:10.1021/acsnano.6b08449.
- [158] D.D. Chronopoulos, A. Bakandritsos, M. Pykal, R. Zboril, M. Otyepka, Chemistry, properties, and applications of fluorographene, *Appl. Mater. Today.* 9 (2017) 60–70. doi:10.1016/j.apmt.2017.05.004.
- [159] R. Langer, E. Fako, P. Blonski, M. Vavrecka, M. Otyepka, N. Lopez, Anchoring of single-platinum-adatoms on cyanographene: Experiment and theory, *Appl. Mater. Today.* 18 (2020) 100462. doi:10.1016/j.apmt.2019.100462.

- [160] G. Tian, H. Fu, L. Jing, B. Xin, K. Pan, Preparation and Characterization of Stable Biphase TiO<sub>2</sub> Photocatalyst with High Crystallinity, Large Surface Area, and Enhanced Photoactivity, *J. Phys. Chem. C*. 112 (2008) 3083–3089. doi:10.1021/jp710283p.
- [161] A. Bakandritsos, M. Pykal, P. Blonski, P. Jakubec, D.D. Chronopoulos, K. Poláková, V. Georgakilas, K. Cepe, O. Tomanec, V. Ranc, A.B. Bourlinos, R. Zboril, M. Otyepka, Cyanographene and Graphene Acid: Emerging Derivatives Enabling High-Yield and Selective Functionalization of Graphene, *ACS Nano*. 11 (2017) 2982–2991. doi:10.1021/acsnano.6b08449.
- [162] L. Gu, J. Wang, H. Cheng, Y. Zhao, L. Liu, X. Han, One-Step Preparation of Graphene-Supported Anatase TiO<sub>2</sub> with Exposed {001} Facets and Mechanism of Enhanced Photocatalytic Properties, *ACS Appl. Mater. Interfaces*. 5 (2013) 3085–3093. doi:10.1021/am303274t.
- [163] S.P. Albu, H. Tsuchiya, S. Fujimoto, P. Schmuki, TiO<sub>2</sub> nanotubes - Annealing effects on detailed morphology and structure, *Eur. J. Inorg. Chem.* 2010 (2010) 4351–4356. doi:10.1002/ejic.201000608.
- [164] D. Zhao, G. Sheng, C. Chen, X. Wang, Enhanced photocatalytic degradation of methylene blue under visible irradiation on graphene@TiO<sub>2</sub> dyade structure, *Applied Catal. B, Environ.* 111–112 (2012) 303–308. doi:10.1016/j.apcatb.2011.10.012.
- [165] Y. Zhang, Z.-R. Tang, X. Fu, Y.-J. Xu, Engineering the Unique 2D Mat of Graphene to Achieve Graphene-TiO<sub>2</sub> Nanocomposite for Photocatalytic Selective Transformation: What Advantage does Graphene Have over Its Forebear Carbon Nanotube?, *ACS Nano*. 5 (2011) 7426–7435. doi:10.1021/nn202519j.
- [166] M. Tayebi, M. Kolaei, A. Tayyebi, Z. Masoumi, Z. Belbasi, B. Lee, Reduced graphene oxide (RGO) on TiO<sub>2</sub> for an improved photoelectrochemical (PEC) and photocatalytic activity, *Sol. Energy*. 190 (2019) 185–194. doi:10.1016/j.solener.2019.08.020.
- [167] A. Chen, S. Nigro, Influence of a Nanoscale Gold Thin Layer on Ti/SnO<sub>2</sub>-Sb<sub>2</sub>O<sub>5</sub> Electrodes, *J. Phys. Chem B*. 107 (2003) 13341–13348. doi:10.1021/jp036138w.
- [168] Y. Rambabu, M. Jaiswal, S.C. Roy, Enhanced Photo-Electrochemical Performance of Reduced Graphene- Oxide Wrapped TiO<sub>2</sub> Multi-Leg Nanotubes, *J. Electrochem. Soc.* 8 (2016) H652–H656. doi:10.1149/2.0351608jes.
- [169] X.Y. Yu, J.Y. Liao, K.Q. Qiu, D. Bin Kuang, C.Y. Su, Dynamic study of highly efficient CdS/CdSe quantum dot-sensitized solar cells fabricated by electrodeposition, *ACS Nano*. 5 (2011) 9494–9500. doi:10.1021/nn203375g.
- [170] A. Zaban, M. Greenshtein, J. Bisquert, Determination of the electron lifetime in nanocrystalline dye solar cells by open-circuit voltage decay measurements, *ChemPhysChem*. 4 (2003) 859–864. doi:10.1002/cphc.200200615.
- [171] S. Spillias, P. Kareiva, M. Ruckelshaus, E. Mcdonald-madden, Renewable energy targets may undermine their sustainability, *Nat. Clim. Chang.* 10 (2020) 974–976. doi:10.1038/s41558-020-00939-x.
- [172] M. Xiao, L. Zhang, B. Luo, M. Lyu, Z. Wang, H. Huang, S. Wang, A. Du, L. Wang, Molten-Salt-Mediated Synthesis of an Atomic Nickel Co-catalyst on TiO<sub>2</sub> for Improved Photocatalytic H<sub>2</sub> Evolution, *Angew. Chem.* 132 (2020) 7297–7301. doi:10.1002/ange.202001148.
- [173] S. Kment, F. Riboni, S. Pausova, L. Wang, L. Wang, H. Han, Z. Hubicka, J. Krysa, P. Schmuki, R. Zboril, Photoanodes based on TiO<sub>2</sub> and  $\alpha$ -Fe<sub>2</sub>O<sub>3</sub> for solar water splitting – superior role of 1D nanoarchitectures and of combined heterostructures, *Chem. Soc. Rev.*, 46 (2017) 3716. doi:10.1039/c6cs00015k.
- [174] C. Cao, W. Song, Single-Atom Catalysts for Thermal Heterogeneous Catalysis in Liquid: Recent Progress and Future Perspective, *ACS Mater. Lett.* 2 (2020) 1653–

1661. doi:10.1021/acsmaterialslett.0c00349.
- [175] M. Xiao, J. Zhu, G. Li, N. Li, S. Li, Z.P. Cano, L. Ma, P. Cui, P. Xu, G. Jiang, H. Jin, S. Wang, T. Wu, J. Lu, A. Yu, D. Su, Z. Chen, A Single-Atom Iridium Heterogeneous Catalyst in Oxygen Reduction Reaction, *Angew. Chem. Int. Ed.* 131 (2019) 9742–9747. doi:10.1002/ange.201905241.
- [176] E.C. Tyo, S. Vajda, Catalysis by clusters with precise numbers of atoms, *Nat. Nanotechnol.* 10 (2015) 577–588. doi:10.1038/nnano.2015.140.
- [177] J. Han, J. Lu, M. Wang, Y. Wang, F. Wang, Single Atom Alloy Preparation and Applications in Heterogeneous Catalysis, *Chin. J. Chem.* 37 (2019) 977–988. doi:10.1002/cjoc.201900185.
- [178] S.M.H. Hejazi, M. Shahrezaei, P. Błoński, M. Allieta, P.M. Sheverdyeva, P. Moras, Z. Bad'ura, S. Kalytchuk, E. Mohammadi, R. Zbořil, Š. Kment, M. Otyepka, A. Naldoni, P. Fornasiero, Defect engineering over anisotropic brookite toward substrate-specific photo-oxidation of alcohols, *Chem Catal.* 2 (2022) 1177–1190. doi:10.1016/j.checat.2022.03.015.
- [179] M. Shahrezaei, A.A. Babaluo, S. Habibzadeh, M. Haghghi, Photocatalytic Properties of 1D TiO<sub>2</sub> Nanostructures Prepared from Polyacrylamide Gel–TiO<sub>2</sub> Nanopowders by Hydrothermal Synthesis, *Eur. J. Inorg. Chem.* 2017 (2017) 694–703. doi:10.1002/ejic.201600820.
- [180] M. Shahrezaei, S. Habibzadeh, A.A. Babaluo, H. Hosseinkhani, M. Haghghi, A. Hasanzadeh, R. Tahmasebpour, Study of synthesis parameters and photocatalytic activity of TiO<sub>2</sub> nanostructures, *J. Exp. Nanosci.* 12 (2017) 45–61. doi:10.1080/17458080.2016.1258495.
- [181] J. Yang, D. Wang, H. Han, C.A.N. Li, Roles of Cocatalysts in Photocatalysis and Photoelectrocatalysis, *Acc. Chem. Res.* 46 (2013) 1900–1909.
- [182] M. Yoo, Y.-S. Yu, H. Ha, S. Lee, J.-S. Choi, S. Oh, E. Kang, H. Choi, H. An, K.-S. Lee, J.Y. Park, R. Celestre, M.A. Marcus, K. Nowrouzi, D. Taub, D.A. Shapiro, W. Jung, C. Kim, H.Y. Kim, A tailored oxide interface creates dense Pt single-atom catalysts with high catalytic activity, *Energy Environ. Sci.* 13 (2020) 1231–1239. doi:10.1039/c9ee03492g.
- [183] A. Naldoni, M. Allieta, S. Santangelo, M. Marelli, F. Fabbri, S. Cappelli, C.L. Bianchi, R. Psaro, V.D. Santo, Effect of Nature and Location of Defects on Bandgap Narrowing in Black TiO<sub>2</sub> Nanoparticles, *J. Am. Chem. Soc.* 134 (2012) 7600–7603.
- [184] J. Eom, S. Lim, S. Lee, W. Ryu, H. Kwon, Black titanium oxide nanoarray electrodes for high rate Li-ion microbatteries, *J. Mater. Chem. A.* 3 (2015) 11183–11188. doi:10.1039/c5ta01718a.
- [185] L. Xiong, J. Li, B. Yang, Y. Yu, Ti<sup>3+</sup> in the Surface of Titanium Dioxide: Generation, Properties and Photocatalytic Application, *J. Nanomater.* 2012 (2012) 831524. doi:10.1155/2012/831524.
- [186] X. Jiang, Y. Zhang, J. Jiang, Y. Rong, Y. Wang, Y. Wu, C. Pan, Characterization of Oxygen Vacancy Associates within Hydrogenated TiO<sub>2</sub>: A Positron Annihilation Study, *J. Phys. Chem. C.* 116 (2012) 22619–22624.
- [187] R. Yew, S.K. Karuturi, J. Liu, H.H. Tan, Y. Wu, C. Jagadish, Exploiting defects in TiO<sub>2</sub> inverse opal for enhanced photoelectrochemical water splitting, *Opt. Express.* 27 (2019) 761–773. doi:10.1364/oe.27.000761.
- [188] M. Lamers, S. Fiechter, D. Friedrich, F.F. Abdi, R. Van De Krol, Formation and suppression of defects during heat treatment of BiVO<sub>4</sub> photoanodes for solar water splitting, *J. Mater. Chem. A.* 6 (2018) 18694–18700. doi:10.1039/c8ta06269b.
- [189] L. Li, J. Yan, T. Wang, Z. Zhao, J. Zhang, J. Gong, N. Guan, Sub-10 nm rutile titanium dioxide nanoparticles for efficient visible-light-driven photocatalytic hydrogen production, *Nat. Commun.* 6 (2015) 5881. doi:10.1038/ncomms6881.

- [190] P. Ghosh, M. Azimi, Numerical Calculation of Effective Permittivity of Lossless Dielectric Mixtures using Boundary Integral Method, *IEEE Trans. Dielectr. Electr. Insul.* 1 (1994) 975–981.
- [191] L. Zhu, H. Ma, H. Han, Y. Fu, C. Ma, Z. Yu, X. Dong, Black TiO<sub>2</sub> nanotube arrays fabricated by electrochemical self-doping and their photoelectrochemical performance, *RSC Adv.* 8 (2018) 18992–19000. doi:10.1039/c8ra02983k.
- [192] L. Wei, Y. Yang, X. Xia, R. Fan, T. Su, Y. Shi, J. Yu, L. Li, Y. Jiang, Band edge movement in dye sensitized Sm-doped TiO<sub>2</sub> solar cells: A study by variable temperature spectroelectrochemistry, *RSC Adv.* 5 (2015) 70512–70521. doi:10.1039/c5ra15815j.
- [193] M. Kolaei, M. Tayebi, Z. Masoumi, B.K. Lee, A novel approach for improving photoelectrochemical water splitting performance of ZnO-CdS photoanodes: Unveiling the effect of surface roughness of ZnO nanorods on distribution of CdS nanoparticles, *J. Alloys Compd.* 906 (2022) 164314. doi:10.1016/j.jallcom.2022.164314.
- [194] T. Xu, H. Zheng, P. Zhang, Isolated Pt single atomic sites anchored on nanoporous TiO<sub>2</sub> film for highly efficient photocatalytic degradation of low concentration toluene, *J. Hazard. Mater.* 388 (2020) 121746. doi:10.1016/j.jhazmat.2019.121746.
- [195] H. Wang, J.X. Liu, L.F. Allard, S. Lee, J. Liu, H. Li, J. Wang, J. Wang, S.H. Oh, W. Li, M. Flytzani-Stephanopoulos, M. Shen, B.R. Goldsmith, M. Yang, Surpassing the single-atom catalytic activity limit through paired Pt-O-Pt ensemble built from isolated Pt1 atoms, *Nat. Commun.* 10 (2019) 3808. doi:10.1038/s41467-019-11856-9.
- [196] R. Lang, W. Xi, J. Liu, Y. Cui, T. Li, A.F. Lee, F. Chen, Y. Chen, L. Li, L. Li, J. Lin, S. Miao, X. Liu, A. Wang, X. Wang, J. Luo, B. Qiao, J. Li, T. Zhang, Non defect-stabilized thermally stable single-atom catalyst, *Nat. Commun.* 10 (2019) 234. doi:10.1038/s41467-018-08136-3.
- [197] N. Daelman, M. Capdevila-cortada, N. López, Dynamic charge and oxidation state of Pt/CeO<sub>2</sub> single-atom catalysts, *Nat. Mater.* 18 (2019) 1215–1221. doi:10.1038/s41563-019-0444-y.
- [198] Y. Hang Li, J. Xing, Z. Jia Chen, Z. Li, F. Tian, L. Rong Zheng, H. Feng Wang, P. Hu, H. Jun Zhao, H. Gui Yang, Unidirectional suppression of hydrogen oxidation on oxidized platinum clusters, *Nat. Commun.* 4 (2013) 2500. doi:10.1038/ncomms3500.
- [199] Z. Lian, W. Wang, G. Li, F. Tian, K.S. Schanze, H. Li, Pt-Enhanced Mesoporous Ti<sup>3+</sup>/TiO<sub>2</sub> with Rapid Bulk to Surface Electron Transfer for Photocatalytic Hydrogen Evolution, *ACS Appl. Mater. Interfaces.* 9 (2017) 16959–16966. doi:10.1021/acsami.6b11494.

## List of abbreviations and acronyms

XRD	X-ray diffraction spectroscopy
XPS	X-ray photoelectron spectroscopy
SEM	Scanning electron microscopy
UV	Ultraviolet
EPR	Electron paramagnetic resonance
HR-TEM	High resolution Transmission electron microscopy
HAADF	High-angle annular dark-field imaging
IPCE	Incident photon-to-current efficiency
IMPS	Intensity-modulated photocurrent spectroscopy
EIS	Electrochemical impedance spectroscopy
PEC	Photoelectrochemical
Ti	Titanium
BSE	Backscattered electrons
SE	Secondary electrons
EDS	Energy-dispersive X-ray spectroscopy
MLTNTS	Multi-leg TiO <sub>2</sub> nanotubes
1-D	One dimensional
DMSO	Dimethyl sulfoxide

## List of abbreviations and acronyms

EG	Ethylene glycol
AM	Air mass
RT	Room temperature
$V_{ocd}$	Open circuit voltage
NP	Nanoparticle
SA	Single atom
e-	electron
h+	hole
$\Phi$	Work function
$\theta$	X-ray scattering angle
$\lambda$	Wavelength



## List of Publications

- 1- **Mahdi Shahrezaei**, Seyyed Mohammad Hossein Hejazi, Yalavarthi Rambabu, Miroslav Vavrecka, Aristides Bakandritsos, Selda Oezkan, Radek Zboril, Patrik Schmuki, Alberto Naldoni and Stepan Kment, “Multi-Leg TiO<sub>2</sub> Nanotube Photoelectrodes Modified by Platinized Cyanographene with Enhanced Photoelectrochemical Performance”, *Catalysts* 2020, 10, 717. Doi.org/10.3390/catal10060717.
- 2- S. M. Hossein Hejazi, **Mahdi Shahrezaei**, Piotr Błonski, Mattia Allieta, Polina M. Sheverdyeva, Paolo Moras, Zdenek Badura, Sergii Kalytchuk, Elmira Mohammadi, Radek Zboril, Stepan Kment, Michal Otyepka, Alberto Naldoni and Paolo Fornasiero, “Defect engineering over anisotropic brookite toward substrate-specific photo-oxidation of alcohols”, *Chem Catalysis* 2022, 2, 5, 1177-1190. Doi.org/10.1016/j.checat.2022.03.015.
- 3- **Mahdi Shahrezaei**, S. M. Hossein Hejazi, Hana Kmentova, Veronika Sedajova, Radek Zboril, Alberto Naldoni, and Stepan Kment “Ultrasound-driven defect engineering in TiO<sub>2-x</sub> nanotubes – towards highly efficient platinum single atom enhanced photocatalytic water splitting” *ACS AMI* 2023. Doi.org/10.1021/acsami.3c04811

**Department of Physical Chemistry**

**Faculty of Science**

**PALACKY UNIVERSITY, OLOMOUC**



**Hybrid nanostructures for photoelectrochemical  
water splitting**

Doctoral Dissertation

Author:

**Mahdi Shahrezaei, MSc**

Supervisor:

**Štěpán Kment, Ph.D.**

Under:

Study program: P1417 Chemistry

Field of study: Physical Chemistry

Olomouc 2023

I hereby declare that the Ph.D. thesis entitled “Hybrid nanostructures for photoelectrochemical water splitting” is an authentic record of my research work performed during my doctoral study under the supervision of Associate Professor Štěpán Kment. All experimental work of this thesis is performed in the Czech Advanced Technologies and Research Institute (CATRIN-RCPTM) as well as the Department of Physical Chemistry, Palacký University Olomouc. All the further information used for this original work has been referenced as well. I declare that this dissertation contains no material, which has been submitted elsewhere as part of any academic degree.

In Olomouc.....

Signature of candidate

<b>Candidate</b>	Mahdi Shahrezaei, M.Sc. Department of Physical Chemistry, Faculty of science, Palacký university Olomouc.
<b>Supervisor:</b>	Štěpán Kment, Ph.D.
<b>Opponent</b>	
<b>Opponent</b>	

Date and place of dissertation defense:

.....

The doctoral thesis is available at the study department of Faculty of Science of Palacký University Olomouc.

## Table of contents

<b>Table of contents</b> .....	<b>iii</b>
<b>Abstract</b> .....	<b>4</b>
<b>Introduction and the aim of this project</b> .....	<b>5</b>
<i>1.1 Introduction</i> .....	5
<i>1.2 The aim of this work</i> .....	6
<b>Results</b> .....	<b>7</b>
<i>2.1 TiO<sub>2</sub> Nanotube Photoelectrodes Modified by Platinized Cyanographene</i> .	7
<i>2.2 Pt-SA decoration</i> .....	16
<b>References</b> .....	<b>27</b>
<b>List of Publications</b> .....	<b>31</b>

## Abstract

The rapid decrease of non-renewable fossil fuel reserves and increase in the amount of carbon emission have negative environmental impacts as well as a decline in the quality of life in all countries. Renewable and abundant energy such as solar as harmless energy, has already gained massive attention due to its availability in nature. The environment and energy are closely related to each other and therefore environmental problem results from an interaction between human activity and energy consumption. Hydrogen ( $H_2$ ) is a promising alternative energy carrier for the future energy system, which can be obtained, for example, from the electrolysis of water and photoelectrochemical water splitting (PEC-WS). The core component of a PEC cell is a semiconductor and among several of them, titanium dioxide ( $TiO_2$ ) has been the most widely investigated material for photocatalytic application. Various  $TiO_2$  nanostructures have been employed in photocatalytic applications; however, 1-D nanostructures (e.g., nanotubes) provide a high surface area, which is more suitable for this purpose. Because of some inherent weaknesses of  $TiO_2$ , the presence of a co-catalyst is required for photocatalytic reactions. We have synthesized 1-D  $TiO_2$  nanotubes via the electrochemical anodization method. Then, to improve the performance of fabricated photoelectrode material for PEC-WS, the electrodeposition method was used to make a composite with platinized cyanographene (G-CN/Pt). In continuation with that, we focused on photocatalytic  $H_2$  evolution of Pt single-atom (Pt-SA) decorated on 1-D  $TiO_2$  nanotube surface as an advanced topic. We have employed a straightforward technique to form traps on  $TiO_2$  as a substrate for Pt-SA, which could act as a co-catalyst centre, where the reduction of  $H^+$  ions to  $H_2$  occurs.

## **Introduction and the aim of this project**

### *1.1 Introduction*

The development of society in science, technology, and human life during the last century relies heavily on fossil fuels which have brought serious problems in the quality of life due to large consumption of energy and detrimental effects on the environment [1–3]. H<sub>2</sub> is a clean and sustainable fuel without toxic emissions (carbon free) which can be produced from a variety of resources such as natural gas, fossil fuels, and water. There are several methods to produce H<sub>2</sub> including electrolysis of water, high-temperature water splitting, photoelectrocatalysis, and photocatalysis [4,5]. In 1972, Fujishima reported one of the most promising and efficient approaches for solar-to-chemical energy conversion using semiconductors [6,7]. Afterward, many efforts have been dedicated to improving the photocatalytic efficiency of semiconductors. Among the variety of semiconductors for photocatalysis, TiO<sub>2</sub> is the most-investigated catalyst because of its relatively low cost, high chemical stability, low environmental toxicity, and superior photocatalytic performance [8–10]. However, the wide application of TiO<sub>2</sub> photocatalyst is restricted by its large bandgap (*e.g.*, anatase TiO<sub>2</sub>, E<sub>g</sub> = 3.2 eV) that is only UV light-responsive, limiting its usage under the whole light spectrum. Moreover, the high recombination rate of photoinduced electron–hole (e<sup>-</sup>/h<sup>+</sup>) pairs also affects their photoactivity [11]. Many attempts have been made to modify TiO<sub>2</sub> photocatalyst activity by loading the noble metals (*i.e.*, Pt, Rh, and Au) [12,13], doping with non-metal elements (*i.e.*, N, S, and C) [14,15], and coupling with narrow bandgap semiconductors [16]. In 1984, Assefpour-Dezfuly and co-workers [17] reported the formation of self-organized 1-D TiO<sub>2</sub> nanotubes using the anodization method. Over the last decade, One-dimensional (1D) TiO<sub>2</sub> nanotubes (TNTs) have been widely studied because of their magnificent properties to

outperform their bulk/nanoparticles counterparts in photocatalytic activity. For instance, the surface area and the light-harvesting efficiency considerably increase [18]. Further, due to the separation and recycling of solid catalysts from liquid phases often place high demands, this drawback has been overcome by using TNTs. Several methods such as the hydrothermal method, sol-gel, and aluminum template are utilized to synthesize TNTs [19,20]. However, electrochemical anodization of Ti metal in the fluoride-containing electrolyte is the most commonly applied technique for much better control over the dimension and long-range order [21,22]. In general, there is also considerable research into the fabrication of heterojunctions between TiO<sub>2</sub> and other partners in different hybrid nanostructures to improve charge separation and light absorption. Over the last decade, the development of TiO<sub>2</sub> heterojunctions with carbon-based allotropes as well as doping with noble metals has been investigated [23]. For this purpose, TiO<sub>2</sub> nanotubes decorated with platinized cyanographene (G-CN/Pt) and Pt-SA catalysts are developed to improve their photocatalytic performances.

### *1.2 The aim of this work*

TiO<sub>2</sub> has attracted significant interest for its distinctive properties, including environmentally friendly, chemical stability, and suitable band edge position, which makes it a widely explored material for applications in photocatalysis and photoelectrocatalysis. However, due to its wide bandgap and fast recombination rate of photogenerated electron-hole pairs, synthesized TiO<sub>2</sub> demonstrates relatively low efficiency in both photocatalytic and photoelectrochemical performance. Therefore, many researchers have been focusing on developing methods to overcome these intrinsic limitations. Decoration of TiO<sub>2</sub> with noble metals and carbonaceous nanomaterials, capable of serving as electron transfer mediators, offers a promising strategy for its photocatalytic activity for hydrogen (H<sub>2</sub>) production. Thus, within this work, we determined the optimal condition for decorating TiO<sub>2</sub> with G-CN, G-CN/Pt, and Pt-SA, thereby amplifying the photocatalytic activity of

the TiO<sub>2</sub> nanostructure. For this reason, we have synthesized compact and discrete 1D TiO<sub>2</sub> nanotubes. Subsequently, we fabricated the discrete TiO<sub>2</sub> nanotubes/platinized cyanographene and cyanographene heterojunctions to get more information about their photoelectrochemical water splitting. Lastly, we conducted a controlled loading of Pt single atoms onto TiO<sub>2</sub> nanotubes to investigate their potential for photocatalytic H<sub>2</sub> production.

## Results

### 2.1 TiO<sub>2</sub> Nanotube Photoelectrodes Modified by Platinized Cyanographene

Multi-leg TiO<sub>2</sub> nanotube (MLTNTs) is obtained by electrochemical anodization on Ti foil. Then, the proposal of making them functionalized with cyanographene as well as platinized cyanographene (G/CN and G-CN/Pt, respectively) is suggested as a hybrid photoelectrode to enhance PEC water splitting. Electrodeposition as a cost-efficient and time-saving method is used to produce a composite (Figure 1). For the sake of simplicity, pristine TiO<sub>2</sub> nanotubes, cyanographene nanotubes, and platinized cyanographene TiO<sub>2</sub>

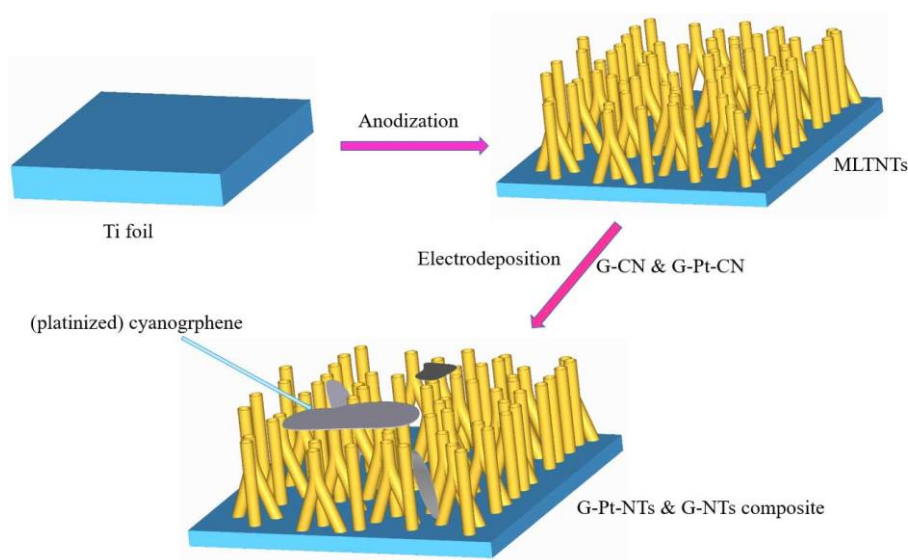


Figure 1. Schematic illustration of the entire process of making composite using electrodeposition.

nanotubes composite are hereafter referred to as P-NTs, G-NTs, and G-Pt-NTs, respectively.

SEM images in Figure 2a–f show the pristine nanotubes (P-NTs) and the synthesized composite samples (G-NTs and G-Pt-NTs). The morphology of multi-leg and largely open ends of TiO<sub>2</sub> nanotubes can be seen with the mean length and diameter of about 3.3  $\mu\text{m}$  and 300 nm, respectively. As shown in Figure 2c-f, the most attractive advantage is that not only on the top surface of the TiO<sub>2</sub> nanotubes but also deep inside the nanostructure, G/CN and G-CN/Pt sheets were deposited. However, for the typical close-packed TiO<sub>2</sub> nanotubes, G/CN sheets would only be deposited on the top of the TiO<sub>2</sub> nanotubes, and closely touching the walls of the tubes are impossible.

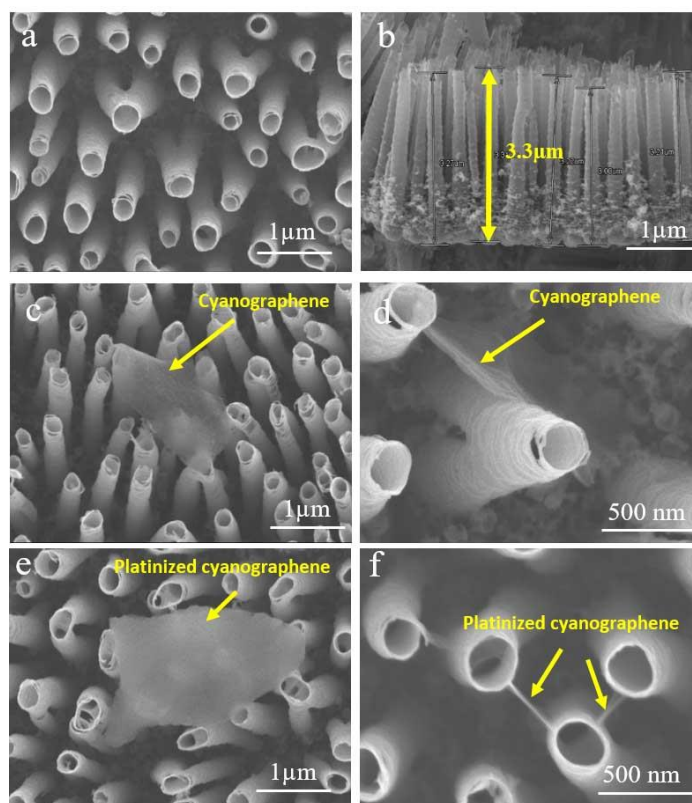


Figure 2 SEM images of fabricated samples: a) P-NTs, b) showing cross-section of P-NTs, c-d) G-NTs, e-f) G-Pt-NTs.

Raman spectra displayed bands at about 148 ( $E_g$ ), 396 ( $B_{1g}$ ), 516 ( $B_{1g}$  or  $A_{1g}$ ), and 636 ( $E_g$ )  $\text{cm}^{-1}$  of the anatase phase [24] for all three samples. Further, as shown in Figure 3a, Raman spectra of hybrids confirm the existence of G-CN and G-CN/Pt within the

MLTNTs arrays, in which, the two main peaks placed at 1365 and 1569  $\text{cm}^{-1}$  are attributed to the characteristic D band and G band of cyanographene [25]. The D and G peaks stem from the structural disorder and bond stretching of all  $\text{sp}^2$  carbon atoms (C–C), respectively. The crystal structures and compositions of P-NTs were further characterized by X-ray diffraction (XRD) pattern (Figure 3b). Due to the as-prepared  $\text{TiO}_2$  nanotubes being amorphous, all the prepared samples were annealed at 450°C for 180 min in air.

The XRD analysis of the calcined P-NTs sample shows the anatase phase and the formation of very little rutile phase owing to the oxidation of titanium (Ti) metal beneath the  $\text{TiO}_2$  nanotubes at the interface of  $\text{TiO}_2$  nanotubes and Ti metal during the annealing of the sample in the furnace [26]. UV-vis diffuse reflectance absorption spectra (DRS) of pristine nanotubes and composite samples were measured (Figure 3c). We observed a red-shift of absorption edge, about 10–20 nm, and a higher absorption in the visible range for the G-CN and G-CN/Pt in comparison with pristine P-NTs. This can be because of the electronic interactions between cyanographene and  $\text{TiO}_2$  nanotubes [27,28]. In addition, the compositions and chemical state of the G-Pt-NTs sample were analysed by XPS. All XPS spectra were calibrated by shifting the spectra to the binding energy of C1s of 258.6 eV. The high-resolution XPS spectra of Ti2P, C1s, and Pt4f of the G-Pt-NTs sample are shown in Figure 3d–f. As shown in Figure 3d, the four peaks at 284.5, 286.0, 287, and 288.8 eV are assigned to C–C, C–N, C=O, and O=C–O, respectively, which is very well in agreement with the results of synthesized cyanographene [25]. This result confirms that during the electrodeposition onto  $\text{TiO}_2$  nanotubes, the chemical structure of cyanographene has not been changed. In Figure 3e, the broad peaks at 459 eV and 464.7 eV are related to the Ti  $2\text{p}_{3/2}$  and Ti  $2\text{p}_{1/2}$  orbitals of  $\text{Ti}^{4+}$  in the  $\text{TiO}_2$  lattice, respectively [29]. Moreover, as shown in Figure 3f, the two peaks at 71.4 and 42.9 eV confirmed the presence of metallic Pt (*i.e.*,  $\text{Pt}^0$ ) in the G-Pt-NTs sample.

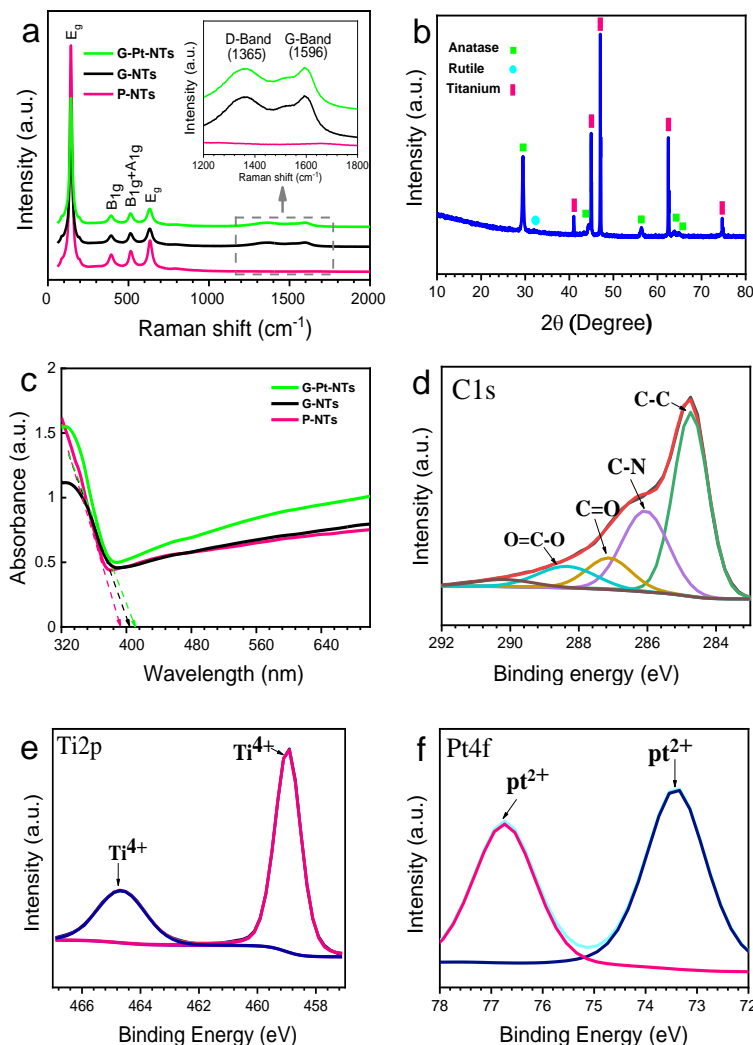


Figure 3 a) Raman spectra of P-NTs, G-NTs and G-Pt-NTs samples (the inset shows the magnified Raman spectra), b) XRD analysis of TiO<sub>2</sub> nanotubes annealed at 450°C in air (using cobalt X-ray source), c) UV-vis DRS of P-NTs, G-NTs, and G-Pt-NTs, and (d–f) HRXPS spectra of C1s (d), Ti2p (e), and Pt4f (f) of G-Pt-NTs sample.

The PEC activity of all fabricated photoanode was evaluated using linear sweep voltammetry (LSV) under 1 sun illumination (Figure 4a). Current density-voltage (J-V) characteristics of P-NTs, G-NTs, and G-Pt-NTs were measured using a xenon lamp equipped with an AM1.5 G filter and with the light intensity of 1 sun (100 mW cm<sup>-2</sup>). From the photocurrent versus curve, it is evident that for the composite samples, compared to the pristine TiO<sub>2</sub> nanotubes (P-NTs) the photocurrent density is enhanced. The highest photocurrent density of 121 μA cm<sup>-2</sup> (hereafter at 1.3 V vs. RHE) was reached

by the G-Pt-NTs sample. Whereas, the G-NTs and P-NTs samples showed less photocurrent densities ( $91 \mu\text{A cm}^{-2}$  and  $73 \mu\text{A cm}^{-2}$ , respectively) than G-Pt-NTs. Such enhancement of the photocurrent, which is nearly 66% and 33% higher than that of P-NTs and G-NTs samples, respectively, might result from faster charge transfer, as a direct consequence of using G-CN and G-CN/Pt in the composite samples. Figure 5b indicates the incident photon-to-electron conversion efficiency (IPCE) spectra of the P-NTs, G-NTs, and G-Pt-NTs samples at 1.5V vs. RHE in a 1 M NaOH solution. All photoanodes show the same trend in photoactivity as well as significantly enhanced photoactivity in the UV region. Based on our experiment, the G-Pt-NTs sample has the highest IPCE value, reaching about 58% at 300 nm, which is in line with the results of the PEC activity of the synthesized samples. The photostability test of the most active G-Pt-NTs sample over time was carried out through the chronoamperometry test with the fixed bias voltage +1.5 V vs RHE and continuous illumination light of nearly 25,000 s under 1 sun illumination ( $100 \text{ mW cm}^{-2}$ ). As shown in Figure 6c, the prepared photoanode also demonstrated good stability for 25,000 s continuous illumination and reached approximately 90% of the initial current. The improvement in the PEC performance of composite samples was attributed to the hybridizing of  $\text{TiO}_2$  with platinized cyanographene, which improves the charge separation/transfer rate and the overall PEC performance.

To investigate the charge transfer capability of photoanodes, electrochemical impedance spectroscopy (EIS) was performed under 1 sun illumination in the frequency range of 0.1 Hz to 100 kHz at the bias potential +1.5 V vs. RHE. Figure 5a shows the Nyquist plots obtained at each potential vs. RHE for PNTs, G-NTs, and G-Pt-NTs samples. The Inset of Figure 5a shows the equivalent circuit diagrams obtained using Z-View software. Here  $R_s$  was the overall resistance between the electrode and electrolyte, which can be calculated from the X-intercept of the Nyquist plot. The value of  $R_s$  for P-

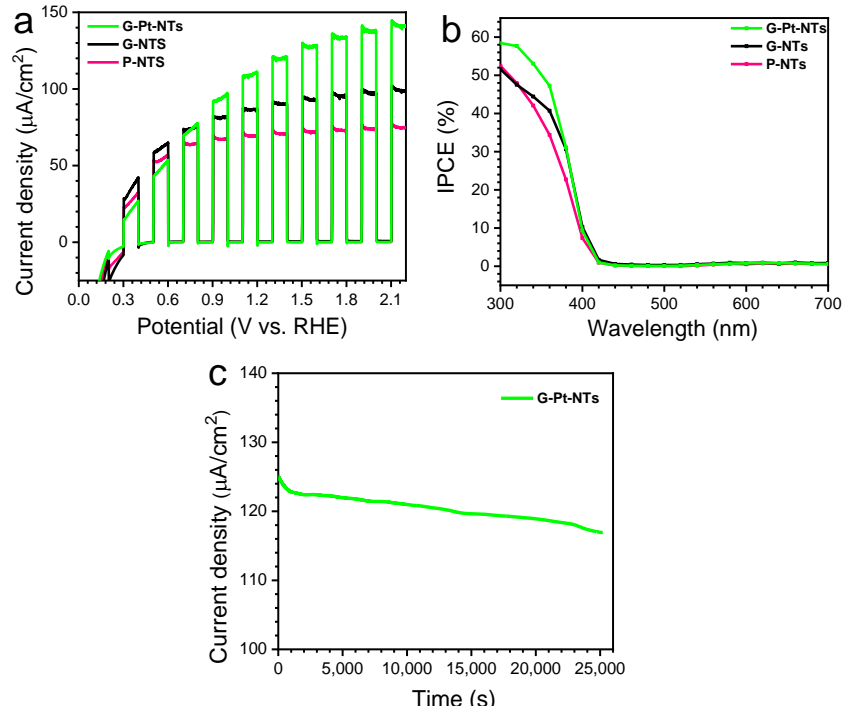


Figure 7 a) Photocurrent spectra of fabricated samples measured in 1 M NaOH solution under AM 1.5 and 1 sun illumination ( $100 \text{ W}/\text{m}^2$ ), b) corresponding IPCE spectra, c) Photostability test of G-Pt-NTs in 1 M NaOH solution, potential 1.5 V vs RHE for 7 h where the pH is 13.6.

NTs, G-NTs, and G-Pt-NTs composite was almost similar for all samples, which is determined around  $11 \Omega$  (Table 1). The  $R_{\text{SC}}$  and  $R_{\text{ct}}$  correspond to the bulk charge transport and the interfacial charge transfer resistance, respectively. However, no significant difference was observed for the  $R_{\text{SC}}$  value and was obtained to be  $95.7 \Omega$ ,  $88.28 \Omega$ , and  $106 \Omega$  for P-NTs, G-NTs, and G-Pt-NTs composite, respectively. Furthermore, the radius of the semicircle for the G-Pt-NTs sample is smaller than P-NTs and G-NTs ones, and it declines as follows: P-NTs > G-NTs > G-Pt-NTs. Therefore, the addition of G-CN/Pt and G/CN into the  $\text{TiO}_2$  nanotube structure leads to the fastest interfacial hole transfer and efficient separation of  $e^-$ - $h^+$  pairs. The  $R_{\text{ct}}$  value was obtained  $105940 \Omega$ ,  $38442 \Omega$ , and  $27954 \Omega$  for P-NTs, G-NTs, and G-Pt-NTs composite, respectively. Thus, these indicate that the pristine G-CN causes improvement of charge transfer kinetics to  $\text{TiO}_2$  nanotubes. In addition, G-CN/Pt results in further improvement in the performance of the composite by an additional  $\sim 27\%$ , and more efficient charge

separation may also be due to the presence of Pt in the composite sample. The constant phase element (CPE1) represents the space charge layer ( $C_{sc}$ ) and the constant phase element (CPE2) depicts the semiconductor electrolyte interface ( $C_{SE}$ ) [30,31].

The value of CPE-1 decreases in the following order P-NTs < G-NTs < G-Pt-NTs, presenting that the electron-hole pair separation of G-Pt-NTs compared to P-NTs and G-NTs improved efficiently. Interestingly, the CPE1 value is greatly enhanced for G-Pt-NTs and G-NTs samples in comparison with P-NTs about 72 and 10 times, respectively. The observation confirms the beneficial role of platinized G-CN, which can act as a charge storage reservoir as well as the significant role of G-CN/Pt as a charge separator across the space charge region for overall photocurrent enhancement. Further, the value of CPE-2 (charge transferability of photoanode to the electrolyte) is higher for G-Pt-NTs compared to Pt-NTs, while lower than G-NTs. Therefore, to understand the correlation between increased photocurrent density and charge transfer efficiency, the rate constant ( $\tau$ ) is determined as a charge transfer process across the photoanode/electrolyte interface (see Table 1) [31]. The lower  $\tau$  value represents the higher charge transfer efficiency. This value follows the order P-NTs > G-NTs > G-Pt-NTs and is well in line with the trend of photocurrent enhancement. Therefore, improvement in the charge separation (CPE1) as well as decreased charge transfer resistance ( $R_{ct}$ ) of photoanodes cause the enhancement of photocurrent in the G-Pt-NTs sample.

Table 1 Equivalent circuit components calculated by fitting the experimental electrochemical impedance spectroscopy data.

Sample	$R_s$ ( $\Omega$ )	$R_{sc}$ ( $\Omega$ )	$R_{ct}$ ( $\Omega$ )	CPE-1 ( $\mu F$ )	CPE-2 ( $\mu F$ )	$\tau = R_{ct} \times$ CPE2 (s)
P-NTs	$11.46 \pm 0.11$	$95.7 \pm 11.1$	$105,940 \pm 2828$	$2.61 \pm 0.15$	$70.20 \pm 0.7$	7.43
G-NTs	$10.22 \pm 0.09$	$88.28 \pm 9.2$	$38,442 \pm 992$	$27.2 \pm 0.9$	$102.99 \pm 0.5$	3.95
G-Pt-NTs	$11.01 \pm 0.09$	$106 \pm 19.1$	$27,954 \pm 625$	$187 \pm 11$	$78.10 \pm 0.9$	2.18

The intensity-modulated photocurrent spectroscopy (IMPS) at various intensities of light was obtained to analyse the transport time of photo-generated electrons. The transform time of photo-generated electrons ( $\tau_{trans}$ ) can be valued as shown in the equation below [32]:

$$\tau_{trans} = \frac{1}{2\pi f_{min}}$$

Where  $f_{min}$  is the minimum frequency of the IMPS plot and  $\tau_{trans}$  is the electron transfer time to the back contact layer. As shown in Figure 5b and Table 2, the G-Pt-NTs showed the fastest electron-transfer time than G-NTs and P-NTs samples. This indicates that platinized cyanographene promotes electron transfer, and charge separation within semiconductors and thus increases the photocurrent. An open-circuit voltage decay ( $V_{OCD}$ ) measurement was conducted to gain insight into the recombination properties of fabricated photoanodes. Once to turn the light off and illumination is interrupted, the decay of  $V_{OCD}(t)$  can be seen due to the recombination process at the interface between electrons in the conduction band of  $TiO_2$  and the electrolyte or bulk recombination (Figure 5c). Therefore, the interfacial charge recombination rate can be suppressed by introducing o -CN/Pt and G-CN as a conducting layer on the surface of  $TiO_2$  nanotubes. Therefore, based on obtained  $V_{CD}$  results, the electron lifetime ( $\tau_n$ ) can be valued according to the equation below [33]:

$$\tau_n = -\frac{k_B T}{e} \left( \frac{dV_{OC}}{dt} \right)^{-1}$$

Where  $e$  is a positive elementary charge,  $k_B$  is the Boltzmann constant and  $t$  is a temperature (K). The electron lifetime as a function of the  $V_{OCD}$  plot is shown in Figure 5d, representing a higher electron lifetime of the G-Pt-NTs sample. By using electron lifetime ( $\tau_n$ ) equation at an equal potential the electron lifetimes were calculated in the following order G-Pt-NTs > G-NTs > P-NTs. During the voltage decay, the smaller slope (the smallest  $V_{OCD}$  decay belonged to the G-Pt-NTs sample) shows a higher electron

lifetime. These results show the addition of cyanographene decreased the recombination rate into the TiO<sub>2</sub> nanotubes, as remarked by the one-order magnitude improvement in the electron lifetime.

Table 2 The electron transfer time ( $\tau_{\text{trans}}$ ) of photogenerated electrons determined through IMPS data analysis.

Sample	$\tau_{\text{trans}}$ (ms) at light power 80 W	$\tau_{\text{trans}}$ (ms) at light power 25 W	$\tau_{\text{trans}}$ (ms) at light power 8 W
P-NTs	1.5	2	5
G-NTs	1	1.3	2.5
G-Pt-NTs	0.5	1	2.1

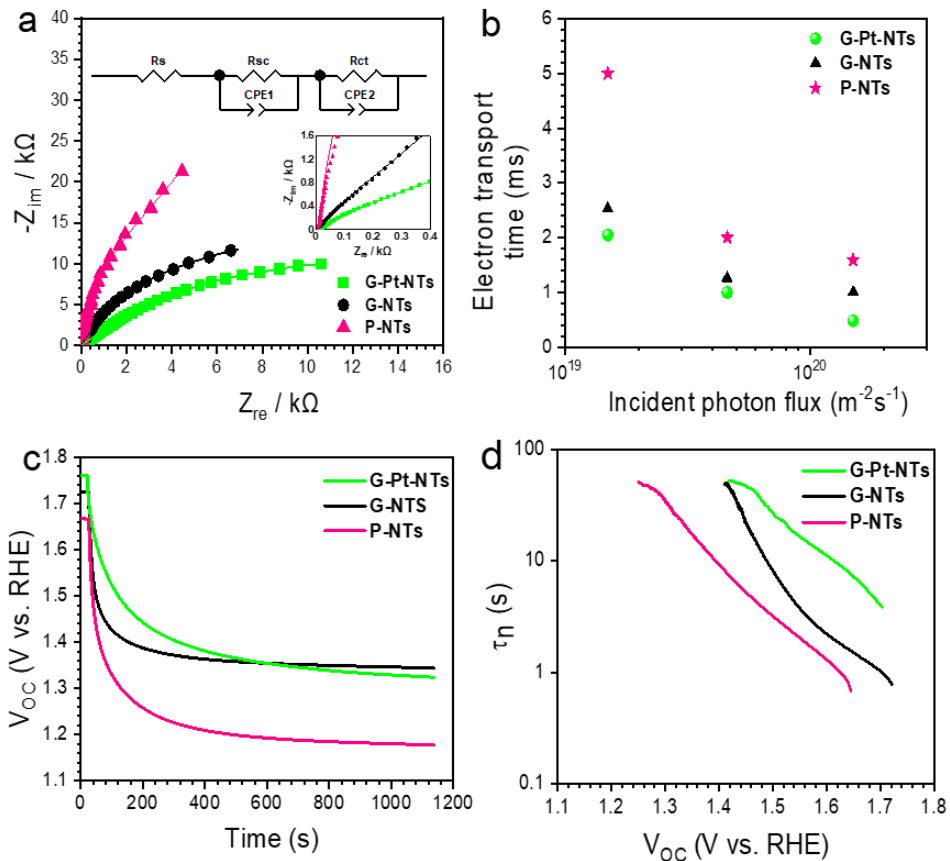


Figure 8 a) Nyquist plots of as prepared P-NTs, G-NTs, and G-Pt-NTs samples obtained in 1 M NaOH solution at 1.5 V vs. RHE (the inset shows EIS at high frequency and the equivalent circuits used to fit the impedance spectra), b) comparison of transport time constant for the P-NTs, G-NTs, and G-Pt-NTs samples as a function of incident photon flux for monochromatic light at 369 nm, c)  $V_{\text{OC}}$  decay measurement of P-NTs, G-NTs, and G-Pt-NTs under one sun (100 W/m<sup>2</sup> –AM 1.5 G) illumination, and d) corresponding electron life-time.

## 2.2 Pt-SA decoration

Decreasing the catalyst size results in not only an increase in the catalyst's active surface area but also an improvement in the photocatalytic activity. Recently, single-atom catalysts (SACs) have attracted special attention as a new class of heterogeneous catalysts due to higher selectivity and superior catalytic activity in a variety of chemical reactions compared to nanoparticle catalysts (NPCs) [34]. Homogeneous loading of SA noble metal such as Pt as one of the most attractive metal (*i.e.*; for photocatalytic reactions) onto suitable support materials play an important role to tune the interaction between atoms and thereby providing highly active SA catalysts. Pt surface decoration of TiO<sub>2</sub> is one of the most adopted strategies to improve its H<sub>2</sub> production photocatalytic activity. Thus, the highly ordered TiO<sub>2</sub> nanotube arrays (TNTs) were synthesized on Ti foil via the electrochemical anodization method. We modified their surface by reducing treatment using ultrasounds. The impregnation method was used as a straightforward route for anchoring Pt SAs on the sonicated TNTs films. The density of the Pt catalyst on the sonicated TNTs was controlled by varying their soaking time in a dilute aqueous Pt solution. As shown in Figure 6, to prepare the Pt-SA catalyst, reduced TNTs were fabricated through sonicating of bare TNTs for various times of sonication ranging from 30 to 80 min. Before soaking the sonicated TNTs samples in the deposition bath containing 100  $\mu$ M of chloroplatinic acid, the acid solution was purged for a duration of 30 min in the Ar atmosphere to extract the dissolved oxygen (O<sub>2</sub>). Then, without any further purification, the sonicated samples were soaked in a very dilute chloroplatinic acid solution for different times (1, 10, 15, 30, and 60 min). For the sake of simplicity, pristine TNTs arrays, sonicated TNTs, and Pt-decorated TNTs are hereafter referred to as P-NT, Rx-NT (x=30, 40, 50, 60, 70, and 80 min), and R50/Pt-NTy (y=1, 10, 15, 30 and 60 min), respectively.

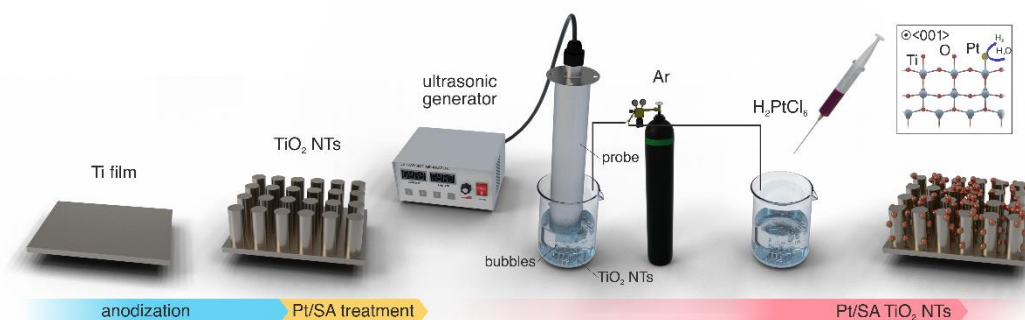


Figure 9 Schematic illustration of preparation Pt-SA TNTs.

Firstly, the TNTs were fabricated by electrochemical anodization method at room temperature for 30 min by using a constant voltage of 70 V in an electrolyte solution containing 94.65 wt% of ethylene glycol, HF, and deionized (DI) water. Then, as prepared TNTs were annealed for 2 h at 450°C in air with a heating and cooling rate of 2°C/min. The XRD pattern of the calcined sample demonstrated the anatase phase. The ultrasound post-treatment (140 W with a frequency of 18.1 KHz) has been applied for various sonication time to introduce the defect site on the TNTs surface. Figure 7 a,b shows the SEM images of the TNTs (P-NT) sample featuring a morphology with the open top that the length and mean diameter of the P-NT sample were 6.1  $\mu\text{m}$  and 100 nm, respectively. As an exemplary morphology of sonicated TNTs, The SEM image of the sonicated sample for 50 min (R50-NT) shows analogous morphology to the P-NT sample (Figure 7c).

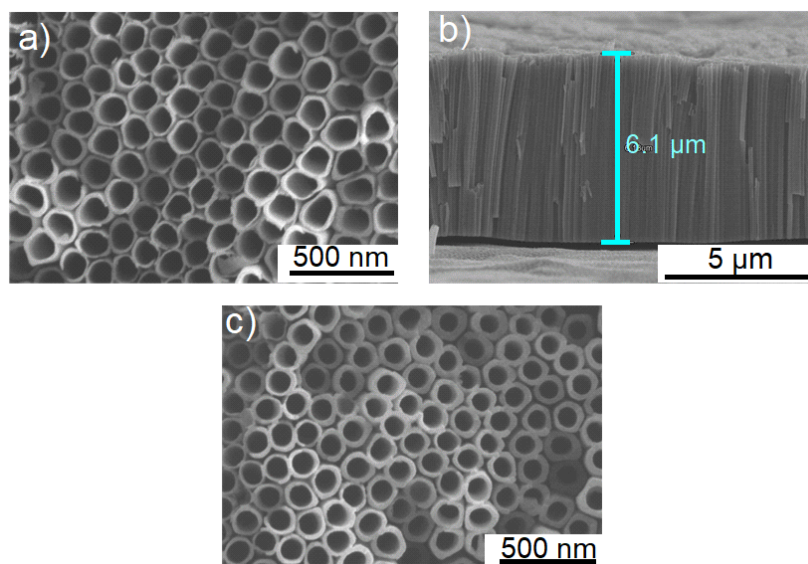


Figure 10 SEM image of samples: a) P-NT, b) showing cross section of P-NT and c) R50-NT.

The occupied density of state (DOS) through the UV-DRS reflectance results and valence band (VB) XPS spectra (Figure 8a-d) is calculated for further the investigation of the band gap narrowing phenomenon and improvement of photophysical properties of the sonicated sample (R50-NT). The P-NT sample showed the maximum energy of VB in DOS at +2.8 eV by linear extrapolation of the peaks to the baseline, while, the maximum level of VB energy and band tail for the R50-NT sample was determined at +2.9 eV and +1.5 eV, respectively (Figure 8d). The band gap energy of P-NTs and R50-NT samples based on UV-Vis DRS measurements are obtained at 3.2 eV and 3.1 eV, respectively. Therefore, the observed narrowing of the band gap in the sonicated sample (R50-NT) can be explained as a small band tail detected within the valence band. However, the conduction band minimum of P-NT and R50-NT samples is located at -0.4 and -0.2 eV, respectively. We measure the HRXPS analysis of the sonicated sample for 50 min (R50-NT), to gain insight into the effect of sonication on its surface and chemical composition (Figure 8e). The two broad peaks centered at 458.6 eV and 464.4 eV are assigned to the  $Ti2p_{3/2}$  and  $Ti2p_{1/2}$  orbitals of  $Ti^{4+}$  in the TNTs lattice, respectively [35,36]. The presence of two small peaks at lower binding energies for the R50-NT sample is

related to the  $\text{Ti}^{3+}$  species [37,38]. Consequently, these results demonstrated that using the sonication to reduce TNTs could be effective to form not only defects and structural disorder but also localized states above the valence band, as shown in Figure 8c.

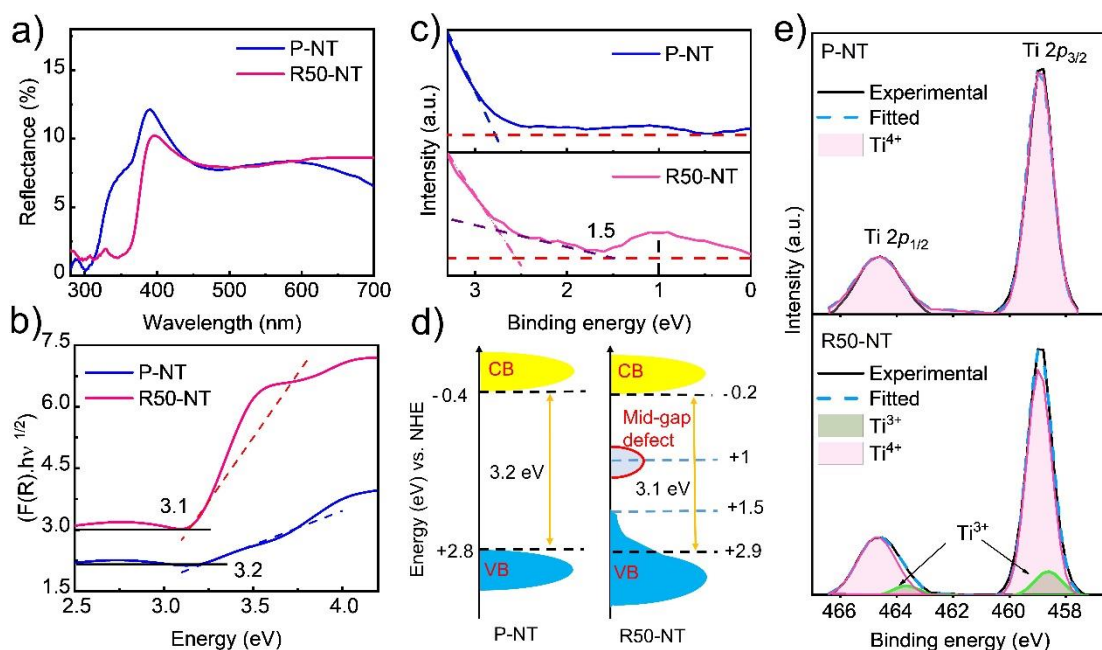


Figure 11 a) UV-Vis DRS of P-NT, R50-NT sample, b) calculated bandgap energies of P-NT and R50-NT, XPS VB spectra of c) P-NT and R50-NT, d) schematic diagram of the DOS of P-NT and R50-NT and e) high-resolution XPS spectra in the Ti2p region for P-NT and R50-NT.

The photoelectrochemical (PEC) water splitting performance of sonicated samples with different time of sonication was measured, owing to selecting the most efficient substrate for Pt-SA decoration. Figure 9a demonstrates the response of photocurrent density versus voltage (J-V) obtained for the sonicated samples with on/off cycles using AM 1.5 G illumination ( $100 \text{ mW cm}^{-2}$ ). The R50-NT sample showed the highest photocurrent density ( $\sim 100 \mu\text{A cm}^{-2}$  at 0.123 V vs. RHE) under solar irradiation which is about 2 times higher activity than that of pristine TNTs (P-NT). Based on these results, the sample sonicated for 50 min (R50-NT) has been selected as the main sample for Pt-SA decoration. Figure 9c shows the results of Mott-Schottky measurements performed on pristine TNTs and R50-NT electrodes. Both electrodes showed a positive slope, corresponding to the finding that they act as an n-type semiconductor [39]. Furthermore,

Mott-Schottky analysis, which correlated capacitance (C) versus applied voltage (V), was carried out to determine carrier concentration ( $N_D$ ) with the following equation;

$$N_D = - \left( \frac{2}{e\epsilon\epsilon_0} \right) \left( \frac{d \left( \frac{1}{C^2} \right)}{d(E_s)} \right)^{-1}$$

Where the  $e$  is the electrical charge,  $N_D$  is the carrier density of electrons,  $C$  is the space charge capacitance for the semiconductor,  $K_B$  is the Boltzmann constant,  $E_s$  is the applied potential,  $\epsilon_0$  is the permittivity of the vacuum,  $\epsilon$  is the relative permittivity of semiconductor (TNTs),  $E_{FB}$  is flat potential and  $T$  is the absolute temperature. Here,  $e = -1.6 \times 10^{-19}$ ,  $\epsilon_0 = 8.86 \times 10^{-12} \text{ Fm}^{-1}$ , and  $\epsilon = 48$  for TNTs in anatase phase [40]. The R50-NT sample indicated higher carrier density ( $1.43 \times 10^{16} \text{ cm}^{-3}$ ) compare to the P-NT ( $0.92 \times 10^{16} \text{ cm}^{-3}$ ). The increase in carrier density of the R50-NT sample shows using the sonication process for the reduction of the sample could enhance the electron density of R50-NT. This can be a result of defect formation including  $\text{Ti}^{3+}$  states and oxygen vacancy [45]. Electrochemical impedance spectroscopy (EIS) was carried out for the investigation of the charge transfer capability of photoanodes, under 1 sun illumination at the bias voltage +1.5 vs. RHE in the range of 0.1 Hz to 100 KHz ( $100 \text{ mW cm}^{-2}$ ). The semicircle radius for the P-NT sample is larger than that of R50-NT, indicating higher resistance to charge transfer at the electrode/electrolyte interface [3]. Therefore, the increase in carrier density of the sonicated TNTs (R50-NT) as well as lower resistivity (faster charge transfer) result in higher PEC performance. The Incident photon to current efficiency (IPCE) spectra was measured for P-NTs and R50-NT samples at +1.5 V vs. RHE in a 1 M NaOH solution to study the contribution of each wavelength photoelectrodes to convert the incident light into photocurrent. The IPCE values were calculated using the following formula [4]:

$$IPCE (\%) = \frac{I_{sc}(A)}{P(W)} \times \frac{1240}{\lambda(\text{nm})} \times 100$$

Where  $P$  is the light power at the specific wavelengths,  $\lambda$  is the wavelength of incident light (nm) and  $I$  is the obtained photocurrent density ( $\mu\text{A m}^{-2}$ ). As shown in Figure 9d, the measured IPCE for the R50-NT sample in the UV region is 70% at 380 nm, which shows greatly enhanced IPCE values. The IPCE of pristine TNTs (P-NT) is 50% at the same wavelength.

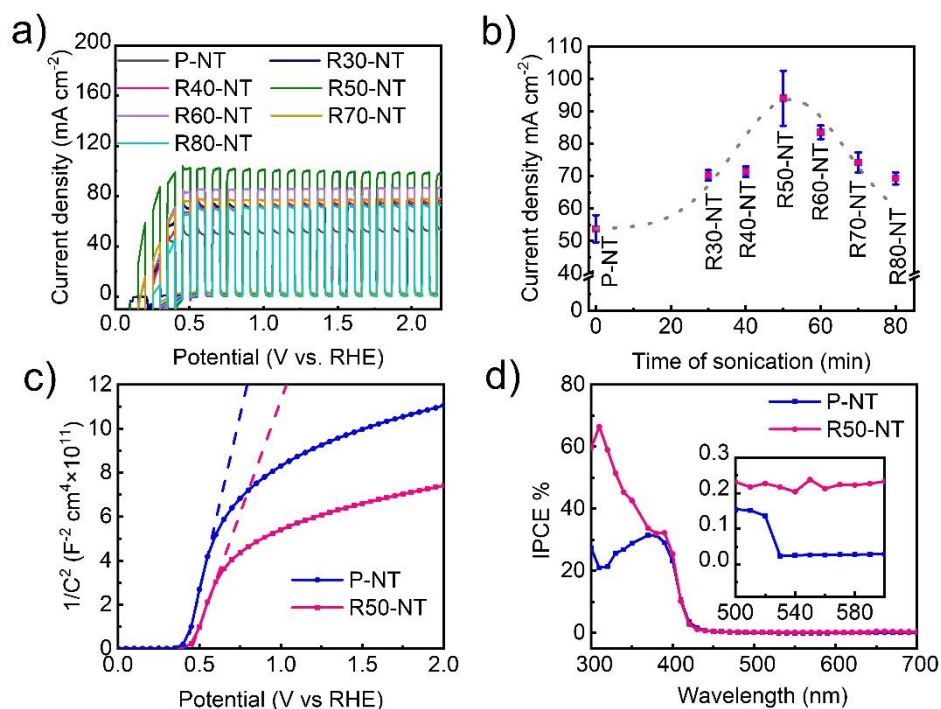


Figure 12 a) Photoelectrochemical response of TNTs samples sonicated for different time measured under 1 sun illumination ( $100 \text{ mW cm}^{-2}$  - AM1.5 G) in 1 M NaOH solution; b) comparison of current density at 1.23 V for the investigated samples, c) Mott–Schottky plots P-NT and R50-NT obtained at a frequency of 5KHz in the dark and d) corresponding IPCE spectra.

Immediately after reduction using the tip sonication, to obtain Pt SA-trapping, fabricated substrate (sonicated TNTs) was immersed in very dilute Pt containing solution for different times (1, 10, 15, 30, and 60 min). Figure 10a shows TEM images of samples sonicated for 50 min and decorated with different loading of Pt. The Pt in the form of nanoparticles was observed for the R50/Pt-NT30 and R50/Pt-NT60 samples (for the 30 and 60 min impregnation time, respectively).

Similarly, the results of energy dispersive spectrometry (EDS) analysis show that Pt can be detected on the substrate in the solution only after 30 min soaking time and for the R50/Pt-NT30 and R50/Pt-NT60 samples. To corroborate the presence of Pt-SA on the surface of TNTs, the HAADF-STEM (High-Angle-Annular-Dark-Field scanning transmission electron microscopy) was performed (Figure 10b). The large number of highly distributed Pt-SA (marked bright dots) in the form of the isolated single atom is shown on the surface of the R50/Pt-NT10 sample. EDS mapping for the R50/Pt-NT10 was carried out to assess the distribution of Ti, O, and Pt of the catalyst (Figure 10c). The result further confirms an almost uniform distribution of elements, including Pt single atoms; no contamination was detected.

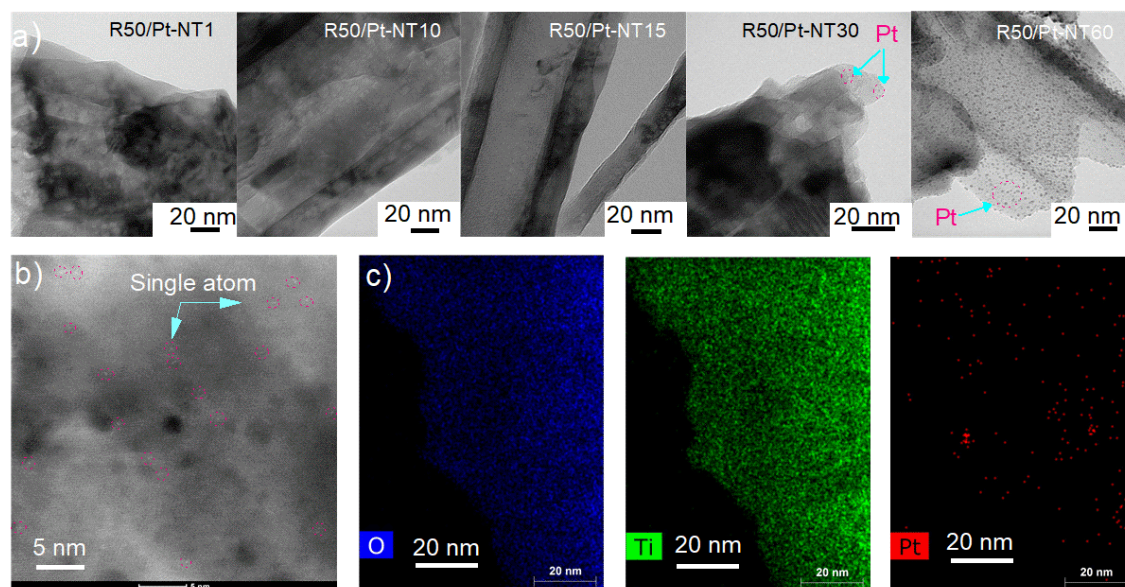


Figure 13 a) TEM images of treated samples at different impregnation time (ranging from 1 to 60 min) in hexachloroplatinic acid solution, b) HAADF-STEM image and c) EDS elemental mapping of R50/Pt-NT10 sample.

As shown in Figure 11a, from the whole XPS survey spectrum, the elements of Ti, O, Pt, and adventitious C can be observed, and based on atomic composition of  $\text{TiO}_2$ , the atomic ratio of Ti:O is about 1:2. Deconvoluted HRXPS spectra of the Pt4f region for the R50/Pt-NT10 and R50/Pt-NT30 (Pt-SA and Pt-NP decorated samples, respectively) are shown in Figure 11b,c, respectively. Figure 11b demonstrates that the XPS spectrum of

Pt4f for the R50/Pt-NT10 sample can be fitted into four peaks. The peaks at 72.3 eV and 75.7 eV can be attributed to  $\text{Pt}^{2+}4f_{7/2}$  and  $\text{Pt}^{2+}4f_{5/2}$ , respectively, whereas the peaks at 73.2 eV and 76.5 eV assigned to  $\text{Pt}^{4+}4f_{7/2}$  and  $\text{Pt}^{4+}4f_{5/2}$  signals, correspondingly. Contrary, for the sample R50/Pt-NT30 (emerging threshold of nanoparticles based on TEM image in Figure 10a) the region corresponding to the Pt4f peak may be deconvoluted into three components (*i.e.*,  $\text{Pt}^{2+}$ ,  $\text{Pt}^{4+}$ , and  $\text{Pt}^0$ ). However, two peaks in metallic state centered at 71.1 eV and 74.5 eV are related to  $\text{Pt}^0 4f_{7/2}$  and  $\text{Pt}^0 4f_{5/2}$ , respectively [41–43]. These results are in line with TEM results (Figure 10a), where the nanoparticles can be observed after 30 min soaking time in dilute Pt solution. Moreover, the HRXPS analysis of the R50/Pt-NT and R50/Pt-NT15 are observed to be quite similar to that of the Pt4f peaks of the R50/Pt-NT10 sample and showed the presence of Pt in the oxidized state ( $\text{Pt}^{2+}$  and  $\text{Pt}^{4+}$ ). In contrast, for the samples, R50/Pt-NT60, the Pt in the metallic state ( $\text{Pt}^0$ ) with peaks located at 70.2 eV and 73.5 eV are observed and can be assigned to  $\text{Pt}^0 4f_{7/2}$  and  $\text{Pt}^0 4f_{5/2}$ , respectively [44,45]. These results show that increasing the impregnation time leads to an increase in the number of Pt deposited on the TNTs surface. As a result, the concentration of Pt in atomic-scale decoration for the R50/Pt-NT1, R50/Pt-NT10, and R50/Pt-NT15 samples is approximately 0.1, 0.2, and 0.4 at%, respectively. Whereas, in the form of nanoparticles for the R50/Pt-NT30, R50/Pt-NT60 samples are about 2.2 and 4.2 at%, respectively (Figure 11d).

To assess the photocatalytic activity of fabricated samples, the open circuit  $\text{H}_2$  evolution was measured in methanol-water solution using a 1 sun solar simulator (AM 1.5 G-100  $\text{mW cm}^{-2}$ ). Figure 12a demonstrate that all the Pt-decorated TNTs exhibit a significantly higher amount of photocatalytic  $\text{H}_2$  evolution, which is at least 10 times higher than that the value obtained for pristine and sonicated TNTs ( $\sim 0.4 \mu\text{l h}^{-1} \text{cm}^{-2}$  for both P-NT and R50-NT).

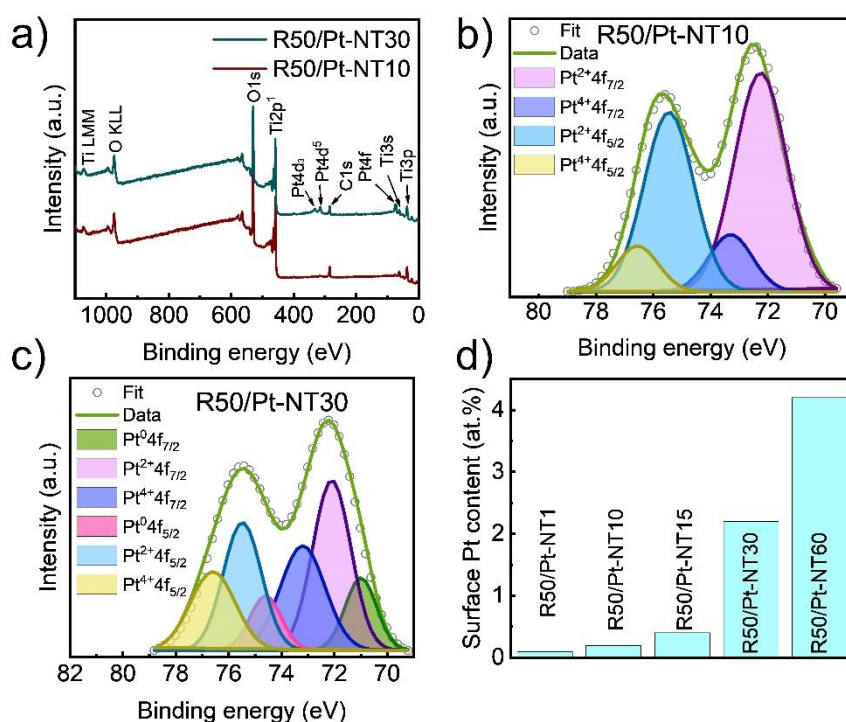


Figure 14 a) Overall XPS survey spectra of sonicated TNTs at different soaking time in Pt solution, b,c) HRXPS spectra of Pt4f for: b) sonicated TNTs for 50 min, followed by immersion in the hexachloroplatinic acid solution for 10 min, c) for 30 min and d) quantitative comparison of surface Pt on Pt-decorated TNTs.

Comparing the results of samples contain Pt-SA (*i.e.*; R50/Pt-NT1, R50/Pt-NT10 and R50/Pt-NT15) with Pt-NP catalysts (R50/Pt-NT30 and R50/Pt-NT60) revealed lower H<sub>2</sub> evolution rate. However, as depicted in Figure 12b, we normalized the data to the surface amount of Pt, to demonstrate the efficacy of the atomic scale Pt decoration on the H<sub>2</sub> evolution rate. The new method achieves almost 50 fold higher hydrogen evolution than pristine TiO<sub>2</sub> nanotubes. It also enables TiO<sub>2</sub> nanotubes decoration with ultrasmall nanoparticles through the impregnation, leading to 10 fold higher hydrogen production using platinum single atoms compared to nanoparticles. The reusability test of the Pt-SA site on the sonicated TNTs surface demonstrated no obvious decrease in efficiency for H<sub>2</sub> production after five successive cycles of reuse, which indicated the impressive stability of the synthesized catalyst (Figure 12c).

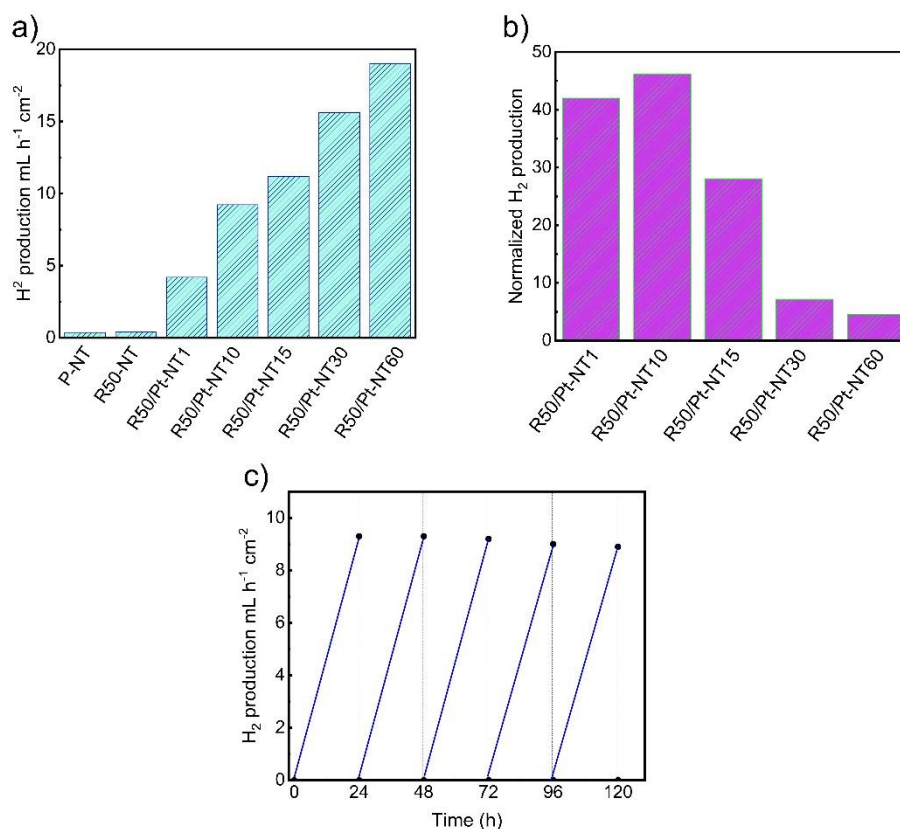


Figure 15 a) H<sub>2</sub> evolution of pristine, sonicated and Pt-decorated TNTs, b) Normalized H<sub>2</sub> evolution of Pt-SA catalysts and c) reusability test of H<sub>2</sub> evolution of R50/Pt-NT10, sonicated for 50 min, followed by immersion in the hexachloroplatinic acid solution for 10 min.

## Conclusion

This doctoral dissertation focused on optimizing the decoration of TiO<sub>2</sub> nanotubes with both metal and non-metal materials to enhance their photocatalytic activity. Given global environmental concerns and energy shortages, TiO<sub>2</sub> has gained significant attention for its energy-related applications. As a result, TiO<sub>2</sub> nanotubes were synthesized through anodization on Ti foil. Surface modifications using platinized cyanographene and Pt single-atom decoration techniques were investigated to improve the photocatalytic performance of the TiO<sub>2</sub> nanostructures. The synthesized samples were characterized by various methods including SEM, HRTEM, XRD, XPS, and UV-vis DRS techniques. The outcomes showed that surface modifications with metal and non-metal materials indeed enhanced the photocatalytic and photoelectrocatalytic performance of the TNTs. This

breakthrough, particularly in the noble metal usage with exceptional stability, marks a significant step towards future energy applications.

## References

- [1] N. Armaroli, V. Balzani, The future of energy supply: Challenges and opportunities, *Angew. Chemie - Int. Ed.* 46 (2007) 52–66. doi:10.1002/anie.200602373.
- [2] H. Du, Y.N. Liu, C.C. Shen, A.W. Xu, Nanoheterostructured photocatalysts for improving photocatalytic hydrogen production, *Chinese J. Catal.* 38 (2017) 1295–1306. doi:10.1016/S1872-2067(17)62866-3.
- [3] S. Kment, F. Riboni, S. Pausova, L. Wang, L. Wang, H. Han, Z. Hubicka, J. Krysa, P. Schmuki, R. Zboril, Photoanodes based on TiO<sub>2</sub> and  $\alpha$ -Fe<sub>2</sub>O<sub>3</sub> for solar water splitting-superior role of 1D nanoarchitectures and of combined heterostructures, *Chem. Soc. Rev.* 46 (2017) 3716–3769. doi:10.1039/c6cs00015k.
- [4] I. Dincer, C. Acar, Review and evaluation of hydrogen production methods for better sustainability, *Int. J. Hydrogen Energy.* 40 (2015) 11094–11111. doi:10.1016/j.ijhydene.2014.12.035.
- [5] M. Ji, J. Wang, Review and comparison of various hydrogen production methods based on costs and life cycle impact assessment indicators, *Int. J. Hydrogen Energy.* 46 (2021) 38612–38635. doi:10.1016/j.ijhydene.2021.09.142.
- [6] L. Finegold, J.L. Cude, Electrochemical Photolysis of Water at a Semiconductor Electrode, *Nature.* 238 (1972) 38–40. doi:10.1038/238038a0.
- [7] R.M. Navarro Yerga, M. Consuelo Álvarez Galván, F. del Valle, J.A. Villoria de la Mano, J.L.G. Fierro, Water splitting on semiconductor catalysts under visiblelight irradiation, *ChemSusChem.* 2 (2009) 471–485. doi:10.1002/cssc.200900018.
- [8] M. Shahrezaei, A.A. Babaluo, S. Habibzadeh, M. Haghghi, Photocatalytic Properties of 1D TiO<sub>2</sub> Nanostructures Prepared from Polyacrylamide Gel–TiO<sub>2</sub> Nanopowders by Hydrothermal Synthesis, *Eur. J. Inorg. Chem.* 2017 (2017) 694–703. doi:10.1002/ejic.201600820.
- [9] S. Kment, H. Kmentova, P. Kluson, J. Krysa, Z. Hubicka, V. Cirkva, I. Gregora, O. Solcova, L. Jastrabik, Notes on the photo-induced characteristics of transition metal-doped and undoped titanium dioxide thin films, *J. Colloid Interface Sci.* 348 (2010) 198–205. doi:10.1016/j.jcis.2010.04.002.
- [10] M. Shahrezaei, S. Habibzadeh, A.A. Babaluo, H. Hosseinkhani, M. Haghghi, A. Hasanzadeh, R. Tahmasebpour, Study of synthesis parameters and photocatalytic activity of TiO<sub>2</sub> nanostructures, *J. Exp. Nanosci.* 12 (2017) 45–61. doi:10.1080/17458080.2016.1258495.
- [11] A. Naldoni, M. Altomare, G. Zoppellaro, N. Liu, S. Kment, R. Zbořil, P. Schmuki, Photocatalysis with Reduced TiO<sub>2</sub>: From Black TiO<sub>2</sub> to Cocatalyst-Free Hydrogen Production, *ACS Catal.* 9 (2019) 345–364. doi:10.1021/acscatal.8b04068.
- [12] Z. Wu, I. Hwang, G. Cha, S. Qin, O. Tomanec, Z. Badura, S. Kment, R. Zboril, P. Schmuki, Optimized Pt Single Atom Harvesting on TiO<sub>2</sub> Nanotubes Towards a Most Efficient Photocatalyst, *Small.* 18 (2022) 2104892. doi:10.1002/smll.202104892.
- [13] F. Shahvaranfard, P. Ghigna, A. Minguzzi, E. Wierzbicka, P. Schmuki, M. Altomare, Dewetting of PtCu Nanoalloys on TiO<sub>2</sub> Nanocavities Provides a Synergistic Photocatalytic Enhancement for Efficient H<sub>2</sub> Evolution, *ACS Appl. Mater. Interfaces.* 12 (2020) 38211–38221. doi:10.1021/acsami.0c10968.
- [14] C. Xia, T. Hong Chuong Nguyen, X. Cuong Nguyen, S. Young Kim, D.L.T. Nguyen, P. Raizada, P. Singh, V.H. Nguyen, C. Chien Nguyen, V. Chinh Hoang,

- Q. Van Le, Emerging cocatalysts in TiO<sub>2</sub>-based photocatalysts for light-driven catalytic hydrogen evolution: Progress and perspectives, *Fuel*. 307 (2022) 121745. doi:10.1016/j.fuel.2021.121745.
- [15] A. Mittal, B. Mari, S. Sharma, V. Kumari, S. Maken, K. Kumari, N. Kumar, Non-metal modified TiO<sub>2</sub>: a step towards visible light photocatalysis, *J. Mater. Sci. Mater. Electron.* 30 (2019) 3186–3207. doi:10.1007/s10854-018-00651-9.
- [16] R. Daghrir, P. Drogui, D. Robert, Modified TiO<sub>2</sub> for environmental photocatalytic applications: A review, *Ind. Eng. Chem. Res.* 52 (2013) 3581–3599. doi:10.1021/ie303468t.
- [17] Y. Fu, A. Mo, A Review on the Electrochemically Self-organized Titania Nanotube Arrays: Synthesis, Modifications, and Biomedical Applications, *Nanoscale Res. Lett.* 13 (2018) 187. doi:10.1186/s11671-018-2597-z.
- [18] M. Ge, C. Cao, J. Huang, S. Li, Z. Chen, K. Zhang, S.S. Al-Deyab, Y. Lai, A Review of One-dimensional TiO<sub>2</sub> Nanostructured Materials for Environmental and Energy Applications, *J. Mater. Chem. A.* (2013) 1–26. doi:10.1039/x0xx00000x.
- [19] M. Shahrezaei, S. Habibzadeh, A.A. Babaluo, M. Haghghi, A. Hasanzadeh, R. Tahmasebpour, Study of synthesis parameters and photocatalytic activity of TiO<sub>2</sub> nanostructures, *J. Exp. Nanosci.* 12 (2017) 45–61. doi:10.1080/17458080.2016.1258495.
- [20] J. Tian, Z. Zhao, A. Kumar, R.I. Boughton, H. Liu, Recent progress in design, synthesis, and applications of one-dimensional TiO<sub>2</sub> nanostructured surface heterostructures: A review, *Chem. Soc. Rev.* 43 (2014) 6920–6937. doi:10.1039/c4cs00180j.
- [21] B.M. Rao, A. Torabi, O.K. Varghese, Anodically grown functional oxide nanotubes and applications, *MRS Commun.* 6 (2016) 375–396. doi:10.1557/mrc.2016.46.
- [22] T.M. David, P.R. Dev, P. Wilson, P. Sagayaraj, T. Mathews, A critical review on the variations in anodization parameters toward microstructural formation of TiO<sub>2</sub> nanotubes, *Electrochem. Sci. Adv.* (2021) e202100083. doi:10.1002/elsa.202100083.
- [23] L. Wei, C. Yu, Q. Zhang, H. Liu, Y. Wang, TiO<sub>2</sub>-based heterojunction photocatalysts for photocatalytic reduction of CO<sub>2</sub> into solar fuels, *J. Mater. Chem. A.* 6 (2018) 22411–22436. doi:10.1039/c8ta08879a.
- [24] G. Tian, H. Fu, L. Jing, B. Xin, K. Pan, Preparation and Characterization of Stable Biphasic TiO<sub>2</sub> Photocatalyst with High Crystallinity, Large Surface Area, and Enhanced Photoactivity, *J. Phys. Chem. C.* 112 (2008) 3083–3089. doi:10.1021/jp710283p.
- [25] A. Bakandritsos, M. Pykal, P. Blonski, P. Jakubec, D.D. Chronopoulos, K. Poláková, V. Georgakilas, K. Cepe, O. Tomanec, V. Ranc, A.B. Bourlinos, R. Zboril, M. Otyepka, Cyanographene and Graphene Acid: Emerging Derivatives Enabling High-Yield and Selective Functionalization of Graphene, *ACS Nano.* 11 (2017) 2982–2991. doi:10.1021/acsnano.6b08449.
- [26] S.P. Albu, H. Tsuchiya, S. Fujimoto, P. Schmuki, TiO<sub>2</sub> nanotubes - Annealing effects on detailed morphology and structure, *Eur. J. Inorg. Chem.* 2010 (2010) 4351–4356. doi:10.1002/ejic.201000608.
- [27] C. Zhai, M. Zhu, D. Bin, H. Wang, Y. Du, C. Wang, P. Yang, Visible-light-assisted electrocatalytic oxidation of methanol using reduced graphene oxide modified Pt nanoflowers-TiO<sub>2</sub> nanotube arrays, *ACS Appl. Mater. Interfaces.* 6 (2014) 17753–17761. doi:10.1021/am504263e.
- [28] M.-Q. Yang, N. Zhang, Y.-J. Xu, Synthesis of Fullerene-, Carbon Nanotube-, and Graphene-TiO<sub>2</sub> Nanocomposite Photocatalysts for Selective Oxidation: A Comparative Study, *ACS Appl. Mater. Interfaces.* 5 (2013) 1156–1164.

- doi:10.1021/am3029798.
- [29] X. Chen, L. Liu, P.Y. Yu, S.S. Mao, Increasing solar absorption for photocatalysis with black hydrogenated titanium dioxide nanocrystals, *Science* 331 (2011) 746–750. doi:10.1126/science.1200448.
- [30] A. Chen, S. Nigro, Influence of a Nanoscale Gold Thin Layer on Ti/SnO<sub>2</sub>-Sb<sub>2</sub>O<sub>5</sub> Electrodes, *J. Phys. Chem B.* 107 (2003) 13341–13348. doi:10.1021/jp036138w.
- [31] Y. Rambabu, M. Jaiswal, S.C. Roy, Enhanced Photo-Electrochemical Performance of Reduced Graphene- Oxide Wrapped TiO<sub>2</sub> Multi-Leg Nanotubes, *J. Electrochem. Soc.* 8 (2016) H652–H656. doi:10.1149/2.0351608jes.
- [32] X.Y. Yu, J.Y. Liao, K.Q. Qiu, D. Bin Kuang, C.Y. Su, Dynamic study of highly efficient CdS/CdSe quantum dot-sensitized solar cells fabricated by electrodeposition, *ACS Nano.* 5 (2011) 9494–9500. doi:10.1021/nn203375g.
- [33] A. Zaban, M. Greenshtein, J. Bisquert, Determination of the electron lifetime in nanocrystalline dye solar cells by open-circuit voltage decay measurements, *ChemPhysChem.* 4 (2003) 859–864. doi:10.1002/cphc.200200615.
- [34] S. Hejazi, S. Mohajernia, B. Osuagwu, G. Zoppellaro, P. Andryskova, O. Tomanec, S. Kment, R. Zboril, P. Schmuki, On the Controlled Loading of Single Platinum Atoms as a Co-Catalyst on TiO<sub>2</sub> Anatase for Optimized Photocatalytic H<sub>2</sub> Generation, *Adv. Mater.* 32 (2020) 1908505. doi:10.1002/adma.201908505.
- [35] J. Eom, S. Lim, S. Lee, W. Ryu, H. Kwon, Black titanium oxide nanoarray electrodes for high rate Li-ion microbatteries, *J. Mater. Chem. A.* 3 (2015) 11183–11188. doi:10.1039/c5ta01718a.
- [36] H. Cui, W. Zhao, C. Yang, H. Yin, T. Lin, Y. Shan, Y. Xie, H. Gu, F. Huang, Black TiO<sub>2</sub> nanotube arrays for high-efficiency photoelectrochemical water-splitting, *J. Mater. Chem. A.* 2 (2014) 8612–8616. doi:10.1039/c4ta00176a.
- [37] L. Xiong, J. Li, B. Yang, Y. Yu, Ti<sup>3+</sup> in the Surface of Titanium Dioxide: Generation, Properties and Photocatalytic Application, *J. Nanomater.* 2012 (2012) 831524. doi:10.1155/2012/831524.
- [38] X. Jiang, Y. Zhang, J. Jiang, Y. Rong, Y. Wang, Y. Wu, C. Pan, Characterization of Oxygen Vacancy Associates within Hydrogenated TiO<sub>2</sub>: A Positron Annihilation Study, *J. Phys. Chem. C.* 116 (2012) 22619–22624.
- [39] L. Li, J. Yan, T. Wang, Z. Zhao, J. Zhang, J. Gong, N. Guan, Sub-10 nm rutile titanium dioxide nanoparticles for efficient visible-light-driven photocatalytic hydrogen production, *Nat. Commun.* 6 (2015) 5881. doi:10.1038/ncomms6881.
- [40] P.. Ghosh, M.. Azimi, Numerical Calculation of Effective Permittivity of Lossless Dielectric Mixtures using Boundary Integral Method, *IEEE Trans. Dielectr. Electr. Insul.* 1 (1994) 975–981.
- [41] S. Hejazi, S. Mohajernia, B. Osuagwu, G. Zoppellaro, P. Andryskova, O. Tomanec, S. Kment, R. Zboril, P. Schmuki, On the Controlled Loading of Single Platinum Atoms as a Co-Catalyst on TiO<sub>2</sub> Anatase for Optimized Photocatalytic H<sub>2</sub> Generation, *Adv. Mater.* 32 (2020) 1908505. doi:10.1002/adma.201908505.
- [42] T. Xu, H. Zheng, P. Zhang, Isolated Pt single atomic sites anchored on nanoporous TiO<sub>2</sub> film for highly efficient photocatalytic degradation of low concentration toluene, *J. Hazard. Mater.* 388 (2020) 121746. doi:10.1016/j.jhazmat.2019.121746.
- [43] H. Wang, J.X. Liu, L.F. Allard, S. Lee, J. Liu, H. Li, J. Wang, J. Wang, S.H. Oh, W. Li, M. Flytzani-Stephanopoulos, M. Shen, B.R. Goldsmith, M. Yang, Surpassing the single-atom catalytic activity limit through paired Pt-O-Pt ensemble built from isolated Pt1 atoms, *Nat. Commun.* 10 (2019) 3808. doi:10.1038/s41467-019-11856-9.
- [44] Y. Hang Li, J. Xing, Z. Jia Chen, Z. Li, F. Tian, L. Rong Zheng, H. Feng Wang, P. Hu, H. Jun Zhao, H. Gui Yang, Unidirectional suppression of hydrogen

- oxidation on oxidized platinum clusters, *Nat. Commun.* 4 (2013) 2500. doi:10.1038/ncomms3500.
- [45] Z. Lian, W. Wang, G. Li, F. Tian, K.S. Schanze, H. Li, Pt-Enhanced Mesoporous  $\text{Ti}^{3+}/\text{TiO}_2$  with Rapid Bulk to Surface Electron Transfer for Photocatalytic Hydrogen Evolution, *ACS Appl. Mater. Interfaces.* 9 (2017) 16959–16966. doi:10.1021/acsami.6b11494.

## List of Publications

- 1- Mahdi Shahrezaei**, Seyyed Mohammad Hossein Hejazi, Yalavarthi Rambabu, Miroslav Vavrecka, Aristides Bakandritsos, Selda Oezkan, Radek Zboril, Patrik Schmuki, Alberto Naldoni, and Stepan Kment, “Multi-Leg TiO<sub>2</sub> Nanotube Photoelectrodes Modified by Platinized Cyanographene with Enhanced Photoelectrochemical Performance”, *Catalysts* 2020, 10, 717. Doi.org/10.3390/catal10060717.
- 2- S. M. Hossein Hejazi, Mahdi Shahrezaei**, Piotr Błonski, Mattia Allieta, Polina M. Sheverdyeva, Paolo Moras, Zdenek Badura, Sergii Kalytchuk, Elmira Mohammadi, Radek Zboril, Stepan Kment, Michal Otyepka, Alberto Naldoni and Paolo Fornasiero, “Defect engineering over anisotropic brookite toward substrate-specific photo-oxidation of alcohols”, *Chem Catalysis* 2022, 2, 5, 1177-1190. Doi.org/10.1016/j.checat.2022.03.015.
- 3- Mahdi Shahrezaei**, S. M. Hossein Hejazi, Hana Kmentova, Veronika Sedajova, Radek Zboril, Alberto Naldoni, and Stepan Kment “Ultrasound-driven defect engineering in TiO<sub>2-x</sub> nanotubes – towards highly efficient platinum single atom enhanced photocatalytic water splitting” *ACS AMI* 2023. Doi.org/10.1021/acsami.3c04811.